Towards the low cost manufacture of dye-sensitized solar cells using inkjet technology

by

Ruth Cherrington

Thesis

Submitted to the University of Warwick

for the degree of Doctor of Philosophy (PhD)

WMG

August 2016

Table of Contents

Acknowledgements

This research is gratefully undertaken with support from the Engineering and Physical Sciences Research Council (EPSRC). I would like to thank my supervisors Vannessa Goodship and Darren Hughes for all their continual advice and guidance. I am also very grateful to Beth Middleton, Ben Wood and Kylash Makenji for accompanying me on my journey as a researcher. I would also like to thank Ross Jaggers and Robert Bell from the department of Chemistry and Simon Leigh from the department of Engineering for their advice and use of equipment.

I have been lucky to receive a large amount of support from outside the university. This includes Neil Chilton and Leon Gicquel from Printed Electronics Limited who have been extremely generous with their time in helping me to learn more about inkjet printing and all its complexities. I am also very grateful to Senthilarasu Sundaram from the University of Exeter who has helped me to develop my understanding of several new aspects of dye-sensitised solar photovoltaic materials and manufacturing.

Finally I would like to thank Adam Longfield for his constant enthusiasm and interest in solar energy, which has helped motivate me during some of the more tedious parts of the project. Special thanks also go to my parents for their support, encouragement (and free lodging) throughout my PhD. I couldn't have got here without you.

Declarations

This thesis is submitted in partial fulfilment of the requirements for the degree of Doctor of Philosophy and describes work carried out from September 2012 to May 2016. Unless otherwise indicated, the research described is my own and not the product of collaboration. No part of this thesis has been submitted to any other university, or as any part of any other submission to the University of Warwick.

Research outputs

Publications

Parts of this thesis have been published in the following book chapter and peer-reviewed journal papers:

- Cherrington, R., B.M. Wood, I. Salaoru, and V. Goodship, Digital Printing of Titanium Dioxide for Dye Sensitized Solar Cells. 2016(111): p. e53963.
- Goodship, V., B. Middleton, and R. Cherrington, Design and Manufacture of Plastic Components for Multifunctionality: Structural Composites, Injection Molding, and 3D Printing 2015: Elsevier Science. ISBN 9780323353847
- Cherrington, R., D.J. Hughes, S. Senthilarasu, V. Goodship , Inkjet printed TiO_2 nanoparticles from aqueous solutions for dye sensitized solar cells (DSSCs), Energy Technology, 3 (2015) 866–870.

Patent application

- Goodship, V., B.J. Middleton, and R. Cherrington, Multilayer manufacturing method utilising mould, 2014: United Kingdom. GB application number WO2014091197

Oral Presentation at Conferences

- Cherrington, R., Manufacturing multilayer thin films for photovoltaics'. Presented at UK Plastic Electronics Research Conference Loughborough, United Kingdom, 10-11 December 2013

Poster Presentation at Conferences

- Cherrington, R., J. Liang, B.T. Thompson, 'Making products, saving the planet'. Presented at WMG Doctoral Research and Innovation Conference. Coventry, United Kingdom, 10-11 July 2014
- Cherrington, R., 'Inkjet printed TiO_2 for application in dye-sensitized solar cells'. Presented at European Materials Research Society Spring Meeting. Lille, France, 11 - 15 May 2015
- Cherrington, R., 'Digitally printed dye sensitized solar cells (DSSCs)'. Presented at University of Warwick Research Poster Competition. Coventry, United Kingdom, 10 June 2015

Abstract

This work presents a novel means of producing dye-sensitized solar cells (DSSCs), using an inkjet printing technique. To manufacture a completely inkjet-printed DSSC, all layers must be considered and a thorough analysis of the suitability of the printing process has previously been unreported.

For DSSCs to become commercially viable they must have long term operational stability, be efficient, have a low environmental impact and low manufacturing cost. Inkjet printing is an additive manufacturing process, meaning that material is only deposited where needed, minimising the material wastage.

Several nanoparticle materials were investigated including titanium dioxide (TiO_2), carbon black as a low cost replacement for platinum and PEDOT:PSS as a low cost replacement to the widely used spiro-MeOTAD 92,2' ,7,7'-tetrkis(N,N-di-p-methoxyphenylamine)-9,9-spirobifluorene) solid-state hole transport material.

A highly porous network of metal-oxide nanocrystals is a fundamental building block to produce DSSCs. The morphology of this layer can greatly influence the efficiency of the cell and therefore a significant amount of this project was spent on developing suitable ink and printing this layer. Titanium dioxide (TiO_2) is widely used within the development of photoanodes due to its low cost, stability and low impact on the environment. However, it can be difficult to create a stable dispersion within water due to the natural tendency for the material to agglomerate.

An aqueous TiO_2 nanoparticle dispersion was developed and several additive materials were explored in an effort to optimize the ink. The initial ink was printed to produce a layer 2.6 μm thick which, once incorporated into a DSSC, resulted in a

promising efficiency of 3.50%. Inkjet printed carbon black counter electrodes with thicknesses of 10.24 µm, lead to efficiencies of 2.59%, whilst inkjet printed PEDOT:PSS solid state hole transport material resulted in a very low efficiency of 0.08%. Whilst the PEDOT:PSS and carbon did not produce suitable results for this application, it is suggested that further materials are still investigated due to the benefits of the manufacturing technique. Therefore, it can be concluded that this work shows the capability of inkjet printing for low-cost solar cells, with exciting potential application to other printed electronic applications.

List of abbreviations

AFM	atomic force microscope
AM	air mass
BHJ	bulk heterojunction
CdTe	cadmium telluride
CIGS	gallium selenide
CIJ	continuous inkjet
CIS	copper indium selenide
DC	direct current
DI	deionised
DLS	dynamic light scattering
DMF	dimethylformamide
DMSO	dimethyl sulfoxide
DOD	drop-on-demand
DSC	differential scanning calorimetry
DSSC	dye sensitized solar cell
DWNTs	double walled carbon nanotubes
EC	ethyl cellulose
EPSRC	Engineering and Physical Sciences Research Council
FF	fill factor
FTO	fluorine doped tin oxide
GaAs	gallium arsenide
HEC	hydroxyethyl cellulose
HTM	hole transport material

IEC	International Electrotechnical Commission
IEP	isoelectric point
IPA	isopropyl alcohol
IR	infrared
IS	ionic strength
ITO	indium tin oxide
IV	current-voltage
JCPDS	Joint Committee on Powder Diffraction Standards
MC	methyl cellulose
MPN	N-methoxypriopionitrile
MWNTs	multiwalled carbon nanotubes
ODC	optimum dispersant concentration
OLED	organic light emitting diode
P3HT	poly(3-hexylthiophene)
PAA	polyacrylic acid
PCE	power conversion efficiency
PEDOT	poly(3,4-ethylenedioxythiophene)
PEDOT:PSS	poly(3,4-ethylenedioxythiophene) polystyrene sulfonate
PEG	polyethylene glycol
PEI	polyethleylenimine
PEN	polyethylene naphthalate
PET	polyethylene terephthalate
PLA	polyacrylic acid
PSS	poly(styrenesulfonate)
PV	photovoltaic

PVA	polyvinyl alcohol
PVDF	polyvinylidene fluoride
PVP	polyvinylpyrrolidone
SEM	scanning electron microscopy
ss-DSSC	Solid state dye sensitized solar cell
STC	standard test conditions
SWNTs	single walled carbon nanotubes
TCO	transparent conducting oxide
TEM	transmission electron microscopy
TGA	thermogravimetric analysis
UV	ultraviolet
XRD	x-ray diffraction

List of Figures

List of Tables

Chapter 1

Introduction

1.1 The research problem

Conventional silicon solar cells are made from high purity materials and require expensive and energy consuming specialist equipment, which incorporate a p-n junction to generate electron-hole pairs. The semiconductor within these devices assumes both the task of light absorption and charge carrier transport. Dye-sensitized solar cells (DSSCs) have a fundamentally different working principle; light is adsorbed by a dye, which is attached to the surface of a nanoparticle semiconductor. Charge generation then takes place at the materials interface between the dye and the semiconductor. These offer the potential of very low materials and fabrication costs compared to traditional silicon devices. However up-scaling from small laboratory test cells into large prototypes for industrial manufacturing involves overcoming several issues including the rapid patterning of the underlying surface or layer [1, 2].

Electronics manufacturing generally requires a degree of patterning, which is either achieved by masking or selective removal of the material after deposition. These steps can be potentially removed through the use of an "additive" patterning process such as inkjet printing or spray coating which deposit material only where required, resulting in little or no wastage. Solid state DSSCs (that utilize a gel or solid in-place of a liquid electrolyte) have a simple multilayer structure which could be processed using these techniques. To become commercially viable, DSSCs must have long-term operational stability, be efficient, with low-cost materials and preparation and minimal impact on the environment. The ideal manufacturing

technique should be able to use flexible substrates with as few processing steps as possible. In consideration of these requirements, an additive manufacturing technique would be ideally suited to the production of solid state DSSCs, however there are very few studies that investigate modifying the materials and structure of devices to utilise additive or digital manufacturing processes [3].

A significant proportion of work in the DSSC research community is focussed on the development of new materials. In particular, focus is on new dyes that can be manufactured faster and cheaper with the potential to capture wide wavelength ranges. Another area of materials research is investigating the modification of the TiO_2 layer through the use of nanotubes, wires, core-shell materials or template-based structures [4-6]. Ongoing work is also concentrated on solvent-free or solid state electrolytes to replace the liquid electrolyte that is currently the standard structure reported [1, 7-16]. Optimization of the device architecture constitutes a smaller research field. Some work has been conducted on alternative substrates to glass including plastic and steel [17-20]. Other work investigates the replacement of fluorine doped tin oxide (FTO) with alternative transparent conductive materials using traditional manufacturing procedures [21, 22].

The nano-structured metal oxide layer within DSSCs plays a critical role in the overall performance of the cell, with material choice, processing methods and nature of the structure all having influencing factors [16, 23-27]. One of the most important requirements for the photoanode is that it needs to exhibit an extremely large surface area, this is achieved through the deposition of nanoparticle materials, commonly TiO_2 [1, 28]. This layer has been fabricated by countless different processes with wet coating techniques still the most popular approach, the most common being screen-

printing and doctor-blading [23, 26, 29]. There are very few published papers that have investigated inkjet printing of TiO_2 as a deposition route for application in DSSCs despite apparent benefits of the processing method [24, 30]. There are also few published papers which consider the issue of adhesion of the printed layer with the substrate [25, 31-34], which is an essential issue that needs to be addressed for larger scale applications and will be discussed in section 4.6. Although single-step deposition is beneficial to maintain high manufacturing speeds, multilayer deposition has already been shown to improve the conversion efficiency of cells [35]. Deposition of a thin, highly dense layer of TiO_2 prior to a thicker and more porous layer can directly enhance DSSC performance [35]. This enhancement is currently achieved through two manufacturing techniques whereas inkjet printing could potentially be used to produce both these layers by modifying the ink composition. Further layers could also be introduced to produce a density profile that progresses from high to low.

In the existing literature, there are no reports of a DSSC device deposited completely by inkjet printing. Having addressed the potential of additive printing, this work aims to move toward a fully inkjet printed, low cost DSSC by filling some of the gaps in the body of knowledge. It was determined that there were neither the inks available nor adequate information on optimising the print parameters to produce a fully inkjet printed, low cost device. Therefore, two main objectives for this work were established which address current research gaps. The first objective was to research the development of nanoparticle inks with the desired degree of stability and rheological behaviour to allow additive layer manufacture. The second objective was to utilize these optimized inks to produce films and test their functionality once they had been deposited by digital printing methods.

1.2 Aims of this work

The main aim of this work was to further develop the science behind functional inks for printing DSSC devices using inkjet techniques, and to examine the potential and performance of such materials in a fully printed DSSC device. In consideration of the knowledge gaps identified in the literature, the following objectives were identified:

- Identify suitable functional materials for the production of DSSCs using inkjet techniques
- Perform fundamental research into the formulation of functional inks by evaluating the suitability of the materials for the printing process
- Analyse the thickness and surface quality of the films once printed
- Characterise (where necessary) the functionality of the printed films
- Examine the potential scalability of the proposed process by determining the optimal structure which can be produced using inkjet printing techniques
- Examine the commercial potential of the proposed process by characterizing the electrical performance of the DSSC

1.3 Thesis structure

This thesis covers several separate disciplines and the structure of the thesis shows the consideration given to each of these and the progression of the project through them. Chapter 2 provides a literature review on photovoltaic technology and the materials used in the manufacture for this project. It continues to introduce the area of printed electronics and the potential role it has in the manufacture of DSSC technology. Chapter 3 then details the materials and methods which were used in the experimental work. Comprehensive results chapters then follow (Chapter 4, Chapter

5 and Chapter 6) highlighting the ink formulation, printing and application to photovoltaic DSSCs. Chapter 7 provides an analysis of the cost and environmental implications of inkjet printed solid state DSSCs. The key findings are then summarised in the conclusions in Chapter 8 along with areas identified for further work.

Chapter 2

Literature review

2.1 Photovoltaic materials

This section provides a review of the materials used within photovoltaic solar cells, which are a technology that convert sunlight into direct current (DC) electricity. Researchers have been developing methods to harness solar energy since it was observed that distinct chemical transformations occur when materials are exposed to sunlight [36]. The types of material that are used within devices designed to capture solar energy has a significant influence on how much energy can be converted into electricity. Although, there are several ways in which to group solar photovoltaic technologies, this section will focus on the materials of manufacture and has therefore been split into inorganic and organic based devices.

2.1.1 Inorganic

The development of photovoltaic cell design and fabrication can be separated into three main categories. First generation, silicon-based devices account for 86 % of the current market [37]. High manufacturing costs are associated with first generation devices; partly due to the highly purified silicon required. This is obtained by firstly reducing silicon dioxide with carbon in a high temperature furnace ($\leq$ 2000 °C). The power conversion efficiency of silicon solar cells is largely dependent on impurity levels in the raw materials; therefore the material is then further purified to reduce impurity levels to less than the parts-per-billion level [38].

Once purified, ingots doped with boron (p-doped) are sliced into wafers. The second side of the photo junction is produced from the same high purity silicon diffused with phosphorous (n-doped). To complete the device (illustrated in Figure 2.1), metal contacts are screen printed onto the surface and it is encapsulated to protect it from damage.

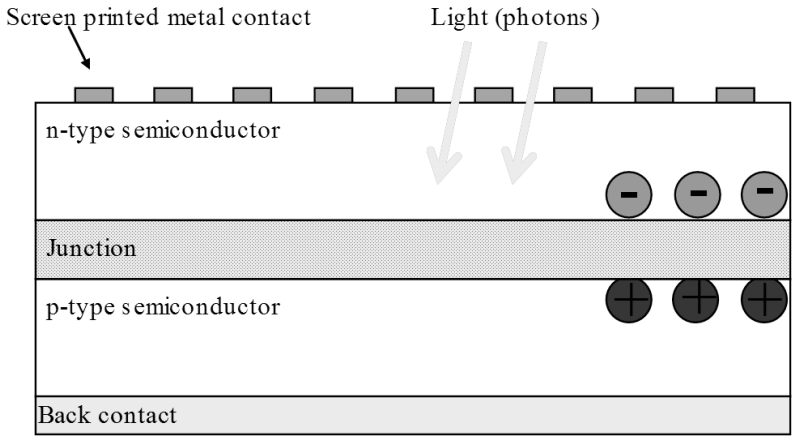

Figure 2.1 - Silicon-based p-n junction

These silicon-based devices are manufactured from either monocrystalline (single-crystal) or polycrystalline (metallurgical grade silicon is melted to 1414 °C and poured into a square mould to produce a block of multi-crystalline silicon) materials. These devices typically have a layer of silicon between 100 and 500 µm, whereas newer thin-film devices have been developed which use a layer thickness of between 1 to 100 µm. However, these thin-film devices are more expensive than that of the bulk-material devices due to the cost associated with processing the materials [39]. Current research is working on the evolution of a new generation of technology to produce high-efficiency thin film technology at low cost [40].

Gallium arsenide (GaAs), cadmium telluride (CdTe), and copper indium gallium selenide (CIGS) are compound semiconductors that have received significant

attention due to the fact they have high absorptivity, present direct band gap energy and can be doped to either p-type or n-type [41, 42].Gallium arsenide (GaAs) is a mixture of gallium and arsenic which has a bandgap of 1.43 eV.

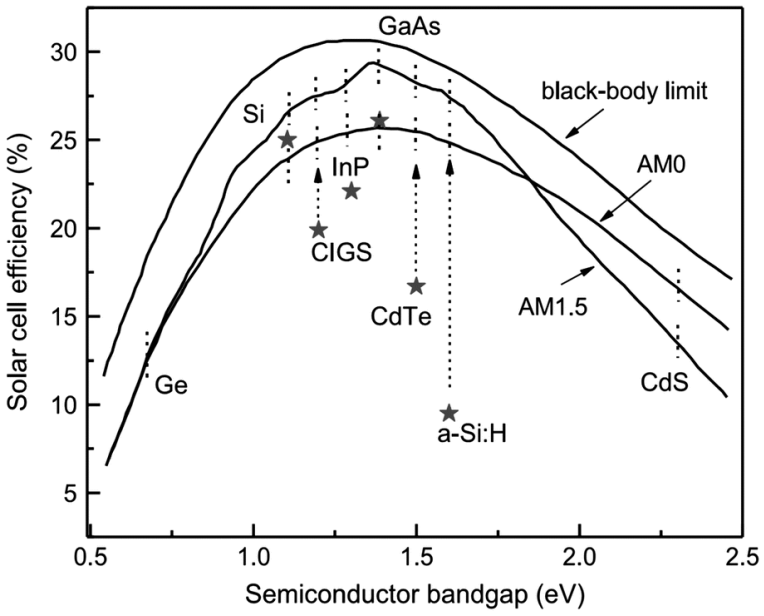

Figure 2.2 - Theoretical efficiency as a function of semiconductor band gap

(From [43])

Figure 2.2 shows how the bandgap of a semiconductor material in a single junction solar cell influences the efficiency. The bandgap of GaAs is almost the same as a black body and should therefore be the ideal material to use to maximise efficiency [43]. The semiconductor compound is able to capture up to 99.5% of solar energy (in the wavelength range from 400–860 nm) and is fairly insensitive to heat [44]. For these reasons GaAs is commonly used in space applications and concentrator systems [45, 46]. GaAs has been combined with other thin-film materials to produce multi-junction cells with laboratory efficiencies of more than 43 % [47]. Gallium is a rare earth metal which may be vulnerable to shortages in the future with global consumptions rising. Arsenic is not rare but is highly toxic, and there are concerns

that arsine or arsenic could be released if cells are not correctly disposed or recycled at end-of-life [48].

Cadmium telluride (CdTe) can be either used alone or easily alloyed with zinc, mercury and others to vary its properties. It is commonly used alongside tin oxide to provide a transparent reflective coating. The more efficient CdTe cells employ a heterojunction interface with cadmium sulphide (CdS). However, CdTe thin film structures can develop high electrical resistances which lead to large internal losses. A method commonly used to overcome this is by allowing the CdTe to be intrinsic (neither p-type nor n-type) and adding a layer of p-type zinc telluride (ZnTe) between the CdTe and the back electrode [49].

Copper indium selenide (CIS) is another promising semiconductor material composed of copper, indium, and selenium. CIS has a very high absorptivity and can capture 99% of the light which shines on the material in the first micrometre. Cadmium sulphide is commonly used as the n-type layer and zinc is sometimes added to improve transparency. Small amounts of gallium can be added to the lower absorbing layer; boosting the band gap which improves the voltage and therefore the efficiency of the device [50].

2.1.2 Organic

Organic solar cells can be separated into three main categories; dye-sensitised solar cells (DSSCs), small molecule cells and polymer cells. Cells which use both organic and inorganic materials within the active layer are called hybrid cells. As DSSCs are the main focus of this work; they will be covered in more detail in section 2.2.

The active material of an organic solar cell can be designed in three ways: single layer, double layer (bilayer heterojunction) or bulk heterojunction (BHJ). Single

layer organic solar cells are made by sandwiching an organic layer between two dissimilar electrodes; one with a low work function and one with a high work function. The work function of an electrode is the minimum energy required to remove an electron from a solid to a point immediately outside the solid surface. When the device is short-circuited, electrons move from the low work function electrode (usually aluminium) to the high work function (usually indium tin oxide, ITO) creating an electric field across the organic layer [51]. These single layer devices had thicknesses between 100 - 500 nm and resulted in power conversion efficiencies between 0.1 - 1.0 % [52].

A double layer structured cell was first introduced in 1986 where p- and n-type organic semiconductor materials were coated one on top of another resulting in a less diffused structure. This bilayer structure has several advantages over the single layer structure for several reasons. The donor acceptor interface is increased resulting in more charge generation and reduced recombination losses due to the fact that electron and hole transport is separated into different materials. The most efficient organic bilayer structure reported has an efficiency of 3.6 % [52]. However, the most successful structure is based on the bulk heterojunction concept [53]. When charges are generated within the active layer, they only have a very short lifetime and therefore can only travel short distances [54]. The bulk heterojunction is designed to capture the charge quickly by reducing the distance that they need to travel before they come into contact with a donor-acceptor interface. A large surface area is achieved by creating a mixture of donor and acceptor materials within the active layer to create a three-dimensional network of junctions [51].

Organic solar devices have two types of architecture; direct or inverted. In direct devices, indium tin oxide (ITO) is commonly used as an anode combined with a

cathode which has a lower work function (e.g. calcium, magnesium or aluminium). An inverted device will commonly use ITO as cathode and a metal with a work function greater than ITO (e.g. silver, gold or copper) [55].

2.2 Dye-sensitised Solar Cells (DSSCs)

DSSCs have three main components (illustrated in Figure 2.3), a dye-sensitized metal-oxide photo anode, a hole transport material (traditionally a liquid electrolyte), and a highly catalytic counter electrode. These are sandwiched in between transparent conductive electrodes [52].

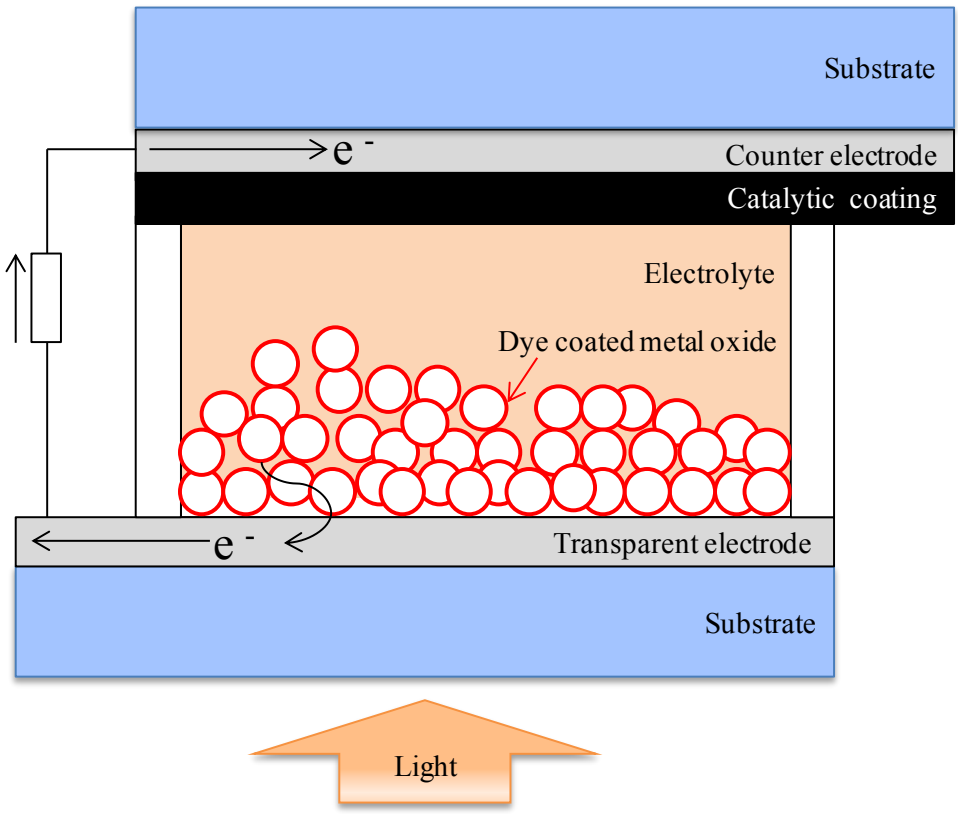

Figure 2.3 - Illustrative structure of a DSSC

Under illumination, the dye molecules will capture energy in the form of photons. The dye molecules then become excited and charge separation occurs at the interface of the metal oxide and the dye. Electrons are ejected into the adjacent metal oxide

particles and "holes" (an electric charge carrier with a positive charge, equal in magnitude but opposite in polarity to the charge on the electron) are left behind on the dye molecule. The injected electrons travel through the metal oxide particles and reach the transparent conductive electrode. When a load is connected, the electrons move to the counter electrode through the external circuit and are finally reunited with the holes through the redox couple present in the electrolyte [56].

2.2.1 Transparent conductive electrode

Solar cells require at least one transparent electrode to allow sunlight to reach the active components of the cell. The transparent electrode can have a significant influence on the overall electrical conversion efficiency of the device and it has been reported that ideally the transparency should be at least 90 % and it should have a sheet resistance of less than 10 Ω/square [57]. Indium Tin Oxide (ITO) is a widely used transparent conductor that has high conductivity, high transparency and good environmental stability. Indium is a by-product of zinc production and is one of the rarest materials, existing at approximately 0.05 parts per million (ppm) in the Earth's crust [58, 59]. The demand for indium-tin oxide has increased dramatically over recent years as touch screen technology and liquid crystal displays have become a popular household technology. In 2013, the global production of indium was 670 tons, of which over 75 % was used for ITO [59].

However, ITO is known to be brittle, with poor thermal stability resulting in layers peeling off and surface defects in modules [60]. Thin film ITO is usually manufactured using sputtering, a slow and costly vapour-phase process in which only 30 % of the material in the sputtering target is deposited onto the substrate [61]. ITO suffers from high ohmic resistance when deposited over large areas; to combat this thin conductive metal strips have been successfully applied to improve the

performance [62]. However, when applied to solar cells this can reduce the overall area exposed to sunlight. For these reasons, the currently preferred transparent conductor for DSSC applications is fluoride tin oxide (FTO), which has similar properties at a lower cost.

Alternative materials are also being investigated to optimize the potential for large area commercialization of electronic products such as thin film photovolatics and organic light emitting diodes (OLEDs). Materials being investigated include conductive polymers and carbon-based materials. Conductive polymers alone have not resulted in high conductivities and relatively low sheet resistance. A conductivity of 900 S/cm and sheet resistance of 300 Ω/square can be produced using a poly(3,4-ethylenedioxythiophene) polystyrene sulfonate (PEDOT:PSS) with dimethyl sulfoxide (DMSO) [63]. This is in comparison to ITO which has conductivities between 3000-5000 S/cm and a sheet resistance as low as 5 Ω/square [64]. Therefore, conductive polymers are often doped with more conductive materials such as carbon nanotubes or graphene to produce higher efficiencies [65-68].

2.2.2 Metal oxide materials

Titanium dioxide (TiO_2), zinc oxide (ZnO), and niobium pentoxide (Nb_2O_5) have been identified as the best candidate materials for efficient electron transfer within DSSCs in view of their electronic band structure [28]. The use of nanoparticles within the metal oxide layer is essential to increase the surface area available for dye adsorption. TiO_2 is the most widely researched, as it is chemically stable, non-toxic, readily available and has delivered the highest conversion efficiencies [69]. The conversion efficiency of a solar cell provides a standard measure for comparison and is defined as the ratio of energy output from the solar cell to input energy from the sun [47].

TiO_2 is a wide bandgap semiconductor, which is transparent in visible light and captures a wide ultraviolet (UV) range. TiO_2 has three main crystal phases, anatase, rutile and brookite. Of the three phases, anatase has the largest band gap energy of 3.23 eV, followed by brookite with 3.14 eV and rutile has the lowest of 3.06 eV [70]. Brookite is the least studied TiO_2 photo catalyst due to the difficulties obtaining it as a pure phase [71]. The anatase phase shows higher photo catalytic activity than rutile and is the most widely used form used in DSSC applications [72]. When illuminated with UV light, charge carriers are created which can be used to generate a current, induce chemical reactions or emit light. This is known as photo generated catalysis.

The photo catalytic activity of TiO_2 increases with decreasing particle size, due to an increase in the specific surface area [73]. This holds true until it reaches a critical particle size of approximately 10 nm, after which a loss in photo catalytic activity can be observed [74]. Below a particle size of 10 nm, the "wide bandgap and the high probability for electron/hole surface recombination results in a loss of photoactivity under visible light" [75]. Figure 2.4 illustrates how the TiO_2 particle size and layer thickness influence the electrical conversion efficiency of the cell [76]. From this we can infer that minimising the particle size within the TiO_2 ink layer should result in the best photo catalytic activity. The use of small particles also increases the surface area per square unit of the TiO_2 electrode (roughness factor) providing greater porosity. The surface area and porosity of the TiO_2 layer is an important factor which influences the amount of dye molecules that can be adsorbed within the film and constitutes a key parameter ruling the performances of DSSCs. A film with a porosity of 50% can increase the surface area by over a thousand times. The specific surface area and mean pore size data can be deduced from Nitrogen sorption experiments [77].

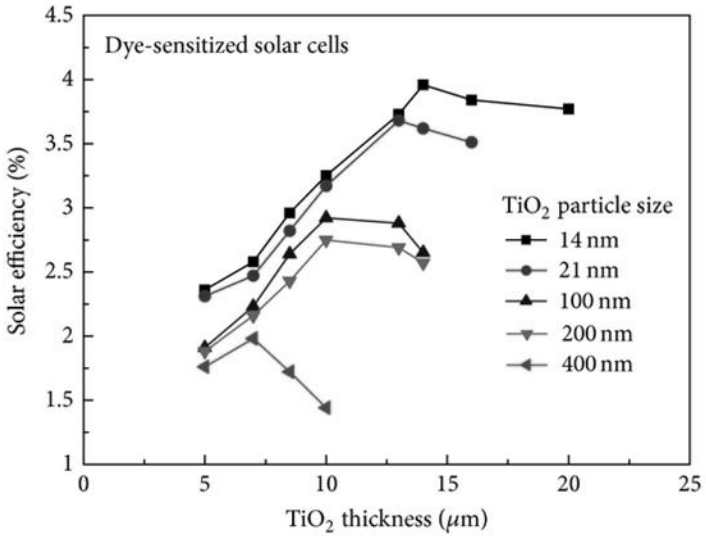

Figure 2.4 - Influence of TiO_2 particle size and layer thickness on efficiency

(From [76])

Following deposition, the TiO_2 layer within DSSC is traditionally followed by sintering at temperatures of 450 ºC or above. This sintering step has several functions. Firstly, it burns off some of the organic binder material to create a porous material in which dye can penetrate the film and attach to the TiO_2 particles. Secondly, it fuses together some of the TiO_2 particles to promote the inter-particle connection within the material and lastly it improves the contact between TiO_2 and FTO coated substrate to provide strong adhesion and reduce the risk of delamination [31]. These adhesive and mechanical properties significantly affect the overall performance of the device. However, high temperature sintering cannot be used alongside heat-sensitive substrates and therefore several alternatives are being considered. Mechanical compression has been used to replace heat treatment, resulting in crack-free films between 7 µm and 14 µm thick [33, 34]. Infra-red radiation has also been successfully used to sinter the TiO_2 printed layers within 12 seconds [17].

It has recently been discovered that treatment with titanium tetrachloride ($TiCl_4$) prior to and post sintering has been shown to significantly improve the performance of TiO_2 DSSCs [78]. The first treatment improves the bond between the FTO and the TiO_2, whilst blocking charge recombination between electrons in the FTO, with holes in the electrolyte. The second treatment adds a 1 nm TiO_2 coating onto the TiO_2 particles (as illustrated in Figure 2.5), which increases the surface roughness factor resulting in more dye molecules attaching to the surface of the particles [79]. $TiCl_4$ is a hazardous material that, when comes into contact with moisture, releases hydrochloric acid vapour and titanium oxychloride smoke. Both of which can cause chemical and thermal burns on contact with skin or eyes and respiratory damage on inhalation. $TiCl_4$ treatment therefore must be undertaken in ventilated areas which may not be suitable for roll-to-roll coating [80].

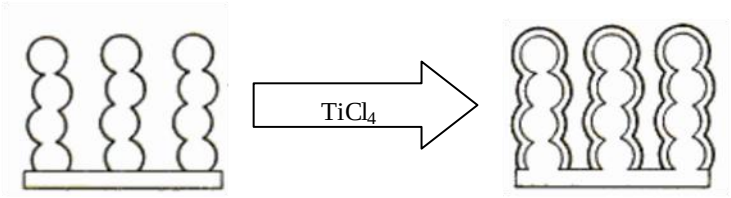

Figure 2.5 - Influence of $TiCl_4$ post-sintering treatment on the structure of DSSCs (From [81])

Zirconium oxide (ZrO_2) has been utilized as an inexpensive and environmentally friendly alternative post-sintering treatment material for photo electrodes. ZrO_2 post-sintering treatment has been shown to improve the connection of nanoparticles, reduce the particle size, and increased the specific surface area to improve the dye adsorption.

Table 2.1 shows how the energy conversion efficiency of ZrO_2 oxide post-treated TiO_2 films was shown to be similar to that of $TiCl_4$ post-treated films [82]. Thin coating of Nb_2O_5 or ZnO on top of the TiO_2 layer prior to dye sensitization has been also shown to reduce recombination losses in DSSCs [83]. Furthermore, Nb_2O_5 coated with a thickness of approximately 2-3 nm has shown to increase the efficiency by 1.4 % [84].

Table 2.1 - Influence of $TiCl_4$ and ZrO_2 treatment on short circuit current, open circuit voltage and efficiency of DSSCs (From [82])

Type	Short circuit current (mA/cm^2)	Open circuit voltage (V)	Fill factor	Efficiency (%)
Untreated	8.45	0.7	0.63	4.35
Post treated with $TiCl_4$	13.19	0.74	0.64	7.28
post treated with ZrO_2	12.61	0.73	0.66	7.03

The thickness and the morphology of the metal oxide layer have a strong influence on the photo electrochemical properties of the solar cells. Thicker layers are expected to adsorb more dye and therefore result in higher conversion efficiencies. However, thicker layers also adversely impact the efficiency in several ways [35]:

- the electrons within the dye cannot be injected to the electrode effectively due to the long distance needed to travel and hence the photocurrent is increased
- a decrease in the transmittance reduces the incident light intensity to the dye
- there is a poor charge recombination between the materials

There is therefore an optimal thickness for the mesoporous oxide material. Several studies have investigated the relationship between the thickness of the mesoporous

oxide layer and the conversion efficiency. The results vary significantly, with optimum film thickness of TiO_2 reported is from anywhere between 9.5 µm and 20 µm [76, 81, 85-89]. Many of these are difficult to compare due to differences in materials (e.g. TiO_2 particle size and dye adsorption) and architectures reported.

ZnO has been used as a photo anode in DSSCs as it has a band gap energy of 3.3 eV, similar to that of TiO_2 anatase, which has a band gap of 3.2 eV [90] and both have similar electron affinities. ZnO is also stable against photo corrosion and is inexpensive. The material is also commonly used as a buffer layer in organic solar cells and is therefore a material of significant research [91]. Despite the superior transport properties of ZnO, cells developed using the material still result in inferior performance; this has been attributed to the fact that ZnO is less efficient at injecting electrons from excited dye molecules [92].

Nb_2O_5 has also been shown to be a suitable alternative to TiO_2 [93], however it is not as widely available as TiO_2 nanomaterials due to it being produced on a large scale as a pigment in paints [94] and as a UV absorber in the cosmetics industry [95].

One possible way to improve the transport properties is to grow the electrode materials as nanoparticles, nanowires, nanotubes, and nanofibers [28]. However, this is a relatively new area of research so the cost and time required undertaking such processing is still unknown.

2.2.3 Dye sensitizers

The dye is a key component of the DSSC that captures energy from light and injects electrons into the conduction band of the metal oxide nanoparticles. Over the past two decades several materials have been studied to provide desirable properties [60]:

- strong light absorption in the visible and near infrared (IR) range
- good solubility in organic solvents
- ability to anchor to the metal oxide surface
- suitable electronic energy level alignment
- good thermal and chemical stability

Metal complex dye sensitizers have been used in DSSC devices to produce efficiencies of 12 %, however recently organic-based sensitizers have received more attention due to their ease of synthesis [96]. Dyes which function well are often polypyridine complexes of ruthenium with one or more carboxylic acid groups as a peripheral substituent [60]. These dyes are very good at capturing light at low wavelengths (300-550 nm), making them an ideal power source for low light environments.

The conversion of light into electricity at wavelengths within the visible range (390 to 700 nm) makes DSSCs an attractive power source option for portable and mobile electronic devices which are primarily used indoors or outdoors in diffuse light [97]. The use of dye sensitizers in a wide range of colours e.g. blue, green, orange, red and yellow, also make them aesthetically attractive option for integration into solar shading and windows [98]. The use of multiple dyes has also been reported to enable absorption of light from a wider wavelength [99].

2.2.4 Liquid redox electrolyte

The most advanced DSSCs incorporate an iodine/triiodide electrolyte to produce power conversion efficiencies of more than 11%. These are typically prepared in a solution of acetonitrile or neat N-methoxypriopionitrile (MPN) which have low boiling points and limit use of devices above 80 ºC, also leading to stability

problems such as short lifetimes and leakage issues [10]. For DSSCs to compete with current commercially produced silicon solar cells there is the need to increase power conversion efficiencies, increase the lifetimes up to 20 years and reduce the overall fabrication costs. Therefore, it is assumed by many researchers that the current use of a liquid electrolyte is not the ideal architecture to meet these targets.

2.2.5 Organic hole transporters

The hole transport material facilitates the transport of charge between the metal-oxide coated electrode and the counter electrode. Solid state DSSCs (ss-DSSCs) were developed to replace the liquid electrolyte with a material which, when dried, becomes solid. This is seen as the most likely route to large scale production of DSSCs and therefore significant research is being undertaken to investigate gel or solid-state electrolytes. These ss-DSSCs also have the potential to achieve higher power conversion efficiencies than the traditional liquid- electrolyte [60].

The highest reported efficiency for a DSSC incorporating a liquid electrolyte (at the time of writing) is $11.9 \pm 0.4\%$ [100]. However, the maximum theoretical efficiency for these cells (incorporating ruthenium/iodine/triiodide) is 13.8%; to improve beyond this will require improved dyes and electrolytes [101]. Dye regeneration with solid-state devices occur several orders of magnitude faster than in the iodine/triiodide redox couple, therefore efficiencies of more than 20% are theoretically possible [101]. Solid state devices typically incorporate indoline dyes (such as D102, D149 or D205), which require much thinner films and produce cells with efficiencies between 4-6 % [10]. Efficiencies of up to 7% have been achieved by using spiro-MeOTAD [2,2' ,7,7'-tetrkis(N,N-di-p-methoxyphenylamine)-9,9-spirobifluorene] as the hole conductor [1]. However, spiro-OMeTAD, has a commercial price that is more than 10 times that of gold and platinum [102]. High

device efficiencies for solid-state devices are achieved by incorporating two additives into the hole transport material; 4-tert-butylpyridine (tBP) and an ionic salt typically lithium bis-trifluoromethanesulfonimide (LiTFSI).

Solid state devices require much thinner metal oxide layers; with an optimum thickness of between 0.65 µm and 2 µm reported (with a spiro-OMeTAD hole conductor) [15, 103, 104].There are possibly two reasons for this. The first is that the hole conductor, spiro-OMeTAD has relatively large molecules in comparison to traditional liquid electrolyte transport materials, which results in insufficient pore filling. The second is that the back electron recombination is approximately twice as fast than that of the traditional liquid electrolytes, resulting in the effective electron diffusion length reduced to 1µm [60]. This opens up opportunities for the use of alternative single-step coating techniques to be used to manufacture the TiO_2 layer such as a dip-coating technique, which has been shown to produce efficiencies favourably to that of traditional screen-printed films. Synchrotron x-ray diffraction has been used to show that the repeated deposition and thermal treatment of eight layers produced larger pore and particles sizes in the bottom layers due to repeated calcinations [105]. The resultant film had a thickness of 1.9 µm and was developed into a ss-DSSC resulting in an efficiency of 4.63 % [105].

Conjugated polymers have also been investigated to replace the liquid electrolyte in standard DSSCs due to their high conductivity and tuneable optoelectronic properties. The most successful examples include the use of poly(3-hexylthiophene)(P3HT) and poly(3,4-ethylenedioxythiophene) (PEDOT), which result in efficiencies of 3.2 % and 6.8 % respectively [9, 15].

2.2.6 Counter electrode

The counter electrode plays a very important role in DSSCs by providing a catalytic surface that greatly enhances electron transfer to the electrolyte. This in turn increases the charge density in the solar cell which directly translates to higher photo-currents and efficiencies. To prevent losses at the counter electrode, the rate of electrolyte reduction should be comparable to the rate of dye regeneration by the electrolyte at the photo anode [106]. The counter electrode within a traditional DSSC requires a high catalytic activity and low resistance. Platinum is often used because it possesses both of these properties, whilst providing high corrosion stability against iodine in the electrolyte.

Concerns over platinum's cost and stability has led to research which is investigating alternative catalysts [107, 108]. Carbon based nanomaterials (e.g. carbon black [109], carbon nanotubes [66, 110], graphite, graphene [65] and graphene oxide [21]) have been investigated as a counter electrode in DSSCs due to their good electric conductivity and high surface area and are thought to be the most promising low cost alternative to platinum. Of these, carbon black is one of the cheapest to produce and is widely available due to its use as a colour pigment in ink, paint, and copy machines toners, however its main use is as an additive in manufacturing of tyres in the rubber industry [111]. Carbon black was first used as a counter-electrode in 1996, resulting in a power conversion efficiency of 6.7% [112].The efficiency of carbon black as a counter electrode in DSSCs greatly depends on the thickness of the layer, for example a 14.47 µm layer is reported to result in an efficiency of 9.1%, a 9.79 µm layer is reported to result in an efficiency of 8.4% and a 3.09 µm layer is reported to result in an efficiency of 7.5% [109]. In solid-state DSSCs the counter electrode materials are commonly thermally evaporated metals of silver or gold.

Reflective metal contacts have been recognized to increase the short circuit current density (I_{sc}) in solar cells by reflecting transmitted light back into the solar cell [113].

2.3 Printed electronics

The use of the term printed electronics refers to the manufacture of electronics beyond classical silicon approaches [61]. Printed electronics combines non-traditional materials (often solution-deposition or vacuum-deposition techniques) and large area, high volume deposition techniques to manufacture electronic components. It is a developing area of research in many fields including PVs, flexible displays, lighting (including electroluminescent and organic light emitting diode (OLED) products), electronic components and integrated smart systems (including sensors and textiles) [61, 114, 115]. Manufacture of a printed electronic device requires the understanding of several separate disciplines including materials science, chemistry, device physics, system integration, production engineering, software, mechanical engineering and electronics. It is therefore a complex, multidisciplinary research field.

Printed electronics opens the possibility to integrate low-cost electronic function directly in the production line to add unique features to products. For example, components such as batteries or lights can be directly printed within a device to reduce the number of manufacturing steps. Although many of the inks and raw materials, especially the organic semiconductors are currently still relatively expensive, only a small amount of material is needed with minimal waste. In contrast, traditional silicon technology needs to use a whole wafer made from highly pure material followed by the use of subtractive technologies, which results in high material losses.

Roll-to roll printing techniques involve a substrate that is unwound from a roll to allow for continuous printing or coating. Several treatment steps (including heating, drying, UV curing etc.) and further layers can be added as required. A detailed comparison of the film-forming techniques for roll-to-roll production can be found in a review by Krebs (2009) [3].

2.3.1 Screen printing and doctor blade coating

In screen printing, a stencil is applied to a woven material (synthetic fibre or steel mesh) that is stretched over a frame. The stencil is impermeable to the ink and blocks all openings except the patterned area. Ink is transferred to a substrate after being forced through the openings in the stencil using a squeegee. The thickness of the coating is determined by the thickness of the solution and the screen [3].

Doctor blade coating is a technique used to form films with well-defined thicknesses. The technique works by placing a sharp blade a fixed distance from the surface that needs to be covered. The coating solution is then placed in front of the blade and the blade is moved across in-line with the surface, creating a wet film. The technique should ideally have solution losses of about 5%, however practically it takes time for optimal conditions to be found [3].

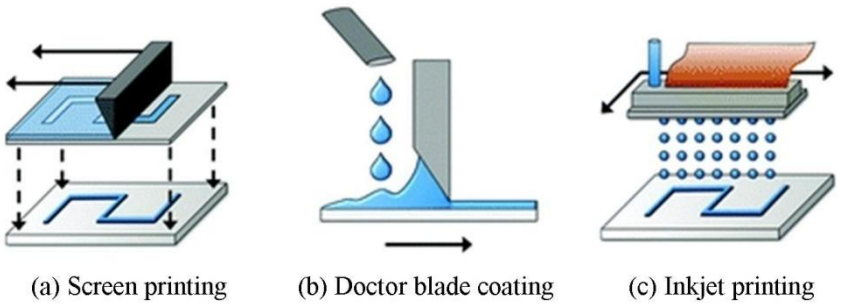

Figure 2.6 - Illustrative comparison of deposition techniques

(From [116])

Doctor blade coating and screen printing are the most reported methods to produce the nano-structured metal-oxide layer within DSSCs [23, 117]. The inks/pastes used in these processes usually require large amounts of binders and thickeners to produce the high viscosities (1000 to 10,000 cP) required for reproducible and reliable production of films [118]. Viscosities can be increased with the addition of polymeric additives such and glycerol or ethylene glycol or ethyl cellulose [119]. However, high temperature curing of between 450-500 ˚C are required to completely remove these large amounts of material from the printed layers without damaging the printed materials or underlying layers [120].

2.3.2 Inkjet printing

Inkjet technologies can be described as the "digitally controlled ejection of drops of fluid from a print head onto a substrate" [121]. Most systems operate by dispensing droplets one at a time as the print head moves in the X direction and the substrate moves in the Y. More advanced systems also incorporate a Z movement. It is a non-contact method that can be used on a wide range of substrates including flexible and three-dimensional geometries. Since inkjet printing uses liquid forms of materials dispersed in a solvent, it is critical to understand the ink deposition processes to determine the limitations of the technique.

The technology is broadly divided into two categories, continuous inkjet (CIJ) and drop-on-demand (DOD). CIJ printers produce a continuous stream of droplets from the nozzles whereas DOD printers produce droplets only when prompted to do so. There are similarities between the two methods. Firstly, they both use a pump to provide suction and to prevent ink leaving the nozzles when they are not in use; it can also be used to provide pressure to flush the nozzles with cleaning fluid. They both use an electric motor to correctly position the nozzles above the substrate to

produce a pattern. This is either done by moving the nozzles (print head) themselves, the substrate or both.

CIJ systems produce a continuous stream of droplets from a nozzle which is directly connected to a reservoir. As the stream of droplets fall toward the substrate, they pass between two electrostatic charging plates. When required, a selection of these electrostatically charged droplets can be deflected, collected in a gutter and recycled. The technology does not suffer from nozzle clogging due to the fact that there is a constant stream of droplets. This enables a high drop frequency and also has the ability to use volatile solvents which allows for a faster drying and increased adhesion to substrates. A high pressure pump forces the liquid through the nozzles which enables printing at large distances from the substrate due to the high drop velocity. These points combined make possible high speed printing for applications such as data coding of products and is most commonly used in industry to produce expiry dates on pots and bottles [2]. However, CIJ results in a relatively low print resolution due to the fact that there is less control over the droplet positioning and has limitations due to the requirement for the print fluid to be electrically charged. The technique is also known for requiring high maintenance and is perceived to be environmentally unfriendly due to the solvents used [121]. CIJ systems are not commonly used to manufacture printed electronics due to the fact that the quality of the functional inks is compromised when exposed to environmental conditions during the ink recycling process [122].

As previously mentioned, DOD systems only eject drops when required; generally formed by the creation of a pressure pulse. These systems can be further divided into thermal and piezoelectric printers. Thermal inkjet printers operate by rapidly heating the ink inside a reservoir using a resistor connected to a power supply [123]. A film

of ink is developed directly above the heater, which vaporises producing an air bubble. The resultant air bubble causes a pressure pulse, which forces a drop of ink through the nozzle [122]. Thermal inkjet printing has the potential for small drop sizes, high nozzle density and low print head costs. However, the heating element can lead to degradation of the functional material and is limited in the range of solvents that can be used [124].

Piezoelectric printers contain a piezoelectric crystal within the ink reservoir, which changes shape when a voltage is applied [2]. This piezoelectric element means that the resultant print head is significantly more costly than the thermal print heads. The drop size and shape can be carefully controlled by adjusting the waveform, meaning that a range of inks and materials can be printed to the pattern required [123]. Smaller droplets can produce patterns of high resolution whereas larger droplets can be used to cover larger areas and therefore increase the print speed. Adjustment of the peak voltage, voltage pulse time and the shape of the waveform applied to the piezo-element can affect how the droplets are deposited [2, 123-125].

The motion of fluid within the ink chamber starts when a positive voltage is applied across the piezoelectric element. This causes the ink within the chamber to enlarge, creating a negative pressure inside. When the voltage drop is applied to the element, the piezo-element expands resulting in a wave of pressure. When the pressure is high enough to overcome the viscous drag and surface tension of the ink, a droplet is forced out of the nozzle. As the ink is forced out, elongated droplets fall to the surface and form spherical drops. The surface tension of the ink determines how easily a drop is formed. If the surface tension is too low, the ink will spread over the nozzle plate resulting in a skin [126]. If the surface tension is too high, the pressure

within the ink reservoir will not be enough to overcome the surface tension and produce a drop.

2.4 Formulation of functional inks

Inkjet printers require specific fluid properties to enable them to print reliably and consistently. As previously mentioned, the two key factors that affect the quality of the resultant print are viscosity and surface tension. However, particle based inks will also need to ensure that particles and agglomerates are small enough to pass through the nozzles [127]. The pH of fluids should also be considered to avoid corrosion and damage the print head (usually in the range of 4-9) [128]. It is also important to prevent the formation of bubbles during printing; this can be done by degassing the ink prior to use [124].

Ink formulations are often kept a highly guarded secret by manufacturers. Successful formulations require good drop formation, wetting and functional performance. Table 2.2 provides the key components of inks alongside typical loadings. Usually a functional material is dispersed in a solvent with at least one other component to make them printable. For example, mixtures of water and common alcohols such as ethanol or isopropanol can produce solutions with appropriate surface tensions but result in a viscosity which is too low for successful jetting. Therefore, a variety of solvents and additives can be used to optimize formulations and an iterative approach to achieving proper viscosity and surface tension may be necessary.

Table 2.2 - Typical compositions of inks (From [125, 129, 130])

Component	Function	Loading (w/w%)	
		Low	High
Functional material	Key component	0.1	10
Solvent	Dispersion medium	50	90
Co-solvent	Controls drying Modifies surface tension	0	50
Surfactant	Modifies surface tension Improves wetting	0	5
Viscosity modifier	Generally increases viscosity	0	30
Humectant	Prevents ink drying	0	30
Other	pH buffer, dispersant, de-foamer, binder	0	1

2.4.1 Solvent carrier

The role of a solvent within an ink is a carrier to deliver the functional material to the substrate. The solvent is then removed via a drying process. The carrier solvent is usually the largest constituent within an inkjet ink and therefore has a huge impact on the overall properties of the ink. The choice of solvent is also important to determine which additional ingredients can be added. One of the most important factors to consider when choosing a solvent is the evaporation rate. Inks should contain solvents that evaporate slowly (usually high boiling point solvents) to prevent the nozzle from drying out and nozzles from clogging [131]. However, this may increase the drying time of the ink when deposited onto the substrate. A common solution for this is to use a mixture of solvents with a high and low evaporation rate [122]. The addition of a co-solvent with a higher boiling point and lower surface tension than the main solvent, acts as a drying agent. The drying agent induces a circulating flow within the ink droplet as the ink evaporates, leading to a

uniform placement of nanoparticles over the surface of the droplet [24]. Another solution is to add a polymeric material such as glycol to reduce the rate of evaporation for aqueous solutions [128].

A further consideration during ink formulation is the compatibility with the adjacent layers. Solvents must be carefully selected to ensure that they do not cause damage to the underlying layer during printing. This usually suggests that each layer must alternate its solubility, usually based on polar / non-polar pairs. The use of post-treatment, such as sintering is also likely to reduce the solubility of underlying layers.

2.4.2 Surface tension

Repeated development of inks has determined certain restraints for fluid properties. Table 2.3 outlines some of the problems which can arise if inkjet fluids fall outside the desired properties. However, as will be discussed later, the nature of substrate will also influence how the ink interacts and the formation of the film. Surface tension and viscosity are two of the most important factors to consider when formulating an ink. The surface tension of the ink should be matched to the specific printer and must be high enough to hold the ink in the nozzle without dropping. A surfactant can be added to solutions to increase the surface tension. Water is low-cost solvent with low environmental impact which is widely used in the development of inks for graphics printing. However it also has a high surface tension; approximately 72.80 mN/m presenting a challenge for formulation of aqueous inks [132].

The ideal surface tension of an ink must be high enough to be held in the nozzle and avoid a premature droplet, but must also be low enough to allow the droplet to spread over the substrate surface resulting in the formation of a continuous film. The

interaction of an inkjet printed droplet with a substrate is very important factor when considering the quality of the final print. When a droplet hits the substrate, the relationship between the surface energy of the substrate and the fluid will mainly determine whether wetting will occur. As the droplet impacts the surface of the substrate, it will deform as shown in Figure 2.7. Depending on the substrate, the final drop diameter on the surface (D3) is generally 2-4 times the drop diameter in flight.

Table 2.3 - Restrictions on fluid properties (From [127, 128, 133, 134])

Property	Value		Problems	Controlled by
	Min	Max		
Viscosity (μ)	2 cP	20 cP	Low viscosities result in droplet breakup and excessive spreading High viscosities have long droplet tails or are unable to exit the nozzle	Solvent Co-solvent Viscosity Modifier
Surface tension (γ)	25 mN/m	40 mN/m	Too low and the nozzle plate becomes wetted making it difficult to jet Too high results in poor drop formation	Solvent Co-solvent Surfactant
Particle size	0 nm	1% of nozzle diameter	If the particle sizes are too large, it results in rapid nozzle clogging	Dispersant Surfactant
Zeta potential (ζ)	30 mV	As high as possible	Too low and the dispersion is not stable	Dispersant Surfactant
pH	4	9	Corrosion within the print head	pH buffer

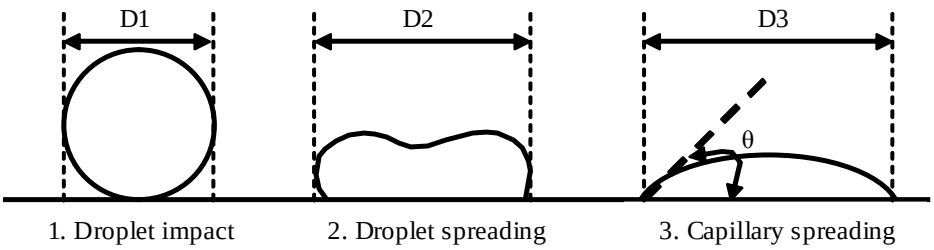

Figure 2.7 - Illustration of droplet spreading and contact angle (θ)

The roughness of the printed materials can have a bearing on the performance of a solar cell and other printed electronic devices. Printed conductive electrodes are only between 40-300 nm thick and non-smooth layers suffer the risk of failures at localized thin or thick points [122]. Surface roughness also dramatically affects the electrical conductivity of thin films and therefore is an important parameter to consider for the electrode layers. However, as previously discussed for the mesoporous layer of metal oxide nanoparticles within DSSCs, good porosity is important to adsorb the maximum amount of photosensitizer material.

Producing smooth, uniform films can be an issue when using solution processing techniques such as inkjet printing. With each of these techniques a droplet is deposited from a nozzle, producing overlapping discs on a substrate. In an ideal situation, each disc overlaps to form a continuous film. Uneven distribution of droplets can result in an unsmooth surface and may also leave pinholes in the film. Figure 2.8 illustrates how the spacing of drops on a substrate can influence the morphology of the deposition.

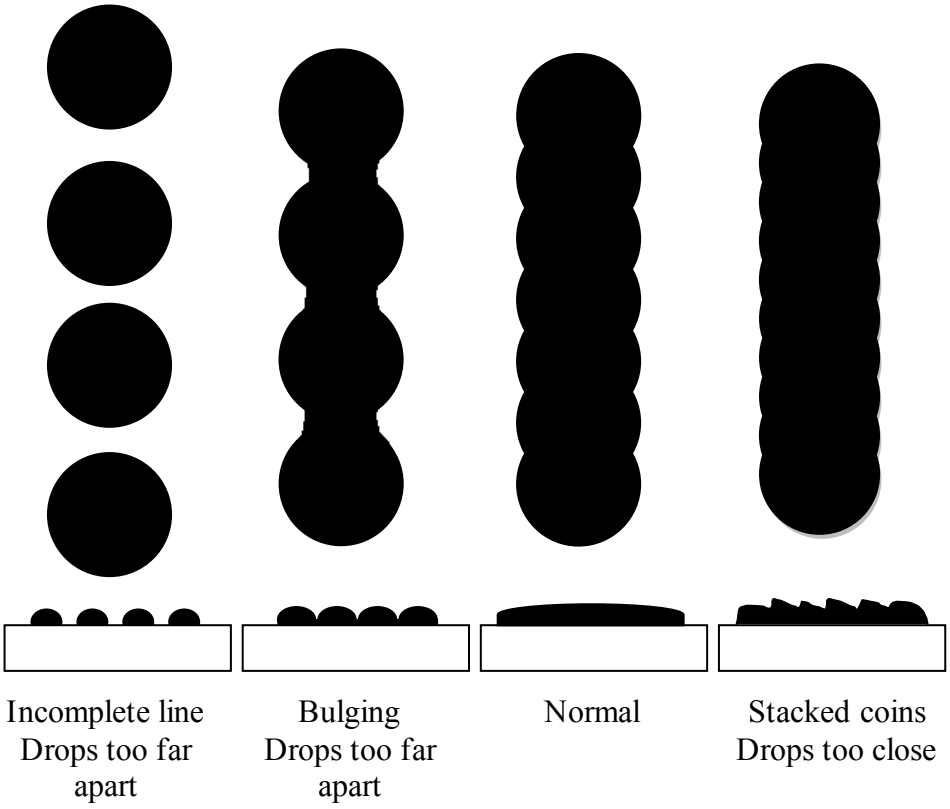

Figure 2.8 - Illustration of line morphologies occurring from drop spacing.

2.4.3 Viscosity

The ideal viscosity of an ink allows a droplet to be ejected from the nozzle and result in appropriate spreading of the droplets on the substrate [128]. The viscosity also has a huge influence on the reliability of printing and research suggests that for drop-on-demand printers a viscosity of less 20 cP should provide good droplet formation [127]. However, low viscosity inks make it more difficult to maintain particle stability and sedimentation is more likely to occur, increasing the potential for jetting reliability issues or premature print head failure. Inkjet fluids are commonly characterized by their zero shear rate viscosity however shear thinning behaviour can be established by measuring apparent viscosity using oscillation rheometers. The presence of polymers, particles, dispersants, binders, and other components can all

affect the viscosity and viscoelastic properties of an inkjet fluid. The inkjet printing process usually involves high jet speeds, typically more than 6 m/s, considering that the process is likely to be moved to high throughput industrial applications, and printing speeds are likely to be increased even more. This results in high shear rates in excess of 1000 s^{-1} and therefore it is important to investigate how inkjet fluids perform under these conditions.

There are several ways in which the viscosity of an ink can be controlled. Increasing the temperature of the ink can decrease the viscosity of the ink significantly. For example, a temperature increase of 5.5 °C can reduce the viscosity by more than 50% [135]. The viscosity of ink depends on the components of the ink, including solvent carrier, dispersing agents and additives. Many inks use water as the carrier solvent and therefore achieving the relatively high viscosities required for piezoelectric printing can be a challenge. In many printers the print head can be heated to lower the working viscosity of the ink, however this severely influences the lifetime of the print head and therefore manufacturers of inks often develop inks suitable for printing at room temperatures [128]. High temperature may also degrade functional components within certain ink formulations.

Viscosity modifiers can also be added, however these may need to be removed after deposition to avoid any negative influence on the films' performance. The rheology of inks and pastes are often controlled by the addition of an organic polymer or binder. Binders are an important component to control film thickness, reduce the likelihood of cracking and improve substrate adhesion. Polyethylene glycol (PEG), polypropylene glycol (PPG), polyvinylpyrrolidone (PVP), polyvinyl alcohol (PVA), polyacrylic acid (PAA) or cellulose derivatives are all examples of commonly used binder materials. Ethyl cellulose (EC) is a well-known binder used in the formulation

of TiO_2 pastes for dye sensitized solar cells [29, 32, 136]. EC is insoluble in water and therefore methyl cellulose (MC) or hydroxyethyl cellulose (HEC) are used for water-based ink formulations [137].

2.4.4 Functional materials

Original inks developed in the 1980's used water soluble colourants; however the industry required better colourants to provide quality and durable images. Carbon black nanoparticles were introduced as a solution to provide high-colour image performance. To make inkjet inks, these nanoparticles needed to be dispersed into a stable solution. At the nanometre scale, materials exhibit properties that differ significantly to their bulk properties. In particular there is a natural tendency for nanoparticles to cluster together. These are known as either aggregates or agglomerates, depending on the nature and strength of the bonds between the particles (illustrated in Figure 2.9). This poses a particular challenge when formulating inkjet inks which incorporate nanoparticles as a functional material. For successful jetting, the particles within the fluid should be 100 times smaller than the nozzle opening [128]. The fluids should be filtered through the correct size filter just before loading into the cartridge to remove large particle agglomerates which can clog the nozzles.

By minimizing the number of these agglomerates, a good quality ink can be achieved. The energy of simply stirring particles into a solution is not great enough to overcome the particle attractive forces between particles and breakup the agglomerates [95]. Ball milling, high shear mixing or ultrasonication are commonly used to break up agglomerated nanoparticles [138]. Ultrasonication produces shock waves caused by collapsing cavitations. This causes particles to collide and any agglomerated particles are eroded and split apart [139].

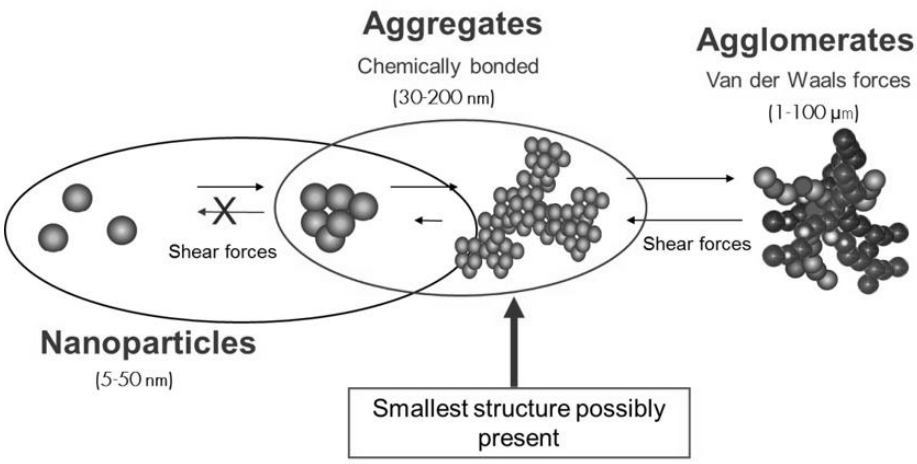

Figure 2.9 - Illustration of nanoparticles, aggregates and agglomerates

(From [95])

Particle size and dispersion of particles is a significant issue when formulating nanoparticle inks and requires a great deal of consideration to avoid irreversible blockage or clogging of printer nozzles. Particle-based inks are generally thermodynamically unstable and held in long-term suspension by electrostatic, steric or electro steric treatments:

- Electrostatic – charges are generated on the surface of particles to prevent or control re-agglomeration. The isoelectric point (IEP) is the pH at which a surface carries no net electrical charge [74, 140]
- Steric – molecules adsorb on to the surface of particles to introduce a barrier
- Electro steric – a combination of electrostatic and steric mechanisms

Particle dispersions are known as 'colloidal systems'. A colloidal system is where one of the three fundamental states (e.g. solid, liquid or gas) is finely dispersed in another. These systems are commonly found in everyday life (e.g. aerosols and emulsions) due to the special properties that they provide. A valuable measurement to understand the stability of a dispersion is the zeta potential (ζ) [140]. It is an

expression of the magnitude of repulsive or attractive forces acting between individual particles. A large negative or positive zeta potential suggests that particles within a suspension will tend to repel each other and flocculation is less likely to occur. Zeta potentials ± 30 mV are normally considered stable and a zeta potential of ± 15 mV is considered as the threshold for agglomeration [141, 142]. A detailed discussion of the theory behind zeta potential is not necessary for this project, only an understanding that the surface charge of particles influences how well it can be dispersed and that zeta potential provides a good indication of stability. It is important to note that zeta potential is generally a term applied to polar suspensions, such as aqueous solvents. One of the simplest ways to adjust the surface charge of particles is modify the pH of the solution. As the pH of a suspension is shifted away from neutral then the particles tend to acquire more charge, resulting in a more stable dispersion. A zeta potential value must always be considered alongside the solution conditions (pH, ionic strength, concentration of any additives). Dispersions are generally unstable when no charge is present (e.g. when the zeta potential is zero and the pH is at the IEP) [140].

2.5 Materials for printed electronics

There are several commercially produced functional inks developed for printing electronic components. These include several nano-metal silver inks [143-145] and a few sources of copper [146], gold [147, 148] and nickel [149, 150]. However, where commercial inks are not available, they must be formulated with the correct components to make them suitable. A review of currently available materials was undertaken to discover which can be utilised in the printing of DSSC devices.

The choice of materials to be used for printed organic and hybrid solar cells are not only crucial to the overall efficiency of the technology but also the printability and stability of the device. Electronic devices (including solar cells) use the passage of electrons to provide the required function. An electrode material is used to transmit these electrons through a device. An ideal electrode material, conducts well, with low losses in voltage or current due to resistance. In the majority of electronic devices two electrodes are used to provide a complete circuit, either made of the same material or two different materials. There are many different electrically conductive materials available, but only some of them are readily available in a form suitable for printing. The three primary groups of these materials are metallic colloids, carbon nanostructures, and conductive polymers, which will be covered in the following sections.

2.5.1 Metallic colloids

The most commonly used method to produce electronic circuitry is a photolithographic process. The process starts with a sheet of metal between 9 to 70 µm thick, which is patterned using a coating material sensitive to ultraviolet (UV) light. Once exposed to UV light, the material hardens and 75% of the remaining material is etched back off to produce the desired pattern [146]. After etching the hardened resist is removed in a strong alkali stripper. The process is very time consuming and wasteful, therefore an additive technique offers an alternative where the design can be quickly altered for different requirements [147, 151].

Metal nanoparticles have been investigated for use as conducting materials in electronic application due to good electrical properties and the ability to be dispersed in high concentration [2]. There are many types of metal nanoparticles available in

the market such as silver (Ag), gold (Au), copper (Cu) and nickel (Ni) [2]. Each has different benefits and limitations toward the application in printed electronics.

Table 2.4 - Resistivity and conductivity of common metals (From [152])

	Specific resistivity, ρ (Ω·m)	Conductivity, σ (S/m)
Silver	1.59×10^{-8}	6.30×10^{7}
Copper	1.68×10^{-8}	5.96×10^{7}
Gold	2.44×10^{-8}	4.10×10^{7}
Nickel	6.99×10^{-8}	1.43×10^{7}

Silver-based inks are frequently used due to bulk silver having the lowest resistivity of all the metal elements. Silver nano-particulate inks have been developed which incorporate stabilizing materials which decompose at temperatures close to 150 ºC, resulting in conductivities close to that of bulk silver [153, 154]. Reactive silver inks have also been developed from silver acetate and silver nitrate, which are conductive at room temperatures meaning that they can be dried at much lower temperatures [155]. Silver nanowires have also been incorporated into inks to produce well-defined patterns and high conductivities [22, 156, 157].

Gold nanoparticles have been widely used due to their excellent thermal stability [2] and high conductivity [158]. Gold nanoparticles have been formulated into an ink with small particle size (<10 nm) and narrow distribution which when sintered at 190 °C results in a resistivity of 1.0 $x10^{-7}$ Ωm, lower than that of the bulk material. Gold is a very expensive and rare material used in the manufacture of high quality electrical components [151].

Copper has comparable electrical conductivity to silver, is approximately 1% of the cost and is 1000 times more abundant [159, 160]. It is therefore being investigated as a low cost alternative to silver and gold [158]. However, the material tends to oxidize easily under ambient temperature which can affect the electrical performance of the material [2].One method to combat this is to coat the copper nanoparticles with a thin barrier layer (such as silver) to prevent oxidation of the copper core and preserves its metallic characteristic [161].

With all nanoparticle suspensions, sintering is required to remove unwanted materials such as solvent carriers and organic binders. For conductive particles this process also transforms the ink into a conductive, solid metal track [162]. Several methods have been previously used to sinter nanoparticles including traditional thermal sintering [155], infrared sintering [20], and microwave sintering [163]. Each of the techniques has different advantages and disadvantages. Thermal sintering can be quite time consuming, taking from 30 minutes to a number of hours in a conventional oven [164]. This also can result in damage to temperature sensitive substrates such as plastic or paper. In contrast, microwave and infrared sintering can sinter nanoparticles in a number of seconds speeding up the manufacturing process significantly [165].

2.5.2 Carbon nanostructures

Carbon has been explored for several applications as a replacement where metals would previously have been used, however, conductivity in carbon itself is approximately 200 S/m, significantly lower than in metals [166-168]. However, the electro catalytic performance of carbonaceous materials has been improved by doping nitrogen into the carbon structure resulting in higher electro catalytic activities and better stability than platinum [106]. These materials offer several

advantages over metals, including that they are naturally abundant, light weight and resistance to corrosion. It's first reported use as an electrode in dye-sensitized solar cells was in 1996 as a low cost alternative to the more traditionally used platinum or gold [112]. Carbon black is an intense black powder made by incomplete combustion or thermal cracking of a hydrocarbon feedstock. The main uses of carbon black are as an additive to provide colour in the manufacturer of plastic and rubber components, inks and paint [111]. However, it is also in the manufacture of electrical components due to its high conductivity, good electrochemical activity, and low cost. The resistivity of carbon black depends upon its origin, composition and manufacture process. More recently, carbon nanotubes, graphene and graphene oxide have all been used in the manufacture of electrical components due to their high electrical conductivity [169, 170].

2.5.3 Conductive polymers

Conductive polymers are a distinctive group of organic materials that exhibit the electrical and optical properties of both metals and semiconductors [171]. They have a wide range of practical applications due to their low cost, flexibility, conductive ability and ease of synthesis. Polyaniline, polyacetylene, polypyrroleand poly(3,4-ethylenedioxythiophene) (PEDOT) are the most intensively studied conducting polymers; an overview of each is provide below [172].

Polyaniline has been around for hundreds of years and was first reported in 1835 as “aniline black” [173]. It is a dark green powder in its conductive form and can be doped to produce high level conductivities. However one of the major limitations is that it has poor solubility in commonly known solvents such as sulphuric acid, methane sulfonic acid, formic and acetic acids. Polyaniline has however been

successfully used as a coating to prevent the build-up of static energy in electrical components [174].

Polyacetylene is a conducting polymer with one of the simplest structures. It was first found to conduct electricity in 1977 and later it was discovered that very heavy doping can produce conductivities similar to that of copper. However, the material was found to be very difficult to work with as it could not be easily dissolved, therefore other synthesis routes have since been investigated to enable the material to be dissolved into liquid precursors [175]. This development made it possible for the material to be printed or coated, opening up new applications in which the material could be used [176].

Polypyrrole is a conductive polymer that is commonly used for commercial applications due to its long-term stability. It was first reported in 1916 as "pyrrole black" by the oxidation of pyrrole with hydrogen peroxide to produce an amorphous powder. This powder could then be made into an aqueous solution or dissolved into organic solvents [177]. However the formation of films or coatings remains problematic, with difficulties in mechanical strength and shape control [178].

PEDOT was developed by Bayer in the late 1980s as an antistatic coating [171].It has excellent transparency, good electrical conductivity (in excess of 300 S/m) and shows good stability in air and humidity. It has also been found to be stable at relatively high temperatures, with the ability to withstand 125 °C for several thousand hours [179]. However, PEDOT is insoluble and therefore very difficult to work with. To enable commercial success PEDOT has been doped with the water soluble polyelectrolyte, poly(styrenesulfonate) (PSS) resulting in a good conductivity liquid solution known as PEDOT:PSS [180]. In addition, it is important

to identify the amount of PSS added into PEDOT as it does effect the stability and the quality of the overall dispersion process [181]. With more than 20 years of evolution, PEDOT has become one of the most commercially developed conductive polymers and has been extensively studied as a transparent conductor in electronics devices. Several additives have been found to increase the conductivity of PEDOT:PSS. Polar organic solvents, such as dimethyl sulfoxide (DMSO) have been shown to improve conductivity by up to three orders of magnitude, however this is still low in comparison to inorganic alternatives [63]. The addition of DMSO solvent which acts as a secondary dopant in the PEDOT: PSS solution has resulted in improved morphology and thus improved the conductivity [182]. The improvement of conductivity is related to the reduction of coulomb interaction between PEDOT and PSS charge [183]. The additive results in better charge transportation within the material [184, 185]. The addition of up to 10 wt% DMSO reduces the electrical resistance in PEDOT:PSS films while beyond this concentration, the resistance remains nearly unchanged [186]. Glycerol has also been used to enhance the conductivity whilst also providing better uniformity and smoother surface roughness [187, 188].

2.5.4 Semiconductor materials

Semiconductors usually form the main functional material of electronic devices. For example, one of the main materials within DSSCs is a large band-gap semiconductor. TiO_2 has already been identified as one of the best candidates, however to be applicable to inkjet processes the nanoparticles first need to be incorporated into an ink suitable for printing. The stabilization of metal oxide nanoparticles in both aqueous and non-aqueous solutions media requires a good understanding of the magnitude of the inter-particle forces and the surface chemistry

of the materials. To improve the performance of the cell, the primary particle size of the TiO_2 should be as small as possible as shown by Jeng, M.-J (2013). However, this is difficult due to the natural tendency of TiO_2 to form agglomerates.

Suttiponparnit, K (2011) adjusted the pH of TiO_2 solutions by adding hydrochloric acid (HCl) and sodium hydroxide (NaOH). They found that the pH at which the surface of TiO_2 carry no net electrical charge (the isoelectric point) varies depending on surface area of the particles [189]. They also reported several critical factors in creating stable dispersions for Degussa P25 TiO_2 (a widely available commercial TiO_2 nanopowder).

- An isoelectric point of approximately 6.2 was found, with significant agglomeration and large flocculation occurring near this value. The smallest particle size observed was approximately 200 nm with a pH lower than 4.0 or higher than 8.2, as shown in Figure 2.10.
- Higher ionic strength (IS) solutions resulted in larger hydrodynamic diameters. The lowest solution strength of 0.001M resulted in the smallest particle size and highest zeta potential.
- As the mass concentration of particles increased, the pH of the solution decreased.

Nitric acid and acetic acid are also investigated within the literature as methods to modify the pH of solutions. According to Ito, S (2007) [136] acetic acid is adsorbed on the surface of TiO_2 reducing the likelihood of agglomeration, whilst at the same time altering the surface charge of particles causes particles to repel each other and shifting the zeta potential to positive.

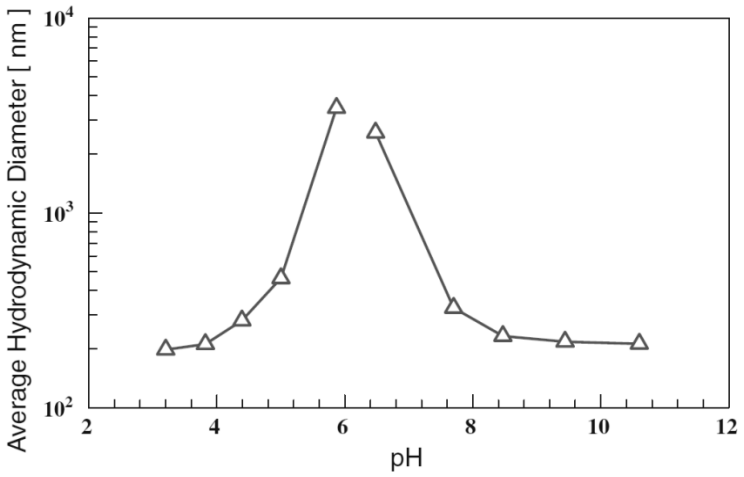

Figure 2.10 - The influence of pH on TiO_2 on the hydrodynamic diameter

(From [189])

Kuscer, D (2012) reported on the formulation of aqueous TiO_2 for inkjet printing applications [190]. Commercially available TiO_2 powders, with a primary particle size of 50 to 100 nm, were milled for 5 hours and adjusted to a pH of 11 to produce an average particle size of 190 nm. However as mentioned previously, inkjet manufacturers recommend that only fluids with a pH within the range of 4-9 are used to avoid the risk of corrosion and damage within the print head [128].

Metal oxide nanoparticles can be synthesized in several ways; however, most of the commercially available products are produced by gas-phase methods due to the high output capacity and low costs compared with the alternatives. Nanopowders produced by this method are often heavily aggregated and agglomeration is difficult to avoid [74]. Liquid-phase production is able to produce non-agglomerated particles by adding organic additives that are adsorbed onto the surface of the particles. Deagglomeration occurs through the break-up of bonds between nanoparticles and aggregates can be prevented with surface treatment methods (which will be covered in more detail later on). Mechanical methods such as milling have also been shown

to break-down agglomerates but can also result in the re-agglomeration of particles due to the impact between the particles and grinding media. This results in a broader particle size distribution and in practice milling is only efficient for particle sizes larger than 500 nm. The milling process is also most suited to 'soft' agglomerates and therefore is not suited to gas-phase-produced metal-oxide nanoparticles which contain hard agglomerates [41, 191]. Chemical approaches can be used alongside mechanical methods to dissolve the interparticle necks between nanoparticle aggregates.

Adding polymeric dispersants such as polyethleylenimine (PEI), polyvinyl alcohol(PVA) or polyacrylic acid (PLA) to TiO_2 suspensions has been found to significantly reduce sedimentation when present in a 1:2 weight ratio with metal oxide nanopowders [192]. The addition of polyethylene glycol (PEG) has found to suppress cracking during the calcinations of films [72]. The addition of PEG has also been found to increase the porosity of films, an important factor which leads to increased dye absorption and conversions efficiencies [193].The optimum dispersant concentration (ODC) is typically quantified as dispersant weight per unit particle weight. This depends on the surface area of the particles and the type of dispersant. A study by Peng, B., et al., (2007) looked at the effects of polymer dispersants on the dispersion stability of TiO_2 (Degussa P25) aqueous suspensions. They prepared a suspension of 1 g TiO_2 nanopowder with 100 mL of deionised (DI) water and found an optimal mass fraction of 3 % dispersant [194].

2.5.5 Substrates

Glass is a robust, temperature stable material that has been traditionally used as a substrate in solar photovoltaics. However, it is fragile, non-flexible, heavy and expensive. As a result, flexible alternatives are being intensively investigated.

Several glass manufacturers including Schott and Pilkington are developing ultra-thin glass for photovoltaics in thicknesses of between 25 and 100 μm [195, 196].

A wide range of substrates have been utilised for printed electronic applications including flexible plastics, metal foils and paper, typically with a thickness less than 50 μm [61]. For solar applications, at least one transparent electrode is required. Polyethylene naphthalate (PEN) is a commercially available as a biaxially oriented semi crystalline film, with an upper processing temperature of 180-220 ˚C [197]. Polyethylene terephthalate (PET) is also widely available with an upper processing temperature of about 150 ˚C. Both suffer with issues of shrinkage when heated. Fluorine polyesters and polyimides have high processing temperatures above 350˚C, with manufacturers such as DuPont reportedly manufacturing films capable of withstanding processing temperatures up to 500 °C [198].

Paper is a cellulose-based material emerging as a substrate for printed electronics due to its recyclability, biodegradability and low cost. Paper substrates show improved ink adhesion and reduced absorption meaning that high resolution prints can be achieved with significantly less ink and therefore reduced costs. Several manufacturers including Mitsubishi and Arjowiggins, have developed coated paper that has a smooth surface and is thermally stable beyond 250 °C. At these temperatures, these coated papers show little noticeable change in its physical characteristics. The use of cellulose-based substrates in the manufacture of photovoltaic (PV) devices is however limited due to its opacity.

2.6 Summary

The use of digital printing techniques such as inkjet has the potential to deposit a wide range of functional materials. The technique is currently used for the

production of single layer conductive materials. However, the ever-growing development of printable materials, presents the opportunity to combine printed layers into more complex devices. The formulation of inks is a complex process and although rough guidelines can be found in the literature the development of stable dispersions, careful control of fluid properties and interaction with underlying materials is still required to retain functionality.

Solar photovoltaics have been identified by several authors as one of many electrical devices which could potentially be printed from functional inks. DSSCs are very good at converting light into energy at low wavelengths (390-700 nm), making them an ideal power source for low light environments. This makes them an ideal power source option for portable and mobile electronic devices which are primarily used indoors or outdoors in diffuse light. They can be manufactured in a wide range of colours through the use of different dye sensitizing materials which makes them attractive option for integration into solar shading and windows. Digital printing techniques could be utilized to manufacture highly customisable DSSCs onto a wide range of substrates (both rigid and flexible) for this application. However, further research is needed to firstly develop the materials into inks which can be printed and then evaluate their performance once deposited and incorporated within a DSSC.

Following the preceding literature review a number of research opportunities have been identified. These opportunities centre on gaps in knowledge that are current barriers to the use of liquid printing processes for cost-effective and efficient DSSCs.

- Inkjet printing potentially offers a high degree of control over the deposition of TiO_2 nanoparticle suspensions. However, a thorough investigation into the formulation of TiO_2 inks and printing parameters is required to fully understand

whether the technique is suitable. Firstly, TiO_2 nanoparticles will be dispersed in a suitable solvent. The dispersion will then be modified (through the addition of further compatible components) into a form suitable for printing whilst retaining the photo catalytic properties required for use within a DSSC.

- One of the main attractions of DSSC technology are the minimal manufacturing requirements and low cost materials. Platinum has a high catalytic activity and high corrosion stability and therefore is the commonly used as the counter electrode in DSSCs. However, it is expensive and rare, therefore low-cost alternatives that exhibit good catalytic are required to fully realize the commercial scale-up of the technology. Carbon-based materials have been used as a counter-electrode to produce comparable efficiencies to platinum [109, 112]. Therefore, a carbon-based dispersion will be developed and produced into a form suitable for printing. Once printed, the films will then be characterised to determine their suitability for use as a counter electrode in DSSCs.
- Solid state hole conductors have been highlighted as an option to replace liquid electrolytes within traditional DSSCs to address the lifetime and stability issues arising from the corrosive nature of iodine/iodide-containing electrolytes. However, there is currently little research available on printable electrolytes [199]. Consequently, part of this project will investigate the potential for solid-state electrolytes within printable DSSCs.

The notable contributions of this work are to further develop the science behind inkjet-ready materials development, and to examine the potential and performance of such materials in fully-printed devices. The challenges associated with such a novel product as printed DSSCs require the development and optimization of specialized processes for materials preparation and handling. Furthermore, many of the

components used to construct DSSCs may also be used in the construction of other electronic devices, meaning that their development can contribute to markets beyond that of DSSCs.

Chapter 3

Experimental methods

Production of DSSCs using digital printing techniques requires the formulation, printing and functional testing of several inks. A typical DSSC consists of three key parts: a dye-sensitized metal-oxide photo anode, a hole transport material, and a highly catalytic counter electrode. Several more layers could potentially be added to optimise the device, however only the basic structure was considered necessary in this work to demonstrate the capabilities of the printing technique. Materials were selected based upon the best available materials used within DSSCs as described in section 2.2 and refined by developing those materials into a suitable form for printing.

3.1 Materials

3.1.1 Substrates

Inkjet-printing of ITO films for transparent conducting electrodes has been reported in the literature [24, 200]. There is also a significant body of work investigating the replacement of rare, brittle and expensive ITO with cheaper, more widely available materials. Therefore both of these research areas were considered outside the scope of this project.

Printing was mainly carried out onto commercially available FTO sputter coated glass substrates (TEC8, Pilkington with a sheet resistance of 8 Ω/sq, transmittance of 80 %, and glass thickness of 2.3 mm) [201]. Flexible substrates were also considered by printing onto plastic films. ITO coated PET (sheet resistance of 60 Ω/sq, transmittance of 79% and thickness of 25 μm) was purchased from Sigma-Aldrich

[202] and ITO coated PEN (sheet resistance of 15 Ω/sq, transmittance of 78% and thickness of 125 μm) was purchased from Peccell [203]. A sample of transparent polyimide film was also received from Kurt D. Roberts at Dupont for investigation of high temperature flexible substrates.

3.1.2 Metal oxide material

The nano-structured metal oxide layer within DSSCs plays a critical role in the overall performance of the cell and therefore was considered an important starting point to investigate whether digital printing techniques could be used in the manufacture of DSSCs. As previously discussed, several metal-oxide materials have been considered for efficient electron transfer within DSSCs. TiO_2 has been identified as one of the best available candidates and therefore will be the main focus in this thesis [69]. TiO_2 nanopowder (Degussa, Aeroxide P25) was purchased from Sigma Aldrich, which is mix of anatase and rutile crystal phases.

3.1.3 Dye sensitizer

Dyes from the ruthenium family have been found to be ideally suited for the sensitization of titanium dioxide in DSSC applications. One of the most efficient sensitizers in the literature is known as N719 (purchased from Solaronix) which effectively sensitizes wide band-gap oxide semiconductors, up to a wavelength of 750 nm. The TiO_2 electrode was soaked in a 0.5 mM solution of N719 dye in ethanol for 24 hours and then rinsed with ethanol, as described by Ito (2010) [204].

3.1.4 Hole transport material

As previously discussed, several hole transport materials have been investigated to facilitate the transport of charge between the metal-oxide coated electrode and the counter electrode. The most successful cells incorporate an iodine/triiodide liquid

electrolyte. Therefore in this work an iodide based low viscosity electrolyte with 50 mM of iodine/triiodide in acetonitrile was used to make the inkjet printed films into DSSCs. The thickness of the electrolyte does not have an effect on the conversion efficiency of the DSSC, therefore the thickness was kept constant in all devices by using a 60 µm spacer [89].

The use of conductive polymers as hole conductors to replace the liquid electrolyte in standard DSSCs was also investigated. A PEDOT:PSS solution (Orgacon IJ-1005) with a concentration of 0.8 wt% in H_2O (purchased from Sigma Aldrich). Dimethyl sulfoxide (DMSO) (purchased from Sigma Aldrich) was added to the ink in an effort to increase the conductivity [205].

3.1.5 Counter electrode

The role of the counter electrode is to collect electrons from the external circuit and to reduce triiodide to iodide in the electrolyte. It should have low resistance and high electro-catalytic activity. Platinum is still the most efficient and widely used counter electrode in DSSCs and therefore a number of cells were produced using a pre-coated FTO glass (7 Ω/sq) purchased from Solaronix, prepared by screen-printing using a Platisol transparent paste followed by heat treatment at 450 °C [206].

As previously discussed, platinum is a rare and expensive material which could be replaced in the move toward low-cost commercial production of DSSCs [106]. Carbon black was first used as a counter-electrode in 1996 and since then a power conversion efficiency of 9.1% has been achieved [109, 112]. A review of the photovoltaic performance of DSSCs incorporating different carbon-based counter electrodes in section 2.25 found that carbon black and porous carbon usually result in higher catalytic activity and efficiency than graphitic carbon materials (graphene and

graphite) [106]. Therefore, inkjet printable carbon black was investigated as an alternative to the pre-coated platinum coated glass purchased from Solaronix.

3.2 Manufacturing equipment

3.2.1 Piezoelectric inkjet printers

Inkjet printers are capable of printing at the speeds required for producing roll-to-roll electronic devices, with commercial speeds up to 244 metres per minute from 1200 dpi (dots per inch) as standard [207]. Smaller benchtop systems are more suited to the research and development of new inks and substrate materials, but the fundamental process is the same. The Fujifilm-Dimatix DMP2831 materials printer (shown in Figure 3.1) was used at Printed Electronics Ltd in Tamworth and in the Engineering department at the University of Warwick. It is a benchtop piezoelectric inkjet printer with 1.5 mL cartridges that can be filled up with custom inks. The print head moves above a vacuum platen and is capable of creating patterns of 200 mm by 300 mm onto substrates up to 25 mm with an adjustable height. The print head used in this work had sixteen 21.5 µm diameter nozzles which can deposit 10 picolitre (pL) droplet volumes. Nozzle to nozzle spacing is 254 microns, equivalent to 100 dpi in a single row. However, the print head can be rotated so that the smallest increment between drop centres can be 5 µm, which is equivalent to 5080 dpi. As previously discussed, the drop spacing can be optimised so that each is deposited to produce an even coating.

Figure 3.1 - Fujifilm-Dimatix DMP2831 desktop piezoelectric inkjet printer

The printer had several features which are beneficial for the development of functional inks:

- meniscus control to prevent ink from dripping
- high frequency "tickling" to prevent the nozzles from drying
- nozzle temperatures can be heated to 70 ºC to reduce the viscosity of inks
- the type and frequency of cleaning cycles can be adjusted
- the printing platen can be heated to 60 ºC to aid drying of the ink once deposited

One of the best features of this printer is that it has an in-built drop watcher camera to provide real-time imaging of drops ejected from the nozzles. This allows the user to easily access the quality of the droplets produced, so that print settings (e.g. nozzle voltages or print waveforms) can be changed to provide optimal results. The Fujifilm-Dimatix printer is therefore the ideal printer for ink development and was a useful tool for this project.

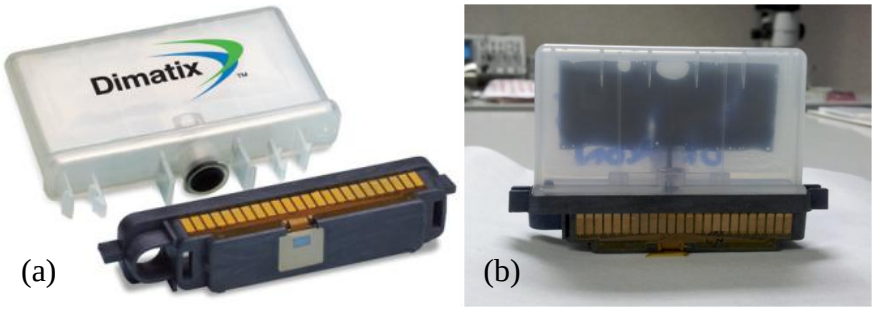

Figure 3.2 - Dimatix inkjet print cartridge (a) unloaded (b) loaded with ink

Inks are loaded directly into the cartridges using a syringe and then clicked into place in the printer. Fujifilm-Dimatix also produces a cartridge with 1 pL drop size which can deposit features as small as 20 µm. The 1 pL print head has a nozzle diameter of 9.0 µm, so any particle, polymer, or aggregate should be less than 90 nm as described in section 2.4.4. A 10 pL cartridge with a nozzle diameter of 21.5 µm was chosen for ink development, to reduce the likelihood of nozzle clogging from nanoparticles within the inks. The printer is operated through the Drop Manager software, which is user-friendly and easy to navigate.

A low cost printer was also purchased and used within WMG to demonstrate the use of the technology to provide economical manufacturing solution using a widely available piece of equipment found in most households. Epson and Kodak use pigments within their inks instead of dyes, therefore they are the most suited to the printing of nanoparticle dispersions for functional applications. The Epson stylus photo P50 desktop piezoelectric inkjet printer (shown in Figure 3.3) incorporates a "micro piezo" print head with 90 nozzles with an approximate diameter of 19.0 µm [208]. The print head technology is able to eject ink droplets of different sizes by

varying the electrical charge given to the piezoelectric elements. This enables the printers to produce droplets as small as 1.5 pl, resulting in high resolution printing.

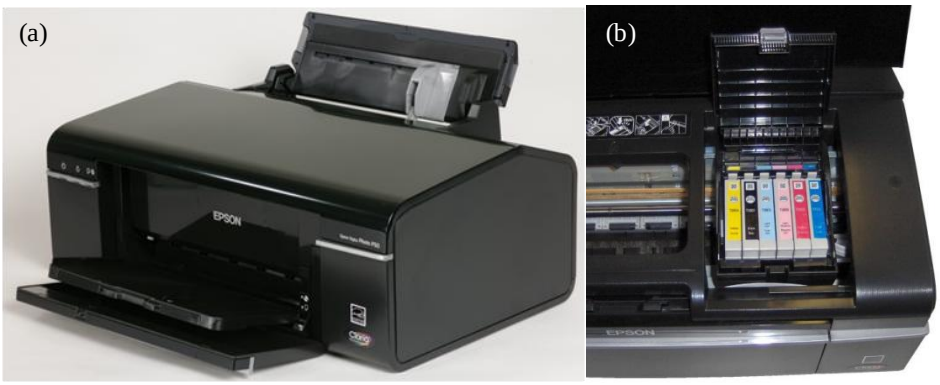

Figure 3.3 - (a) Epson stylus photo P50 printer (b) Location of ink cartridges

The printer is designed for use with flexible substrates up to A4 size (210 × 297 mm^2) which is loaded into the top of the printer. Refillable cartridges compatible with the printer were purchased so that functional ink formulations could be loaded and printed. Inks were filtered prior to printing to avoid nozzle blockages and loaded into the black cartridge.

3.2.2 Mechanical compression

The TiO_2 layer within DSSC is traditionally screen printed from a paste followed by sintering at temperatures of 450 ºC or above. This sintering step has several functions. Firstly, it burns off the organic binder material to create a porous material in which dye can penetrate the film and attach to the TiO_2 particles. Secondly, it fuses together some of the TiO_2 particles to promote the inter-particle connection within the material and lastly it improves the contact between TiO_2 and FTO coated substrate to provide strong adhesion and reduce the risk of delamination [31]. These adhesive and mechanical properties significantly affect the overall performance of the device.

Following inkjet printing onto polymer films, the samples were dried in a vacuum oven at 140 ºC for 30 minutes followed by cooling to room temperature. The films were then placed in between two polished aluminium sheets and loaded into a Collin 200 M laboratory platen press (shown in Figure 3.4). A study on the influence of heat treatment during compression has found that no relevant difference can be observed, therefore compression temperature was kept constant at 25 ºC [33]. The heating/cooling platens are controlled by a uniform temperature distribution over the platen surface (± 1°C). Heating/cooling rates up to 30 ºC /minutes are readily achieved. Optimal compression of TiO_2 films has previously been found at 30 MPa, however the press has a maximum pressure of 25 MPa and therefore films will be compressed at this pressure for 60 seconds [31].

Figure 3.4 - Collin 200 M laboratory platen press

3.3 Characterisation of fluid properties

3.3.1 Particle sizing

The distribution of particle sizes within prepared particle suspensions and printed films is an important part of this project for two main reasons. Firstly if the particles are too large, they cannot be printed and secondly once deposited, the particle size influences the performance in the application of DSSCs. There are a number of particle size measurement techniques applied. In choosing a suitable technique, consideration was given to the particle size range which could be measured and the measure of particle size returned. When considering the measurement of particles for use within inks, it was important to consider the final application and therefore samples were measured in the conditions which they were to be used e.g. suspended in the same solvent mixtures. In addition it is important to consider the number of measurements which must be taken to obtain statistically significant results. Table 3.1 outlines the techniques available in this project to measure particle size. Although these techniques are all capable of measuring other properties, they will now be discussed in relation to measurement of particle size.

Table 3.1 - Properties of particle sizing techniques

Technique	Typical size range measured	Size/property measured in this project
Optical Microscopy	0.8 - 150 µm	Any which can be taken from an image e.g. particle diameter
Scanning Electron Microscopy (SEM)	Wide range of sizes can be measured.	
Transmission Electron Microscopy (TEM)	Samples must be thin enough for electrons to pass through (>500 nm) [205]	
Dynamic Light Scattering (DLS)	0.3 nm - 10 µm	Hydrodynamic diameter and zeta potential
X-ray diffraction (XRD)	Generally applied to a powder specimen <10 µm	Crystallite size can be estimated by using the Scherrer equation

Optical microscopy was carried out on selected samples using a Carl Zeiss optical microscope with an AxioCamMRc5 camera. Image processing was carried out using the Zeiss AxioVision 4.2 software package. It had a maximum magnification of 100 times and has automated image stitching capability. For higher resolution images, Scanning Electron Microscopy (SEM) has been used. SEM is a valuable tool used to examine a wide variety of samples including powders and thin films where particle size, shape and distribution were readily observed.The SEM uses an electron beam to detect the properties of the sample including surface topography and material composition through penetration of electron beam onto the surface or near-surface of a specimen [209]. The technique generated images by capturing electron interactions, which produces images in atomic resolution [209]. The main

component of an SEM is the electron column which consists of an electron gun and two or more lenses to control the path of electrons travelling down an evacuated tube. The base of the column is taken up with vacuum pumps that produce a vacuum of 10^{-4} Pa; this prevents electrical discharge in the gun and allows the electrons to travel freely within the instrument. Electrons are generated in the cathode, and accelerated due to a voltage difference between the cathode and anode of 0.1 - 30 kiloelectron volt (keV) [210]. At high magnification, the technique was used to observe the size and distribution of particles in addition to any particle fusing formed from sintering at high temperatures or pressure. At lower magnifications the technique was used to check the film quality, formation of cracks or inhomogeneous areas within the printed films. During the analysis process, the brightness, contrast and image magnification were adjusted accordingly in order to obtain a good quality image of sample. A detailed understanding of the technique is not required for this project however, for more information on SEM, the reader is directed to the texts by Goodhew et al [211] and Reimer [212].

A Hitachi TM3030 benchtop SEM, with a magnification of up to times 60,000 and a gun voltage of 5 kV or 15 kV was used for selected samples. For samples that required further magnification a Carl Zeiss Sigma SEM was used, which has a magnification of up to times 100,000 to examine nano-scaled features.The samples were dried in a vacuum oven to remove any moisture then mounted onto a sample holder using carbon tape, they were then sputter coated with gold and to produce a conductive coating.

Dynamic light scattering (DLS) measures the size of particles dispersed in a liquid, typically in the sub-micron region. The particle size distribution is calculated by measuring the intensity of light scattered when a laser beam is passed through a

sample containing particulates. Figure 3.5 illustrates how large particles scatter light at small angles and small particles scatter light at large angles. The angle and intensity at which the light is scattered is then used to calculate the size of the particles within the solution. The calculation requires knowledge of the absorption and refractive index of the particles and reports particle sizes as a volume equivalent sphere diameter (referred to as the hydrodynamic diameter, D_h), assuming that they are spherical in shape [213].

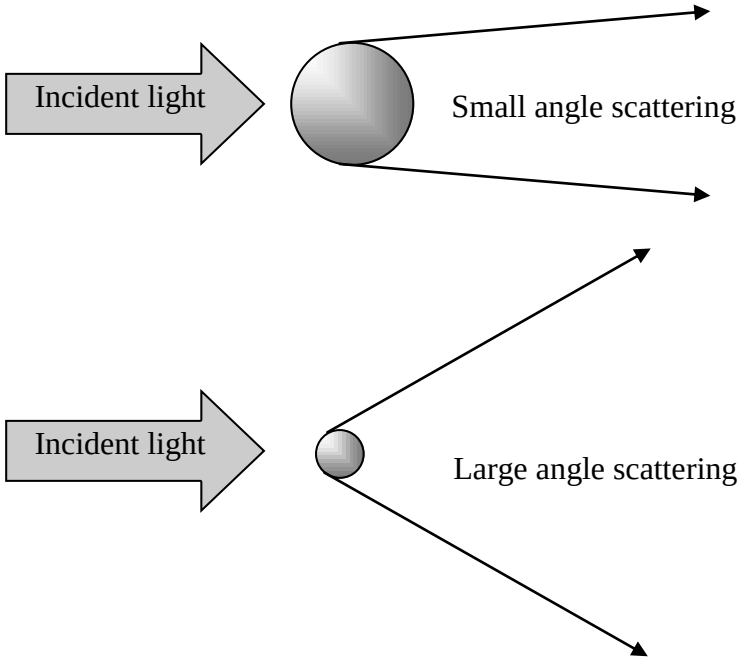

Figure 3.5 - Scattering of light from small and large particles

The presence of non-spherical particles or high particle loadings may result in an overestimation of the volume concentration (as shown in Figure 3.6). Good spatial separation of individual particles is required to gain an accurate measurement. If the sample is too concentrated, then light scattered by one particle will itself be scattered

by another (this is known as multiple scattering).The manufacturers suggest that (assuming a density of 1 g/cm^3) a maximum concentration of:

- 5% mass for particles between 10 nm and 100 nm
- 1% mass for particles between 100 nm and 6 µm

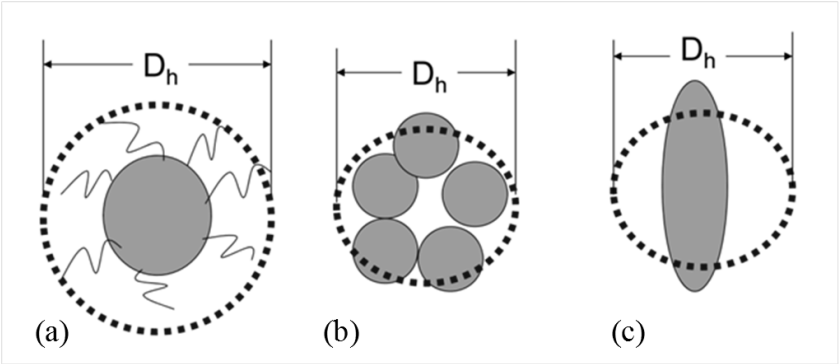

Figure 3.6 - Illustration of how hydrodynamic diameter (D_h) is influenced by (a) adsorbed polymer layer (b) formation of agglomerates and (c) particle shape

According to the equipment manufacturer, measurements are highly reproducible (within 2%) and most problems come from inconsistent sample preparation techniques. In this work, DLS was carried out using a Zetasizer Nano ZS particle size analyser from Malvern Instruments. It had a measurement range of 0.3 nm (+/-2%) to 10.0 µm (+/-2%) in diameter. To obtain statistically significant results, each sample was dispensed into a cuvette and allowed 120 seconds to stabilize, after which 3 measurements were taken from a minimum of 100 runs.

XRD diffraction patterns can be analysed to determine the crystallite size. A crystallite may be made up of several particles; however crystallite size often matches grain size. As the crystallite size gets smaller, the diffraction peak gets broader. X-ray diffraction (XRD) analysis of the TiO_2 was performed using an Empyrean diffractometer from PANalytical with a CoKα source of wavelength (λ)

1.7890 Angstroms (Å) and data was taken in the 2θ range of 20˚ to 95˚. The Scherrer equation [214] can be applied to estimate the crystallite size from the width of the diffraction peaks halfway between the background and the peak maximum (FWHM):

$$D = \frac{K\lambda}{(B.\cos\theta_B)}$$

Where:

- *K* (the Scherrer constant of proportionality) depends on the shape of the crystal. For spherical crystals with cubic symmetry, this is equal to 0.94.
- *D* is the characteristic crystal size (nm)
- λ is the wavelength of incident radiation (CoKα = 0.17890 nm)
- *B* is the angular width of the peak at half maximum height (radians)
- θ_B is the characteristic diffraction angle (radians)

3.3.2 Viscosity

Viscosity is a measurement of a fluids resistance to gradual deformation by shear stress or tensile stress [215]. Knowledge of a fluids characteristic under stress is valuable in predicting the performance in a printing process. In inkjet printing, for example, high viscosity fluids require more energy to move, resulting in the need for a higher input voltage to produce a drop from a piezoelectric inkjet system. The incorporation of nanomaterials within a solution will also influence the bulk properties of the mixture. For instance, altering the weight percent of nanoparticles will influence the rheological (flow/deformation) behaviour of the formulated product.

A Brookfield DV2T rotational viscometer was used in addition to a small sample adapter with a link hanging spindle (SC4-18) using a 6 mL sample size (illustrated in

Figure 3.7). The small sample adapter can measure viscosities in the range of 1.5 to 30,000 cP. The viscometer has a speed range from 0.1 to 200 rpm, however the rotational speed is limited by the viscosity of the sample. When combined with the SC4-18 spindle, this results in a maximum measureable shear rate of 264 s^{-1}. It has an accuracy of ± 1.0 % and repeatability of ± 0.2 %.

Figure 3.7 - Picture of small sample adapter for Brookfield rotational viscometer

A Kinexus rotational rheometer from Malvern Instruments was used to measure the viscosity and rheology of selected samples. The system works on a similar principle to the Brookfield viscometer in that it applies controlled shear deformation to a sample, to enable measurement of flow and dynamic properties of a material. However, conventional rheometry techniques such as these have limitations in their ability to access ultra-high shear rates, particularly for low viscosity liquids. As previously mentioned inkjet inks typically have viscosities in the range of 1 to 40 cP and therefore rotational viscometers are limited due to flow instability and viscous heating at high shear rates.

The inkjet printing process usually involves high jet speeds, typically more than 6 m/s. Considering that the ink flows through a channels approximately 60 µm in width, according to the equation below this can result in high shear rates up to

1×10^5 s^{-1} and therefore it is important to investigate how inkjet fluids perform under these conditions [216].

$$\text{Shear rate } (s^{-1}) = \frac{\text{Velcocity (m/s)}}{\text{Channel width (m)}}$$

In order to access high shear rate ranges for low viscosity liquids, a microfluidic viscometer (m-VROCi) from Malvern Instruments was used. For low viscosity samples, shear rates in excess of 1×10^6 s^{-1} are accessible with an accuracy of ±2% [217].

Figure 3.8 is an illustration of the microfluidic viscometer showing rectangular flow channel with embedded pressure sensors along its length. Viscosity measurements are made by loading the sample into a 1 mL syringe which is forced through the flow channel with a depth of 51.2 µm. Pressure measurements are taken via the sensors and a viscosity is calculated from the readings. The process enables stable flow and viscous heating is considered negligible within the flow channel.

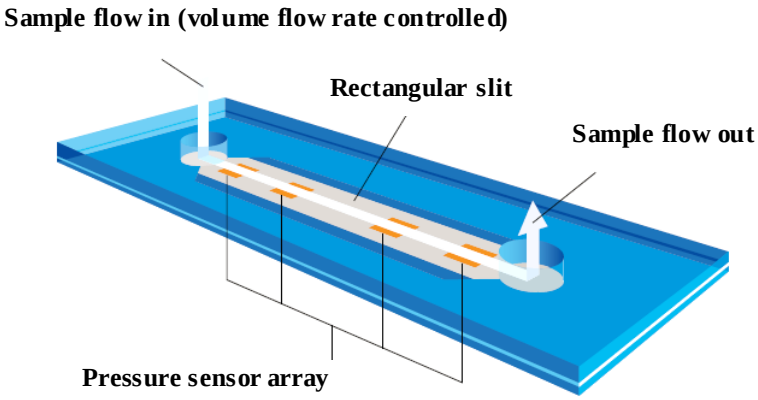

Figure 3.8 - Illustration of microfluidic viscometer.

(From [218])

3.3.3 Surface tension

Surface tension is a measurement of the cohesive energy present at the interface between liquid and air. Pendant drop analysis determines the surface tension of a liquid from the shape of the drop of that liquid hanging from a needle (illustrated in Figure 3.9). The surface tension of inks was determined using a Theta Lite optical tensiometer from Biolin Scientific which has an accuracy of 0.01 ±mN/m (shown in Figure 3.10). The surface tension at the liquid interface can be related to the drop shape through the following equation:

$$\gamma = \frac{\Delta\rho . G . R_0^2}{\beta}$$

where:

γ = surface tension (mN/m)

$\Delta\rho$ = difference in density between fluids at interface (kg/m^3)

G = gravitational constant (Nm^2/kg^2)

R_0 = radius of drop curvature at apex (m)

β = shape factor (dimensionless)

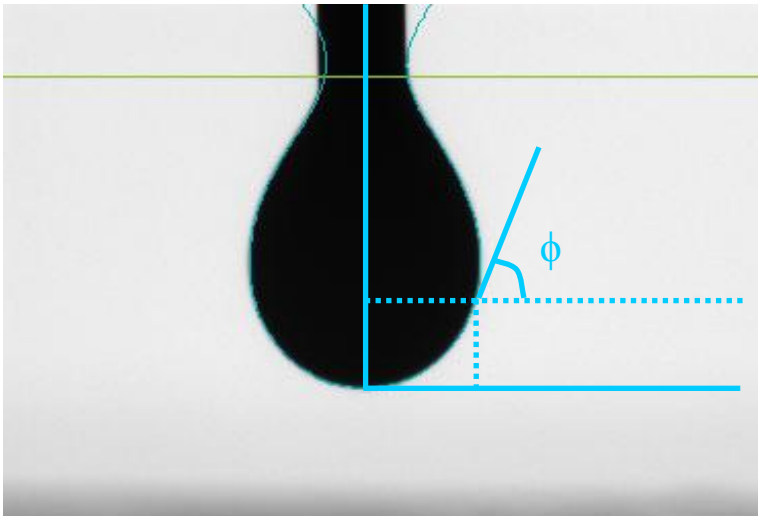

Figure 3.9 - Illustration of pendant drop analysis to measure surface tension

The shape factor can be defined through the Young-Laplace equation, which is solved using iterative approximations to provide a solution. Therefore, the surface tension can be calculated where the densities of the liquid and gas in contact are known. For custom ink formulations, the density of the main solvent was assumed. The droplet should have a suitable pendant shape to achieve reliable results; a droplet size from 5 to 20 µl is usually sufficient [219].

Figure 3.10 - Theta Lite optical tensiometer from Biolin Scientific

3.4 Characterisation of substrate properties

3.4.1 Surface energy

A particular issue is adhesion of the upper layers to the substrate. Adhesion occurs as a result of the attractive forces that exist between all atoms and which fall into three broad categories: primary (chemical); quasi-chemical (hydrogen bond); and secondary (van der Waals) [220]. For adhesion to occur, the surface energy of the substrate should not exceed the surface tension of the fluid by more than 10-

15 mN/m [221]. Adhesion occurs through three components: primary chemical bonding, secondary (or polar) bonding and mechanical bonding. However, the coating must come into intimate physical contact with the substrate before adhesion can occur. This interaction is referred to as ‘wetting’, which is an important factor in the adherence of two materials and occurs when the surface energy of the substrate is able to overcome the surface tension of a liquid. Surface energy is defined as the amount of energy required to create a new unit area of surface. Polar liquids such as water have high surface energies compared to non-polar liquids such as hexane. Surface energies can be calculated based on contact angle measurements [221]. In the coating industries, Table 3.2 outlines a simple method of determining whether a liquid has wetted a surface.

Table 3.2 - Determination of wetting by measuring contact angle

(From [222])

Contact angle	Liquid interaction with substrate
$\theta = 0$	the liquid completely wets the substrate
$\theta < 90^{\circ}$	high wetting occurs
$90^{\circ} \leq \theta < 180^{\circ}$	low wetting occurs
$\theta = 180^{\circ}$	the liquid does not wet the substrate at all

Many commonly used polymers often exhibit low surface free energy and consequently poor adhesive properties. This makes them difficult materials to wet and is one of the many challenges to consider in the pursuit for an alternative substrate to glass. The cleaning of substrates prior to coating or printing usually involves several steps to unsure uniform deposition. These steps are important to consider for the up scaling of any process, especially the consideration of any

materials which may require extra health and safety precautions to prevent harm to workers or the environment. Cleaning procedures differ between laboratories however the basic procedure usually starts with sonication in a detergent solution, sonication in an organic solvent such as ethanol or isopropanol, followed by rinsing with deionized water and finally dried with compressed nitrogen. Some suggest starting with sonication in a dilute acid to remove oxide impurities and others also use ultraviolet ozone cleaning to reduce the surface contamination. Other methods to modify a surface and promote adhesion include corona treatment treatment [114], plasma treatment [223] and chemical etching [224]. However, each would add cost and time to the manufacturing process.

The surface energy of substrate materials was also determined using a Theta Lite optical tensiometer from Biolin Scientific, which can measure contact angle with an accuracy of ±0.1˚. The surface energy of the substrates was calculated according to the European Standard EN 828 [219] for determining the wettability of a solid surface by measuring the contact angle and surface free energy. Drops of three different liquids (water, ethylene glycol and diiodomethane) were dispensed onto a plane test piece surface. For each drop, the left and right contact angles were measured. From the averaged contact angles of each liquid combined with its surface tension, the surface free energy of the substrate can be calculated. The OneAttension software uses the Fowkes method [216] to calculate the total surface energy (γ) from the sum of the contributions from dispersive interactions (γd) and non-dispersive interactions (γp).

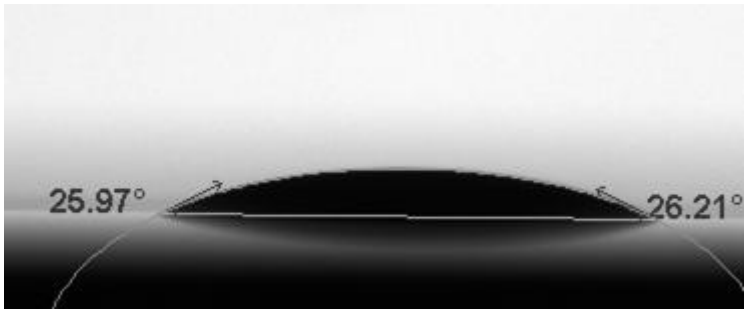

Figure 3.11 - Illustration of measuring contact angle

The different surface energies of each substrate material mean that droplets dry in different ways. If the surface energy of the substrate is too low, de-wetting will occur and the coating will not be homogeneously distributed over the whole surface. If the surface energy is too high then spreading will occur, resulting in poor resolution. As previously discussed, wetting occurs when the surface energy of the substrate is able to overcome the surface tension of a liquid. If the contact angle of a liquid onto a substrate is between 0 and 90˚, it is considered that high wetting occurs [222].

3.4.2 Thermal analysis

Thermogravimetric Analysis (TGA) was performed on plastic substrates and selected components within the ink to measure the thermal stability of the materials. TGA consists of a sample pan that is supported by a precision balance located within a furnace, where nitrogen is used to control the environment. As the sample is heated (or cooled), the mass is monitored. The instrument can quantify loss of components such as water, solvent or binder material due to thermal decomposition. It can also quantify the amount of solid components remaining. The Mettler Toledo TGA2 (STARe System) used in this study could provide heating up to 1100 ºC with a weighing accuracy of 0.005 %. A heating rate of 20 ºC per minute from a temperature of 25 ºC up to 600 ºC for all samples, with a sample size of between

2 mg and 50 mg. The TGA data was used to explain how the different components within an ink decompose in relation to temperature.

Differential scanning calorimetry (DSC) measures the heat flow change of a sample (compared with a reference) due to changes in their physical and chemical properties, where nitrogen is used to control the environment. Differences in heat flow arise when a sample absorbs (exo) or releases (endo) heat due to thermal effects such as melting, crystallization and chemical reactions. DSC was used alongside TGA to provide further results for interpretation of glass transition temperature (T_g), melt transition temperature (T_m) and degradation temperature (T_d) of plastic substrates. The glass transition temperature occurs when the bulk material ceases to be brittle and glassy and becomes more rubbery. The melting temperature defines the upper limit of stability. Investigating the thermal properties of plastic films provides important information to predict how they will behave during processing. The Mettler Toledo DSC3 (STARe System) used in this study can provide heating up to 700 °C measuring heat flow with an error of ± 200 mW. A heating and cooling rate of 25 °C per minute from a temperature of 25 ºC up to 600 ºC was used for all samples. Standard 40 µl aluminium crucibles will be used for both TGA and DSC measurements.

3.5 Characterisation of printed films

3.5.1 Crystal phases

X-rays are electromagnetic radiation of wavelength about 1 Angstrom (about the same size as an atom). X-ray diffraction (XRD) analysis is based upon Bragg's Law, which is a relationship developed to describe why crystal faces appear to reflect X-ray beams at certain angles of incidence.

$$n\lambda = 2dsin\theta$$

Where:

- θ is the scattering angle
- n is a positive integer
- λ is the wavelength of incident wave
- d is the interplanar distance

When a beam of X-rays is directed onto a material, the resultant diffraction of X-rays produce a pattern. The diffraction pattern can be analysed to provide information about the material, such as crystal phase, particle size and texture.

As previously discussed in section 2.2.2, TiO_2 has three main crystal phases, anatase, rutile and brookite. Each of the three phases have different band gap and photocatalytic energy. Carbon black is also available in different grades, each of which have certain characteristics. Each grade of carbon black may have different purities, porosities and carbon content which will affect their use as a conductive material. XRD analysis can determine the crystal composition of materials by measuring diffraction peak positions and intensities. The measured pattern can then be compared to entries within a reference database to identify the crystal phase. This is also known as qualitative phase analysis. Analysis was performed using an Empyrean diffractometer from PANalytical Empyrean with a cobalt source which has a CoKα wavelength (λ) of 1.7890 Angstroms (Å).

3.5.2 Thickness and surface quality

As previously discussed, the thickness and morphology of the metal oxide layer within a DSSC can influence the amount of dye that can be adsorbed. The thickness of conductive materials such as carbon and PEDOT:PSS also has an influence on the

properties. Therefore the thickness of the printed layer after thermal treatment was an important parameter to measure. Initially, a stylus surface profiler (Ambios XP-100) was used to measure roughness and step height of the printed layer within a precision of 1 nm. The 5 µm stylus has a vertical range to 400 µm and a maximum scan length 10 mm.

In order to better quantify and understand the overall surface topographies a 3D optical microscope (Bruker ContourGT) was used. It has a maximum scan length of 10 mm and a vertical resolution of 0.01 nm. It is fitted with an additional Nano Lens atomic force microscope (AFM) module with 1000 times magnification to enable imaging of nanometer-scale features. It is capable of measuring steeply sloped objects which regular optical microscope would struggle to see. It has a maximum scan length of 70 µm and a vertical resolution of 0.34 nm. Automated stitching within the Vision64 analysis software can be enabled to produce larger area scans of up to 150 mm^2. Three-dimensional (3D) surface measurement parameters can be used to measure roughness and height of printed features.

3.5.3 Transmittance

The total transmittance, clarity and transmission haze of the printed PEDOT: PSS conductive films was measured using a haze meter (BYK-Gardner haze-gard plus). Total transmittance is the ratio of total transmitted light to incident light. It is reduced by reflectance and absorbance. Haze is also known as diffuse transmittance where the light is reflected due to wide angle scattering. Clarity, on the other hand, is due to narrow angle scattering which may cause the image to appear blurred when the distance between the sample and the beam is increased. Figure 3.12 shows the measurement principle of the haze meter. A beam of light passes through the specimen and enters an integrating sphere. The sphere's interior surface is coated

uniformly with a matte white material to allow diffusion. A detector in the sphere measures total transmittance (direct transmittance plus diffuse transmittance) and transmission haze. A ring sensor mounted at the exit port of the sphere detects narrow angle scattered light (clarity) [225]. Before any measurement was taken, the equipment was calibrated to ensure that an accurate result could be obtained.

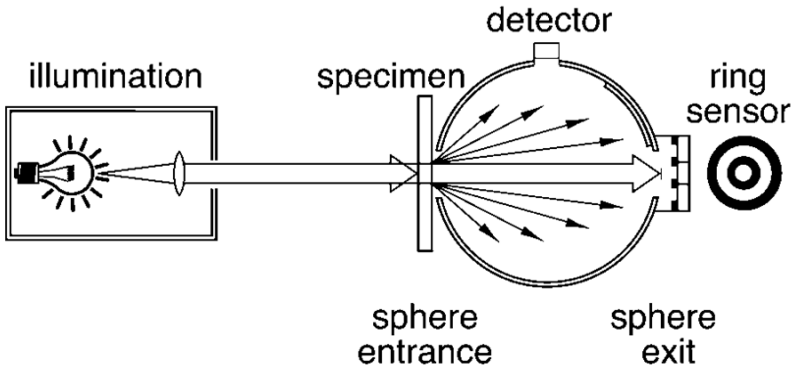

Figure 3.12 - Measurement principle of the haze meter.

(From [225])

Transparent TiO_2 electrodes have the potential to be used in applications such as windows and solar shades to harness energy while allowing some light to pass through [226]. However, the level of transparency has a direct impact on the resultant conversion efficiency of the cells. When the TiO_2 thickness increases, light transmission decreases and the efficiency rises [227]. To measure the transmittance of light over a wider wavelength (200-1100 nm), a Cary60 ultraviolet-visible (UV-Vis) spectroscope from Agilent Technologies was used. The spectroscope measures direct transmittance as a percentage (%T); this represents the percentage of the incident beam of light transmitted by the sample. A beam of light is separated into its component wavelengths through a diffraction grating or a prism. Each single

wavelength beam is split into two, with one beam passing through the sample to the sample detector and the other internal beam hitting a reference detector. The intensity of the reference beam (which should have little or no light absorption) is then compared to the sample beam.

3.5.4 Conductivity

Bulk resistivity, also referred to as volume resistivity, is the inherent resistance of a given material regardless of the shape or size. The resistivity of conductive materials is most often determined using a four point probe technique. With this method, four equally spaced probes are put in contact with the material, the two outer probes are used as a current source and the two outer probes measure the voltage drop across the surface of the material (shown in Figure 3.13). This method eliminates measurement errors due to the probe resistance, the spreading resistance under each probe and the contact resistance between each metal probe.

Resistivity is calculated using the following equation:

$$\rho = \frac{\pi}{ln2} \times \frac{V}{I} \times t \times k$$

Where:

ρ = Resistivity (Ωm)

V = Voltage (V)

I = Current (A)

t = Sample thickness (m)

k = is a correction factor (based on the ratio of probe spacing to sample diameter and on the sample thickness to probe spacing)

However, if the probe is centred on a very wide (sample diameter>probe spacing) and very thin sample (sample thickness<probe spacing), then the correction required can be considered negligible and the equation can be simplified. A Jandel cylindrical probe with 4 linear probes spaced 0.5 mm apart was used to measure the resistivity of the inkjet printed carbon samples [228].

Electrical conductivity (measured in S/m) is simply the inverse of resistivity and is a measure of the materials ability to conduct an electric current. Sheet resistance (measured in Ω/square) is a value used when measuring a thin layer of semi-conductive material and will change depending on the sample thickness.

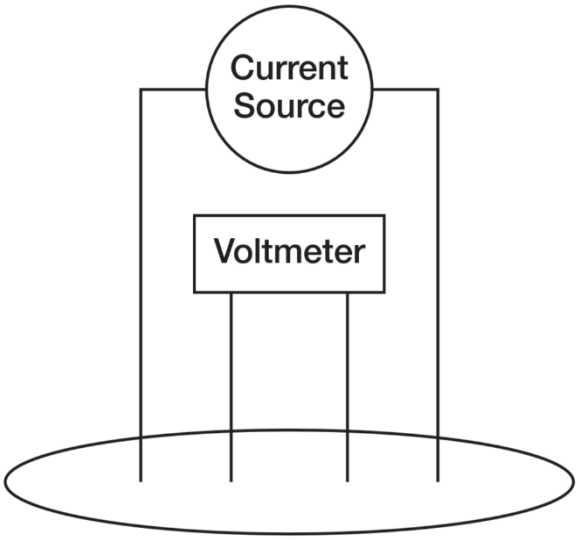

Figure 3.13 - Four-point probe resistivity configuration

Due to the low conductivity of the inkjet printed PEDOT:PSS, the four point probe method proved unsuitable and therefore a 2-point method was used. A multimeter was connected to either end of the conductive area to measure the average resistance across the entire width of the film. Measurement across the sample yielded bulk resistance (R). This value is independent of sample geometry. Therefore, the

conductivity (σ) was calculated as a meaningful figure for comparison. Resistance is related to conductivity by the following expressions [229]:

$$\rho = \frac{RA}{L} \qquad \text{and} \qquad \sigma = \frac{1}{\rho}$$

Where:

ρ = Resistivity (Ωm)

R = Resistance (Ω)

A = Cross sectional area (m^2)

L = Length (m)

σ = Conductivity (S/m)

The equations show that conductivity is the inverse of resistivity; therefore as one variable is increased the other variable is decreased.

3.6 Device characterisation

PV devices should be characterised directly after fabrication to minimize the effect of degradation caused by water and oxygen in the air [230]. There are five electrical performance parameters that are used to characterize and compare solar cells [231]. Three parameters are derived from the current-voltage (IV) curve, as shown in Figure 3.14.

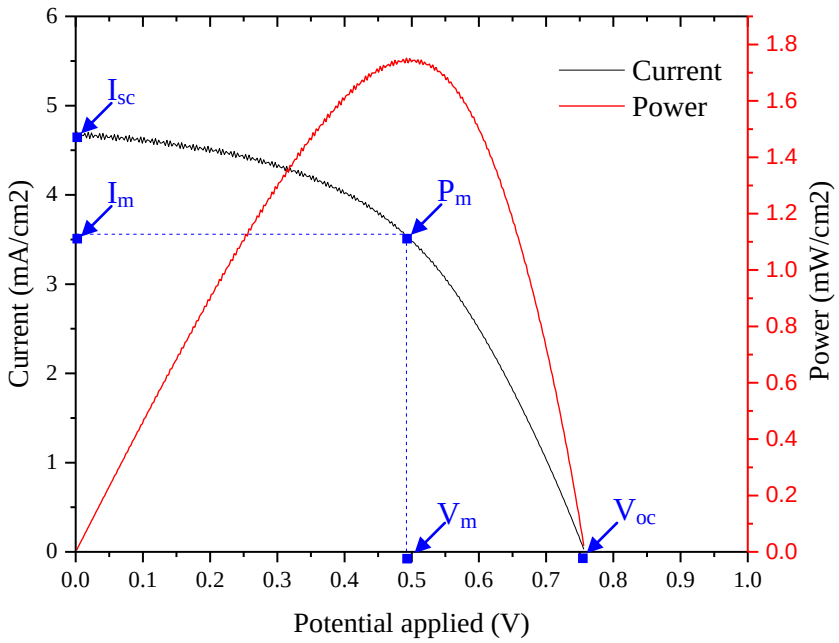

Figure 3.14 - I-V diagram for an illuminated inorganic solar cell

1. Short-circuit current (I_{sc}) – This is the current that flows through an illuminated solar cell when there is no external resistance. It is measured at the intercept where the curve crosses the current axes. For an organic device the Short-Circuit Current (I_{sc}) is negative and therefore the curve is inverted [232]. In the dark, there is no voltage or current flow therefore the IV curve passes through the origin. When the cell is exposed to light, voltage and current is generated, causing the I-V curve to shift downwards.
2. Open circuit voltage (V_{oc}) – This is the maximum voltage across a photovoltaic cell e.g. when light is on the cell but no current is flowing. It is measured at the intercept where the curve crosses the voltage axes.
3. Maximum power point (P_m) - the "knee" point where the product of voltage (V_m) and current (I_m) is maximum cross on the power curve.

4. The values of I_{sc}, V_{oc} and P_m can then be used to determine the Fill Factor (FF) and power conversion efficiency (η).
5. Fill factor (FF) – The ratio of the cell's actual maximum power output to the product of the open circuit voltage and short circuit current [233]. This is a key parameter in evaluating the performance of solar cells. A high FF means low electrochemical losses, whereas a low FF indicates there is room for improvement. Several factors are known to influence the FF including the quality and interface of layers within the cell. DSSCs incorporating an iodide/triiodide redox couple with record efficiencies report fill factors of 0.71 [47].The fill factor is illustrated in Figure 3.14 as the red area divided by the blue area.

$$FF = \frac{V_m \times I_m}{V_{oc} \times I_{sc}}$$

6. Power conversion efficiency (η) can be calculated from the equation below. To increase the efficiency of solar cells, one of these 3 factors (Isc, Voc, and FF) needs to be improved.

$$\eta = I_{sc} \times V_{oc} \times FF$$

All of these parameters need to be determined under standard test conditions (STC), as defined by the National ASTM standard E948 and IEC standard 60904-1 [47] i.e. the temperature of the device is to be 25 ˚C ± 1 ˚C, spectral irradiance distribution of the light is to be AM1.5 ± 25 %, total irradiance measured (E_m) at the solar cell is to be 1000 W/m^2 ± 2 % [47]. A solar simulator from Wacom electric company limited was used which consists of a 500 W xenon lamp and 150 W halogen lamp to match the artificial light closer to the natural solar spectrum than a one lamp system. The

resultant spectral irradiance distribution of the simulator matches the air mass (AM) 1.5 standard within ± 10% as shown in Figure 3.15.

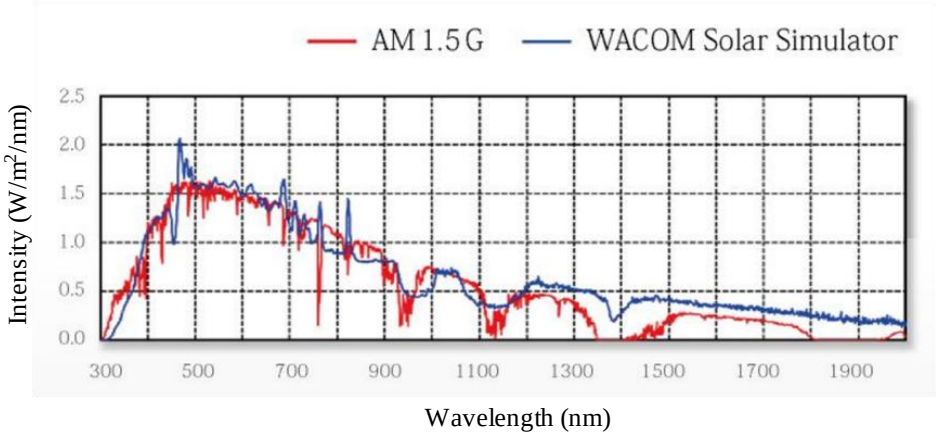

Figure 3.15 - Spectral irradiance distribution of the solar simulator.

(From [234])

Chapter 4

Development of an aqueous titanium dioxide ink to produce inkjet printed photo anodes in DSSCs

4.1 Introduction

This chapter starts by describing the development of a TiO_2 aqueous dispersion. It continues by detailing how the dispersion is optimised through ultrasonic processing, modification of pH and the addition of dispersants to reduce the size of the agglomerates and aid stability within the suspensions. A description of the printing trials and optimisation of the print parameters to enable uniform deposition of the ink is given. Once printed, the TiO_2 films were then characterised to determine the crystal phase, particle size, thickness, surface distribution and transmittance. In order to overcome the issues of surface cracks and peeling of the coating from the substrate, an investigation was performed on the use of compression and the incorporation of binder materials within the TiO_2 ink.

Finally, the chapter ends with a description of how the printed films were incorporated within DSSCs to evaluate their electrical performance and therefore determine the commercial potential of inkjet printing as a manufacturing technique. A standard cell was produced as a benchmark using a TiO_2 photoelectrodes prepared by doctor-blading. Four key electrical performance parameters (Isc, Voc, FF and efficiency) were used to characterize and compare the cells.

4.2 Identification of crystal phases

A study by Suttiponparnit et al. reported on the role of particle surface area, primary particle size and crystal phase on the dispersion properties of TiO_2 nanoparticles [185]. Degussa Aeroxide P25 TiO_2 is manufactured on a large scale according to the aerosil process. It is used widely because of its relatively high levels of photo catalytic activity and commercial availability. A review of the literature finds that various particle sizes and phase compositions have been reported indicating considerable inhomogeneity, both within and between production batches [235]. The nanomaterial will be the functional component within the ink and resultant printed layer. Therefore to understand fully the as-delivered material, the AeroxideTiO_2 P25 material used within this work was analysed to determine the phase composition. X-ray diffraction (XRD) analysis of the TiO_2 was performed using an Empyrean diffractometer from PANalytical with a CoKα source of wavelength (λ) 1.7890 Angstroms (Å) and data was taken in the 2θ range of 20˚ to 95˚. Identification of crystalline phases for the P25 nanoparticles was achieved by comparison of their XRD patterns (shown in Figure 4.1) with those in the Joint Committee on Powder Diffraction Standards (JCPDS) database. Based on the XRD data, the distribution of anatase and rutile was calculated using the following equation [236].

$$W_R = \frac{I_R}{I_0} = \frac{I_R}{(0.88I_A + I_R)}$$

W_R is the rutile weight percentage, I_A and I_R are the integrated diffraction peak intensities of anatase and rutile. I_0 is the total integrated intensity of the anatase (101) and rutile (110) peaks. The XRD spectrum has strong diffraction peaks at 29.57˚ which indicates TiO_2 in the anatase phase [237]. Analysis determined that the phase composition is a mixture of anatase (71 %) and rutile (29 %).

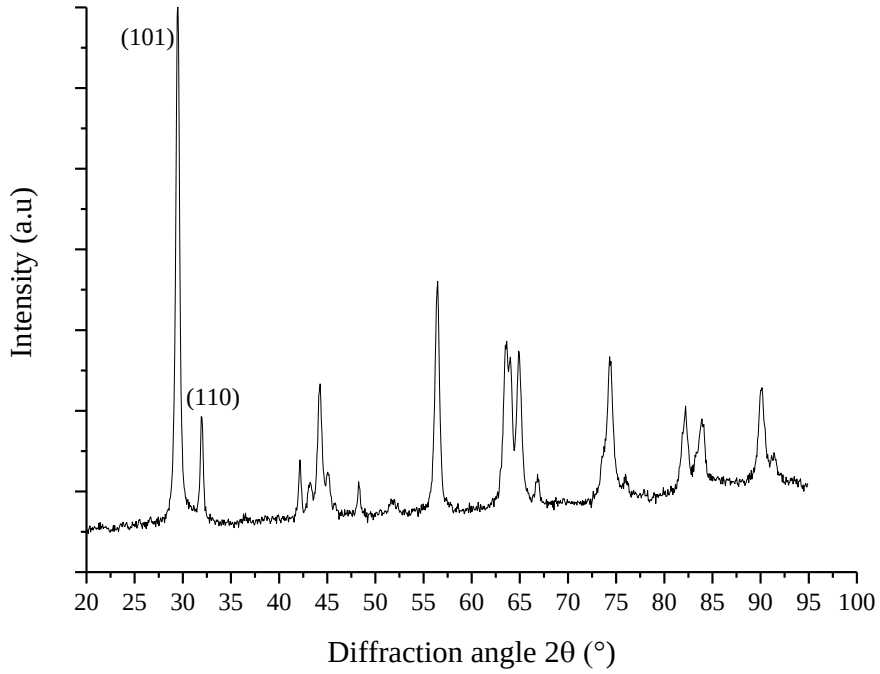

Figure 4.1 - XRD spectra of P25 TiO_2 powder from Degussa. Anatase 101 and rutile 110 are shown.

4.3 Analysis of particle size

The crystallite size can be estimated from measured XRD peak half breadths by using the Scherrer equation introduced in 3.3.1. The characteristic diffraction angle (from a cobalt source) was taken to be 29.6° for TiO_2 anatase which agrees with the data above [236]. The angular width of the peak at half maximum height was measured from the XRD spectra (shown in Figure 4.1) and subsequently the crystal size was calculated to be 23 nm. However, a crystallite may be made up of several particles and therefore further analysis of particle size was undertaken.

Particle size and shape in powders can be readily observed using electron microscopy. SEM was performed on the starting powder, Figure 4.2 shows that the particle size of the powder (as received) ranges significantly with small primary

particles and larger agglomerates and aggregates (>5 µm) which have formed over time.

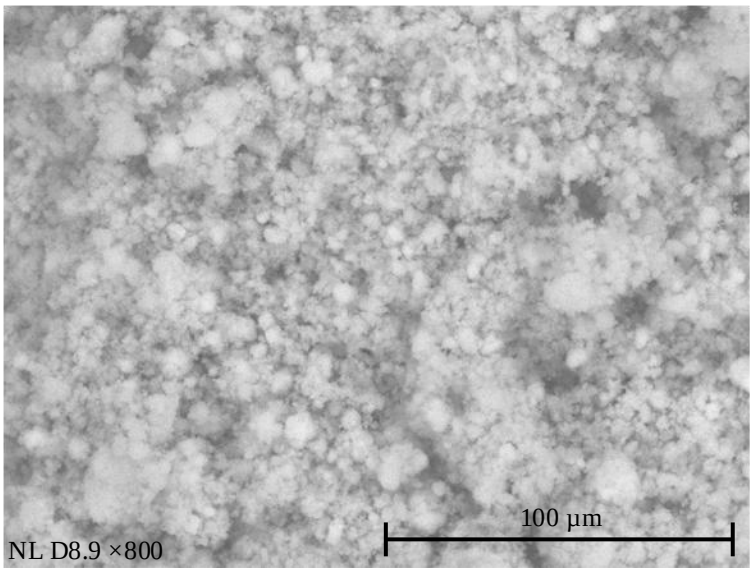

Figure 4.2 - SEM of P25 TiO_2 powder

The average diameter size of the nanoparticle dispersions were characterized using the Zetasizer Nano ZS (Malvern Instruments, United Kingdom), utilizing dynamic light scattering (DLS).The manufacturers suggest a maximum concentration of 5% mass for particles between 10 nm and 100 nm (assuming a density of 1 g/cm^3). According to the supplier, titanium dioxide (Degussa Aeroxide P25) has a density of 4.26 g/cm^3, therefore further dilution was required to produce an accurate representation.

As previously discussed, the carrier solvent is usually the largest constituent within an inkjet ink and therefore has a huge impact on the overall properties of the ink. The choice of solvent will also impact the odour, ventilation requirements, waste management procedure and cost of the manufacturing process. Several solvents were trialled during this project including water, isopropanol, ethanol, methanol and dimethylformamide (DMF). Good dispersions were achieved in all; however work

focussed on water as the main solvent to provide a low cost ink with low environmental impact. This is one of the most challenging as it has a high surface tension of approximately 72.80 mN/m. The surface tension of the ink should be matched to the specific printer and must be high enough to hold the ink in the nozzle without dropping. Therefore it was noted that the use of a co-solvent or surfactant would be required to reduce the surface tension of the ink to be compatible with the fluid restrictions of the printer.

As previously discussed inkjet inks typically contain solid fractions of approximately 10 wt%, however following extensive trials, it was found that high loading resulted in significant sedimentation therefore a 1 wt% solution of TiO_2 nanoparticles in DI water was prepared. Approximately 1mL of the nanoparticle dispersion was dispensed into a polystyrene cuvette. Each sample was allowed 120 seconds to stabilize, after which 3 measurements were taken from a minimum of 100 runs. From Figure 4.3 it can be seen that the particle size distribution of the TiO_2 nanoparticle suspension prepared, shows a bimodal curve indicating that the nanoparticles agglomerate in two size ranges of approximately 531 - 3091 nm and 4145 - 6439 nm.

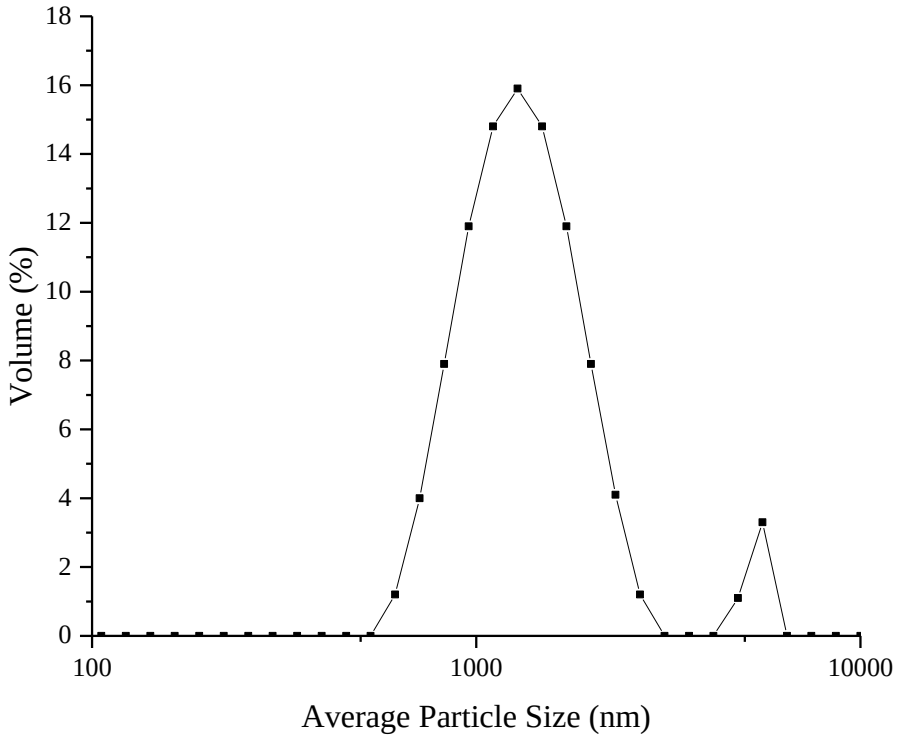

Figure 4.3 - Particle size distribution of aqueous TiO_2 solution

The particle size distribution measured by DLS differs significantly to the crystal size calculated using the Scherrer equation. It must be noted that the size determined by diffraction methods corresponds to the areas of the crystal regions where the atoms are perfect and continuous i.e. primary particles. The size obtained by diffraction cannot always be simply compared to the sizes determined by other techniques. DLS represents the measurement from in-situ conditions of TiO_2 nanoparticles within an aqueous dispersion, and clearly shows the formation of agglomerates formed from many small crystals due to sample preparation. The larger sizes are attributed to agglomerates, since the technique is unable to distinguish between the two.

As previously mentioned, particles within the inks should be smaller than 215 nm to prevent nozzle clogging. Therefore several methods were investigated to reduce the agglomerates found within aqueous dispersion of TiO_2, as detailed in the following sections.

4.3.1 Influence of ultrasonic processing

As previously discussed in section 2.4.4, the energy of simply stirring particles into water or binder is not great enough to overcome the particle attractive forces preventing the breakup of agglomerates. Ultrasonication produces shock waves caused by collapsing cavitations, this causes particles to collide and any agglomerated particles are eroded and split apart. Ultrasonic processing can be carried out using a probe-type ultrasonic homogenizer or an ultrasonic bath. In an ultrasonic bath, the sonication effect is of low intensity and unevenly spread resulting in uncontrollable distribution of cavitation throughout the tank. The repeatability and scalability of the process is very poor. In contrast, the probe-type ultrasonic devices have a high localized intensity and therefore, greater localized cavitation effect.

The use of ultrasonic processing was investigated as a method to break up agglomerates within the solution. However, it can cause a temperature increase which may result in degradation and reduced quality of the dispersion. The sedimentation of TiO_2 particles has been observed at temperatures above 45 ˚C [238]. Therefore the temperature of the suspensions was monitored during ultrasonic processing to ensure that they did not exceed this. The temperature was monitored in relation to time, whilst the TiO_2 dispersion was processed in an ultrasonic bath (Elmasonic) and ultrasonic probe (Hielscher UP200S, 200 watts, 24 kHz).

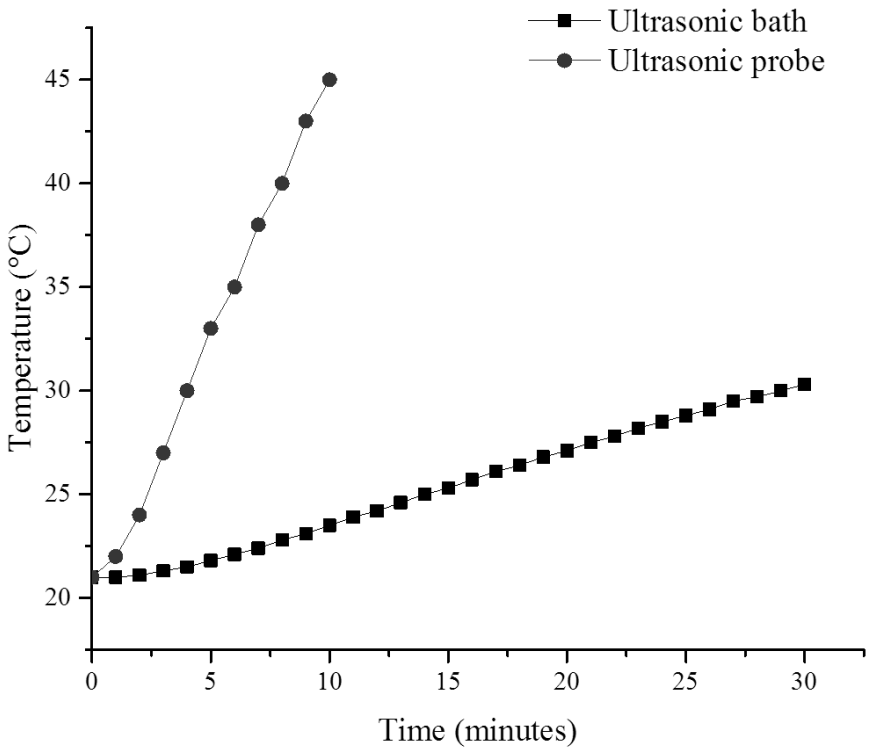

Figure 4.4 - Measured temperature over time during ultrasonic processing

Figure 4.4 shows that after 30 minutes of processing in an ultrasonic bath, the temperature increased from 21˚C to 30 ˚C. In contrast, the temperature increased more rapidly with the use of an ultrasonic probe and reached 45˚C after 10 minutes at 60% amplitude. Processing with an ultrasonic probe was therefore limited to 10 minutes to prevent degradation to the material.

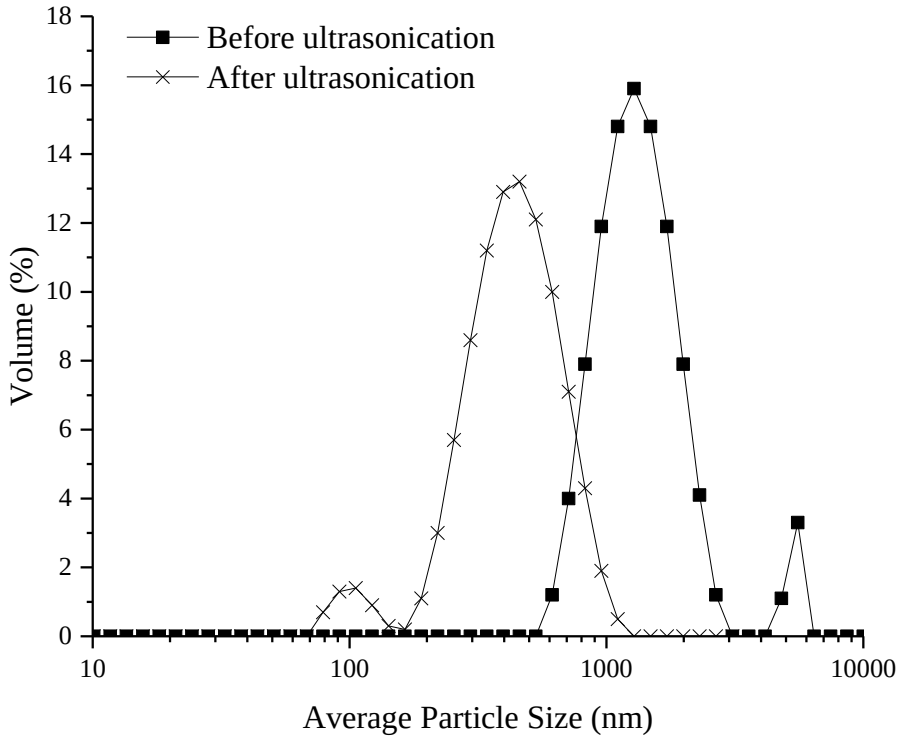

Figure 4.5 - Influence of ultrasonic processing on particle size distribution in aqueous TiO_2 suspension

Figure 4.5 shows the average particle size distribution by DLS after the suspensions were ultrasonicated with a probe for 10 minutes at 60% amplitude. After ultrasonic treatment, the particle size distribution curve still appeared as a bimodal shape; however the most dominant curve was shifted to the left indicating that the average agglomerate size was decreased. After ultrasonic treatment, the volume of the most dominant curve was also decreased, indicating further breakdown of agglomerates. This suggests that the break-up process was a result of a rupture mechanism.

4.3.2 Influence of pH

As previously discussed, the long-term stability of particle-based inks can be improved through electrostatic treatment. Electrostatic treatment is when charges are

generated on the surface of particles to prevent or control re-agglomeration. One of the simplest ways to adjust the surface charge of particles is to modify the pH of the solution. As the pH of a suspension is shifted away from neutral then the particles tend to acquire more charge, resulting in a more stable dispersion.

To investigate the relationship between pH and particle size, hydrochloric acid (HCl) and sodium hydroxide (NaOH) was used to prepare solutions with pH values between 2 and 12. TiO_2 nanoparticles were then added to the solutions to produce a concentration of 1 wt% and stirred for 2 hours using a magnetic stirrer. The particle sizes were then measured using DLS.

Firstly the pH of TiO_2 in water (with an average particle size of 380 nm) was measured using a pH meter from Hannah instruments. The pH of DI water was measured to be 6.59 and the TiO_2 dispersion was 5.68. This result is in agreement with the literature which suggests that when TiO_2 nanoparticles are dispersed in water extra hydrogen ions are produced resulting in a decrease in solution pH [189].

Figure 4.6 shows that as the solution pH was made more acidic, a reduction in particle diameter was observed and similarly, a reduction in the average particle diameter was observed as the solution pH was more alkaline.

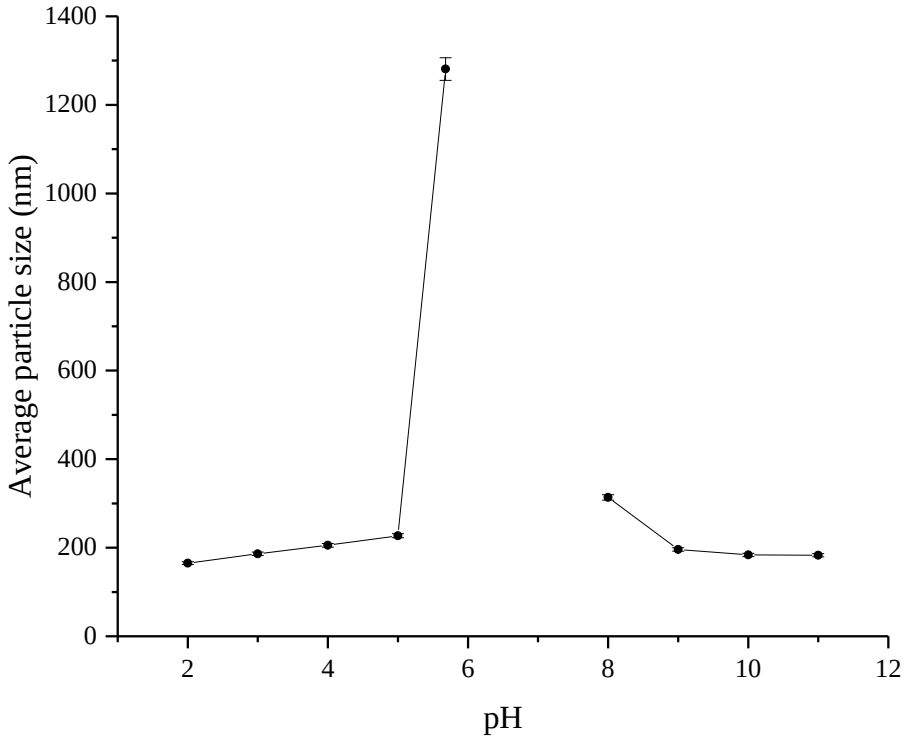

Figure 4.6 - Influence of pH on TiO_2 particle size in aqueous solutions

Although, the results indicate that altering the pH results in a reduction in particle size, a significant amount of sedimentation was observed in samples which were left over a few weeks. To improve the stability of the inks, steric treatment was considered through the use of polymeric dispersant which adsorb onto the surface of the particles to provide a barrier against the formation of agglomerates. The results of this investigation will be detailed in the next section.

4.3.3 Influence of polymeric dispersants

Dispersing agents are designed to stabilize the dispersed particles against flocculation. It is particularly important to ensure that enough dispersant is added to overcome the attractive forces between the particles; however the addition of too much may also result in flocculation and is an unnecessary expense. There are

several methods available to approximate the quantity of dispersing additive required. The amount of dispersing agent required is generally based on the particle surface area and the absorption properties of the material.

The amount of oil which can be adsorbed onto the surface of a particulate material can give an indication of dispersant content. For example, TiO_2 adsorbs a moderate amount of oil. The oil absorption ratio is 15–20 parts by weight of oil to 100 parts by weight of TiO_2 [239, 240]. However the surface area of the particle can also provide a guide to how much dispersant is required [241]. Larger particle size dispersions can be stabilized with a relatively low amount of the dispersant (less than 1-3 wt% of the solids). As the particle size is reduced, the surface area is increased and therefore a much higher dispersant to particle (D/P) ratio is needed (up to 100-200 wt% of the solids) [242]. Other factors also need to be considered including: the application, the binder and the particular additive.

Three different commercially available dispersing additives were trialled to determine which was most suited. Zetasperse-1200 [243], Tween-80 (Polysorbate 80) [244] and Triton X-100 [136] have all been identified from the literature for their ability to aid dispersion and increase stability for aqueous polar particle dispersions such as TiO_2. Table 4.1 outlines the key components, viscosity and boiling point of each.

Table 4.1 - Active components, viscosity and boiling point of dispersants, provided from manufacturers' datasheets

Dispersant	Active components	Viscosity at 25°C, cP	Boiling point, °C
Zetasperse-1200	Tetramethyl-5-decyne-4,7-diol Polyethylene glycol	300	188
Tween-80	Polyethylene sorbitol ester	400-620	110
Triton X-100	Polyethylene glycol tert-octylphenyl ether	270	270

As previously discussed, surfactants and dispersants work by forming a layer around the dispersed material to prevent them from touching and forming agglomerates. However, surfactants and dispersants can also encapsulate air bubbles within the liquid, which can later prevent the fluid from jetting through an inkjet nozzle. To reduce the problem of stabilized gas bubbles, liquids can be simply degassed by ultrasonic processing, therefore the liquid mixtures were sonicated before the addition of nanoparticles to remove any air bubbles. Subsequent mixing was then undertaken at speeds which prevent the formation of new bubbles.

Each dispersant was mixed into water using a magnetic stirrer for 8 hours at 50 ºC on a hot plate. The dispersant to TiO_2 ratio (wt%/wt%) was varied between 0 and 3 to investigate their ability to aid dispersion. Each premixed solution was then slowly added to TiO_2 nanoparticles to produce a concentration of 1 wt%.

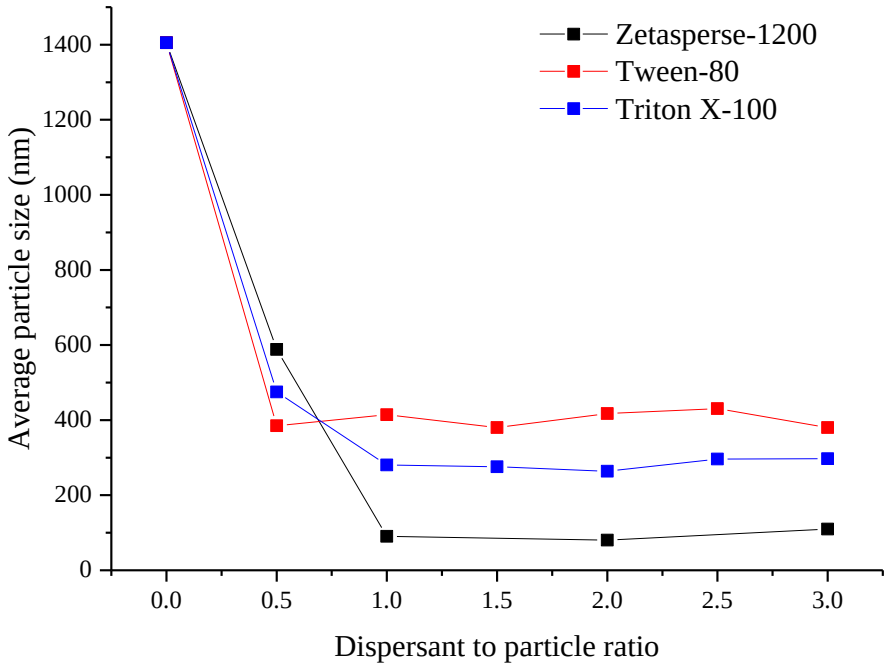

Figure 4.7 - Influence of dispersant quantity on average particle size

Figure 4.7 illustrates the effect of type and amount of dispersant on the average agglomerate size within the TiO_2 suspensions, measured using DLS. It can be seen that the use of Zetasperse-1200 within TiO_2 suspensions resulted in the smallest average agglomerate size, followed by Triton X-100 and Tween-80. The smallest average agglomerates were found after a dispersant to particle (D/P) ratio of 1 for all types of dispersant. To minimise the additional cost associated with dispersant, further investigation into the optimal dispersant content between a D/P ratio of 0 to 1 should be considered. However for the purpose of this project, the results show that a ratio of polymer dispersant to particle of one is enough to overcome the attractive forces between particles. It was noted that in this case, the addition of further dispersant did not result in any noticeable change in average agglomerate size.

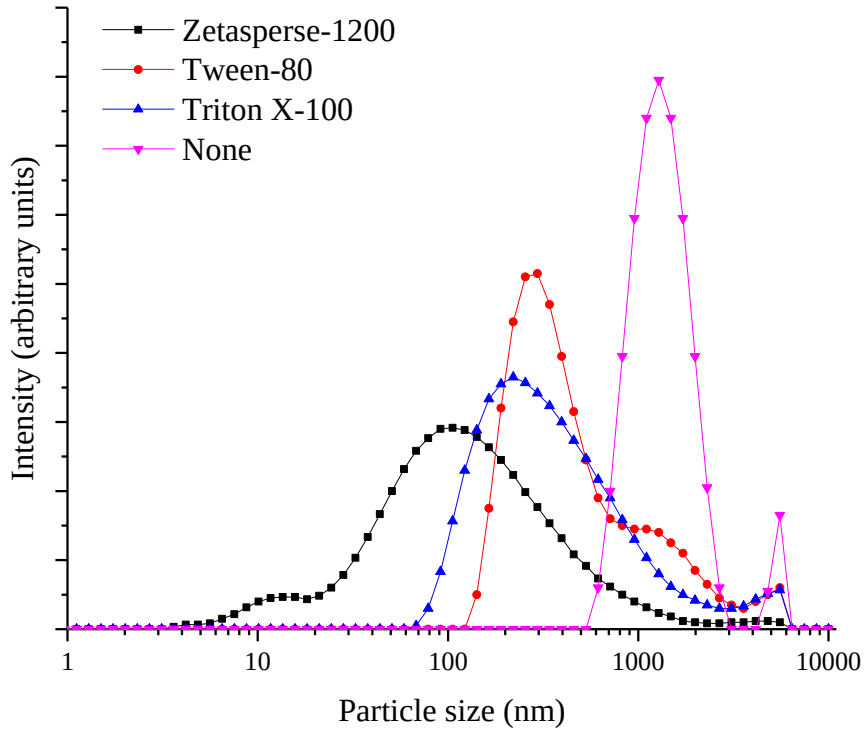

Figure 4.8 - Particle size distribution of aqueous TiO_2 solutions with a dispersant to particle ratio (wt%/wt%) of 1

Figure 4.8 shows the distribution of particle size with a D/P of 1, where a reduction in average particle size can be observed for all dispersants compared to TiO_2 alone. A large spread of particle sizes can still be observed; indicating that filtration prior to printing is still advisable to remove any large agglomerates within the solution.

According to the datasheets Tween-80 has the highest molar mass of 1310 g/mol, followed by Triton X-100 with a molar mass of 647 g/mol. The molar mass of Zetasperse-1200 could not be found, however, the molar mass of the two active components tetramethyl-5-decyne-4,7-diol and polyethylene glycol are 22.36 g/mol and 76.09 g/mol respectively indicating that it has the lowest molar mass of the three dispersants trialled. This suggests that the dispersants with a lower molar mass

resulted in suspensions with the smallest average agglomerate size. Polymers of high molecular weight have longer carbon chain that can adsorb onto the surfaces of many nanoparticles. This could likely result in bonding between nanoparticles, resulting in larger agglomerates.

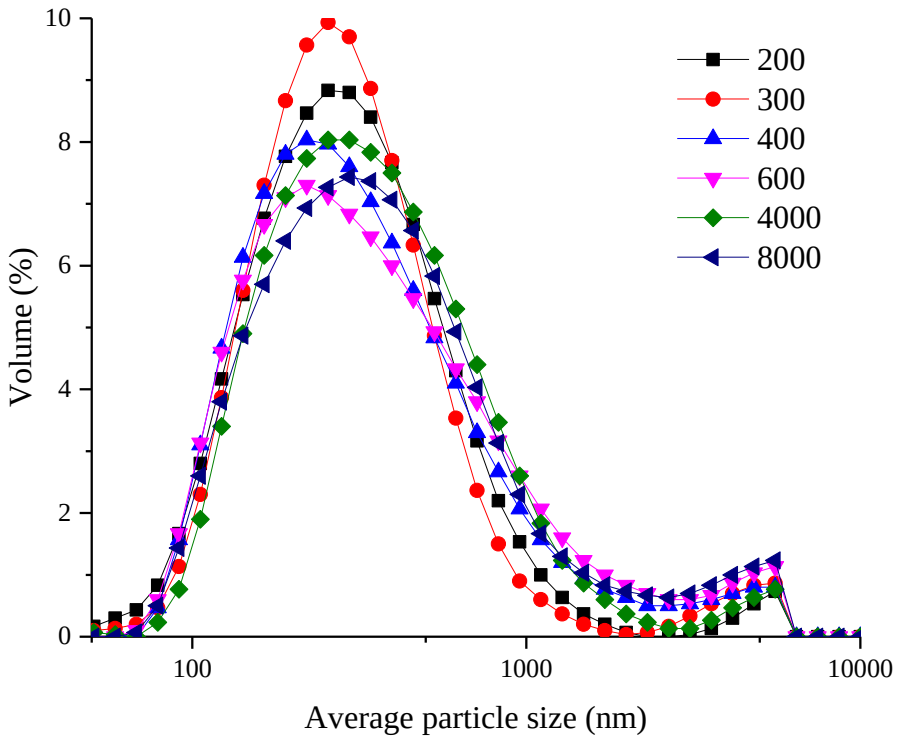

Figure 4.9 - Particle size distribution of TiO_2 aqueous suspensions with polyethylene glycol of varying molecular weight

To further investigate the link between molar mass and average agglomerate size, polyethylene glycol in varying molecular weight was added as a dispersant to an aqueous solution of TiO_2, with D/P ratio of 1. Each dispersant was mixed into water using a magnetic stirrer for 8 hours at 50 ºC on a hot plate. Each premixed solution was then slowly added to TiO_2 nanoparticles to produce a concentration of 1 wt%. Figure 4.9 shows the measured size distribution of agglomerates for each. The results

show that there is a small difference between each particle size distribution, with a standard deviation of 19.72 nm between the average hydrodynamic diameters. This can be more easily observed in Figure 4.10, where the average particle size is plotted against the molecular weight of PEG. The figure shows a small increase in average agglomerate size as the molecular weight of PEG increases.

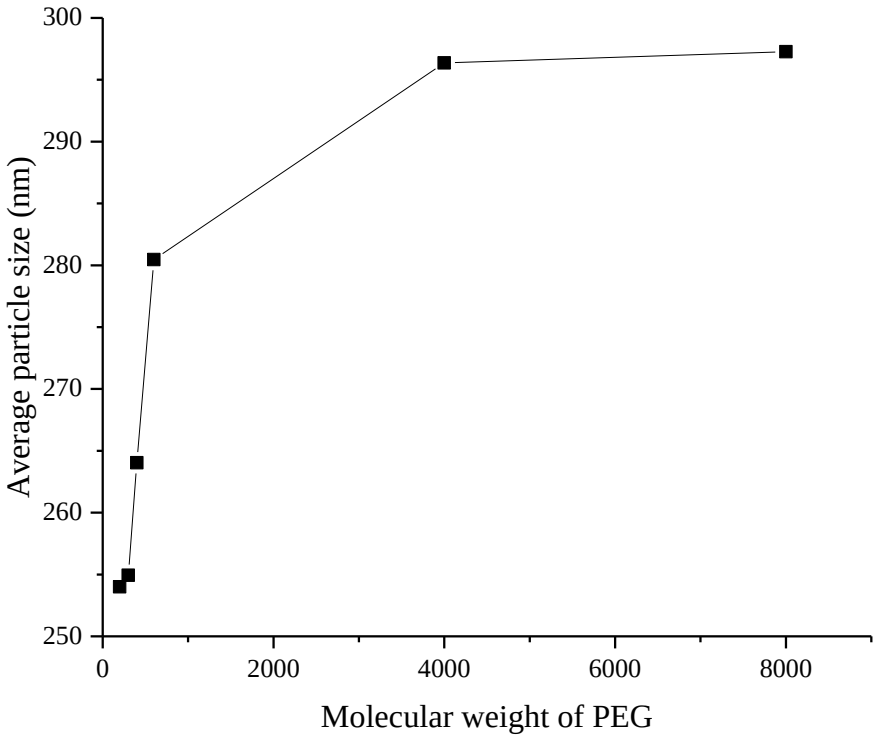

Figure 4.10 - Average particle size of TiO_2 aqueous suspensions with polyethylene glycol of varying molecular weight

As previously mentioned, surface tension and viscosity are two of the most important factors to consider when formulating an ink. The use of dispersing agents can influence the viscosity, with some having a significant thinning effect [122]. Zetasperse-1200 dispersant resulted in the smallest average agglomerate size, therefore was taken forward for further testing on viscosity and surface tension. The

rheological behaviour of the solutions were investigated using a microfluidic viscometer / rheometer from Malvern Instruments. Figure 4.11 shows that the average shear viscosity of 3 wt% TiO_2 nanoparticles in water was found to be 1.0 cP compared with 0.9 cP for water alone, indicating that the addition of nanoparticles results in a small increase in viscosity. This is to be expected since the literature suggests that the viscosity of nanoparticle suspensions depends on the nanoparticle size and concentration [245].

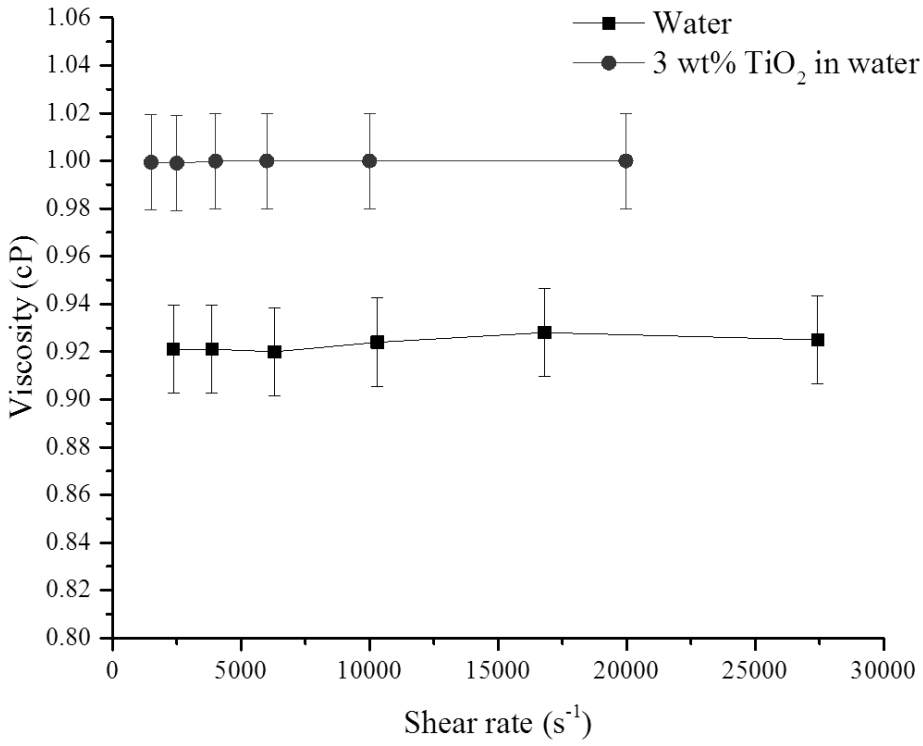

Figure 4.11 - Dynamic viscosity of TiO_2 dispersion compared to water

The surface energy of the ink must be reduced to between 25 mN/m and 40 mN/m to ensure that it is compatible with the inkjet printer. The addition of 3 wt% Zetasperse-1200 dispersant in water was calculated and resulted in a drop in surface energy from 72.80 mN/m to an average of 26.5 mN/m. A liquid will wet a solid surface when its

surface energy is lower than the solid's surface energy. The surface energy of the substrate was measured to ensure wettability and the results are outlined in the next section.

Deionised (DI) water was mixed with Zetasperse-1200 content from 0 to 5 wt% to investigate the influence on the dynamic viscosity. Figure 4.12 shows the dynamic viscosity of the solutions measured using a Brookfield viscometer with a small sample adapter at a shear rate of 264 s^{-1}. The figures shows how viscosity increases with Zetasperse-1200 content, however since the error bars are very significant further testing would need to be performed before an upward trend can be confidently reported.

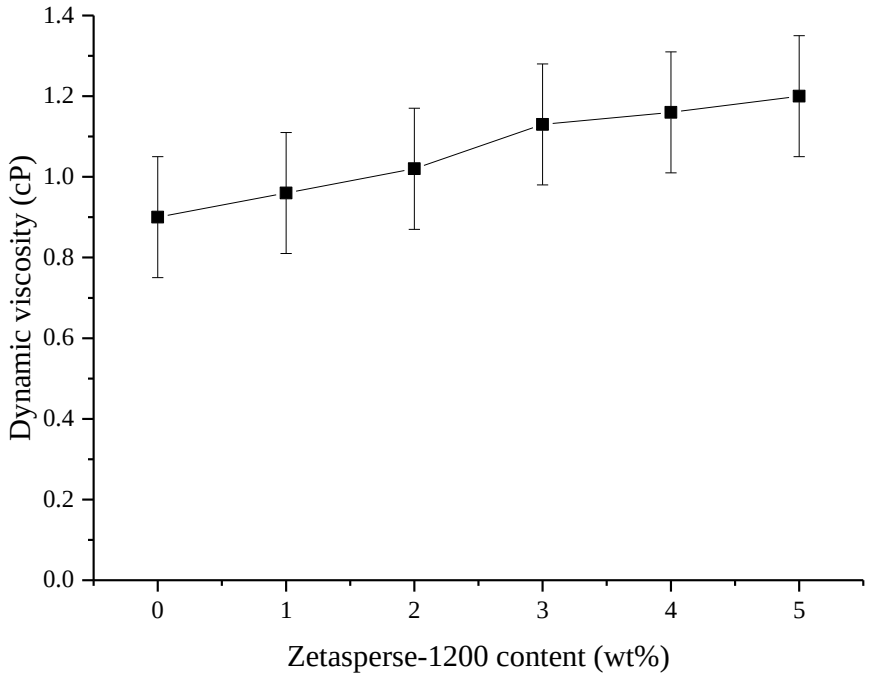

Figure 4.12 - Influence of dispersant content on dynamic viscosity

(at a shear rate of 264 s^{-1})

4.4 Inkjet printing trials and optimisation of the print parameters

Ink formulations underwent iterative testing of fluid properties while adjusting the specific components and proportions of each component until an optimal was reached. A TiO_2 nanoparticle aqueous ink was prepared using the following method:

- A 0.0001 M aqueous solution of hydrochloric acid (HCl) was prepared to produce a pH of approximately 4
- 3 wt% of Zetasperse-1200 dispersing additive
- The solution was mixed for 8 hours using a magnetic stirring bar to ensure homogeneity
- 3 wt% of titanium dioxide (TiO_2) nanoparticles was added to the solution
- The mixture was transferred into a round bottom flask and sonicated using a Hielscher UP200S ultrasonic probe for 10 minutes at a frequency of 60 Hz

The solution was left overnight, after which a thin layer of nanoparticles was observed at the bottom of the flask. The stable part of the suspension was removed using a syringe and sonicated again for a further 10 minutes to degas the ink. The ink was passed through two polyvinylidene fluoride (PVDF) filters, firstly 5 μm and secondly 1.2 μm to remove any large particulates and injected into a 1.5 ml Fujifilm-Dimatix cartridge.

On initial trials the TiO_2 dispersion jetted through the nozzles but quickly stopped. This was thought to be due to the evaporation of water at the nozzles such that the remaining particles produced a visible film on the surface of the nozzle which prevented jetting.

Humectants leave a thin wet film on the surface of the nozzle when it is idle to prevent a dry film from forming. Typical humectant materials are glycols such as diethylene glycol, polyethylene glycols, and propylene glycol methyl ethers [121]. Polyethylene glycol with a molecular weight of 400 (PEG 400), is a non-hazardous, water soluble polymer and liquid at 20 ˚C, making it compatible with the current ink formulation. The ink was prepared again with the addition of 25 wt% PEG 400 (purchased from Sigma-Aldrich) to act as a humectant to investigate whether it would prevent drying at the nozzles and enable long-term printing.

After the addition of PEG 400, it was observed that a layer of foam formed within the ink which did not appear to dissipate over several minutes. As previously discussed, air bubbles trapped within the ink can cause major problems for piezoelectric inkjet printers. They can counteract the pressure build-up at the nozzle, which prevents the formation of droplets [7]. Therefore 0.5 wt% defoaming agent from Airproducts was added which showed improvement. Increasing the content to 1 wt% reduced the foam completely. PEG 400 has a viscosity of 120 cP at 20 °C and therefore is expected to result in an increase in viscosity [246]. An average viscosity of 2.6 cP was measured using a microfluidic viscometer from Malvern instruments, up to a shear rate of 20,000 s^{-1} as shown in Figure 4.13.

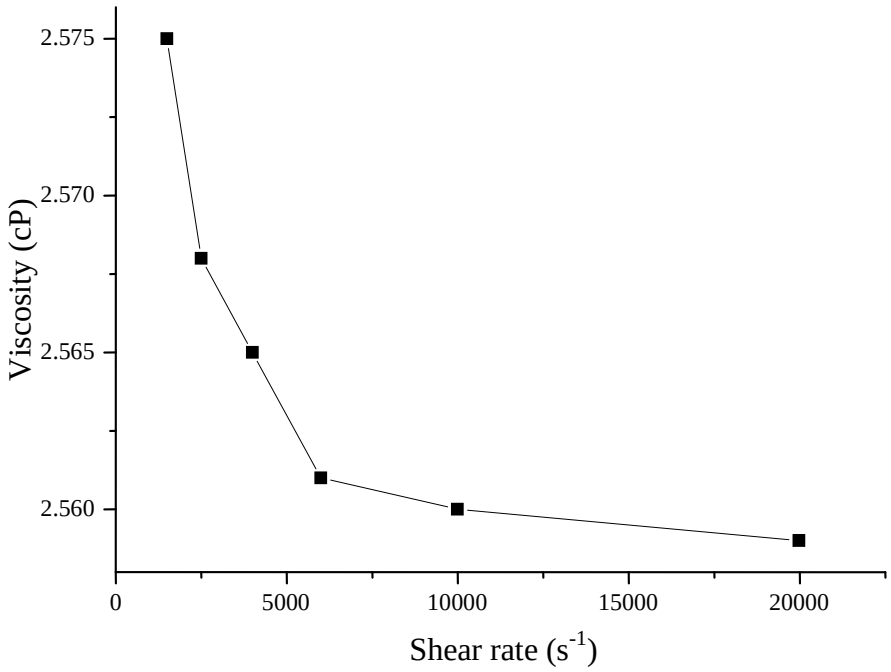

Figure 4.13 - Flow curve (viscosity vs. shear rate) for TiO_2 aqueous ink with 25 wt% PEG 400.

The new ink formulation was then sonicated again for a further 10 minutes in an ultrasonic bath, passed through a 1.2 μm polyvinylidene fluoride (PVDF) filter and injected into a 1.5 ml Fujifilm-Dimatix cartridge. Printing was carried out onto commercially available FTO sputter coated glass substrates.

As previously discussed in section 3.4.1, 'wetting' is an important factor in the adherence of two materials and occurs when the surface energy of the substrate is able to overcome the surface tension of a liquid. Therefore to further understand the interaction between the ink and the substrate surface, the surface energy of the substrate material was calculated based on contact angle measurements. The surface energy of the substrate materials was determined using a Theta Lite optical tensiometer from Biolin Scientific. The substrate was soaked in a 2 wt% solution of

cleaning detergent (Decon90) in deionized water for an hour to remove any surface contaminants. It was then rinsed thoroughly with deionized water to remove traces of the cleaning detergent. Three drops of water, ethylene glycol and diiodomethane were dispensed onto the test piece and the Fowkes method was used to calculate the total surface energy (γ).

The surface energy was calculated using a Theta Lite optical tensiometer from Biolin Scientific as described in section 3.4.1, to determine whether the ink would wet the substrate. The Fowkes method resulted in a surface free energy of 26.5 mN/m for the FTO coated glass. The surface tension of the TiO_2 ink was previously calculated to be an average of 26.3 mN/m. For adhesion to occur, the surface energy of the substrate should not exceed the surface tension of the fluid by more than 10-15 mN/m [221]. The surface tension of the ink and surface energy of the substrate are very similar, therefore the temperature of the substrate was heated to 60 ºC to encourage wetting of the ink.

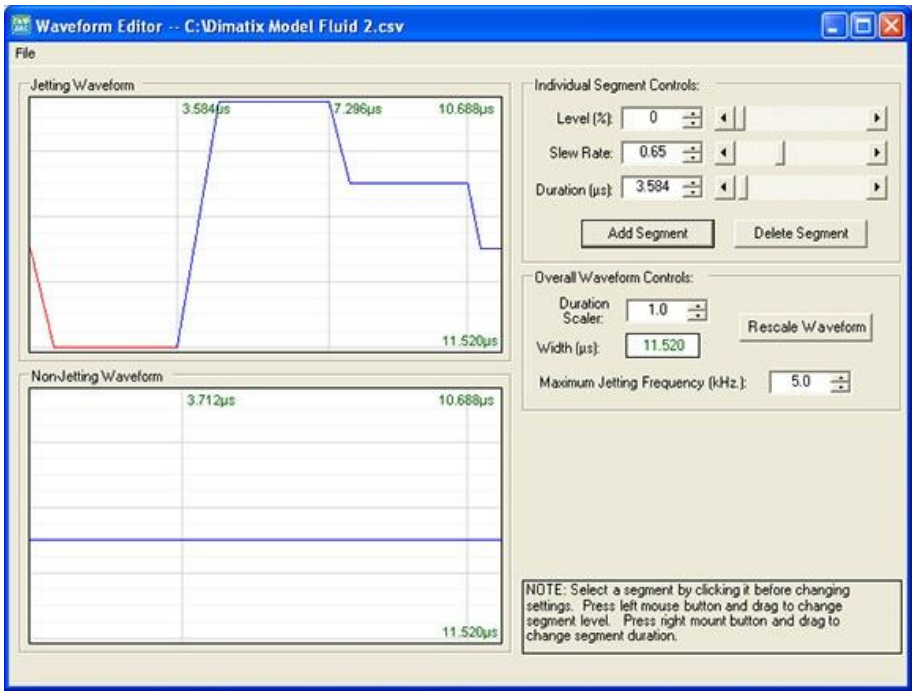

Figure 4.14 - Dimatix model fluid waveform.

The Drop Manager software was used to evaluate the quality of jetting from the nozzles. The "Dimatix Model Fluid" waveform (shown in Figure 4.14) was designed to work with model fluids (e.g. with a viscosity of 10-12 cP and a surface tension of 28-33 mN/m) and therefore was loaded and used as a starting point to monitor drop formation from the nozzles using the built-in camera. A jetting frequency of 5 kHz was set and the voltage waveform was adjusted to 10V to produce stable jetting of droplets with small tails (as shown in Figure 4.15) The nozzle temperature was maintained at 25 ºC. Elevated nozzle temperatures up to 60 ºC were investigated. However, the droplets deposited onto the substrate appeared less white and therefore it was assumed that the elevated temperatures was causing the inkjet nozzle to dispense the liquid components (e.g. solvent and humectants) leaving behind the TiO_2 nanoparticles.

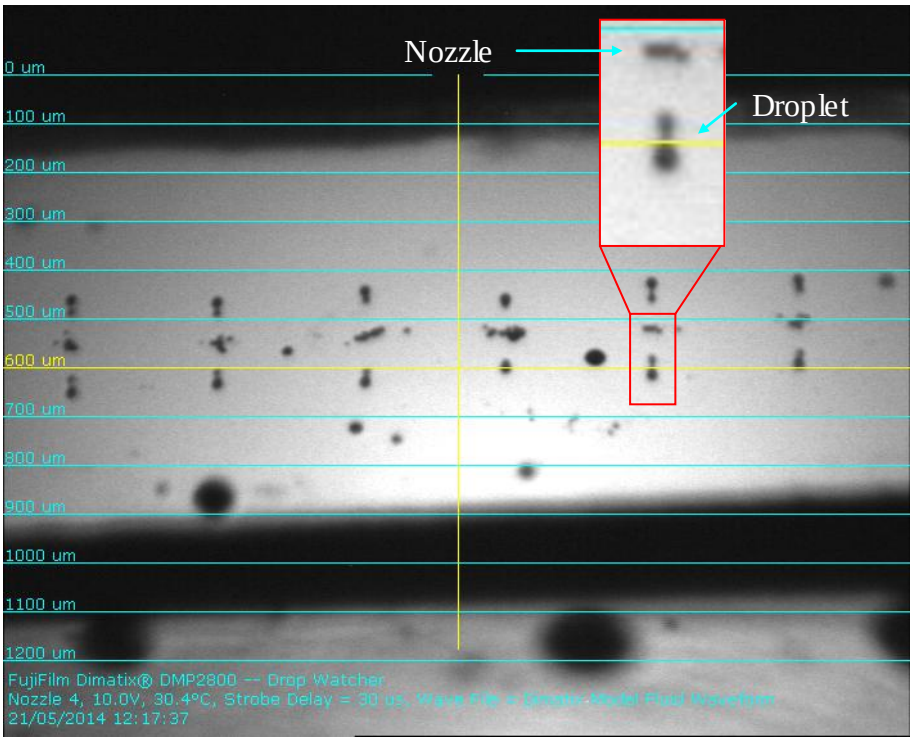

Figure 4.15 - TiO_2 ink droplet formation

To produce the optimal coating, the inkjet droplets should be dispensed from the nozzle so that overlapping discs are formed on the substrate. The Fujifilm-Dimatix printer is capable of altering the drop spacing between 5 µm to 100 µm. The drop size was used to determine the spacing; if they are too far apart it would result in holes within the printed layer. Generally, a drop spacing equal to the drop size is enough to form a uniform line. A drop size of 100 µm was used to print a single layer onto FTO coated glass, and a drop diameter of 40 µm was measured for individual drops using an optical microscope. A drop spacing of 40 µm did not form a uniform line and a drop spacing of 30 µm resulting excessive overlap resulting in bulging. Therefore a drop spacing of 35 µm was selected. Squares 5 mm by 5 mm were printed onto FTO coated glass which were placed on a hot plate at room temperature and then heated to 150 ºC for 30 minutes, followed by 250 ºC for a further 30 minutes.

4.5 Characteristion of the printed films

X-ray diffraction (XRD) analysis of the inkjet printed TiO_2 was performed using a Empyrean diffractometer from PANalytical with a CoKα wavelength (λ) of 1.7890 Angstroms (Å) and data was taken in the range of 20˚ to 95˚. Identification of TiO_2 crystalline phases for the printed film was achieved by comparison of their XRD patterns (shown in Figure 4.16) with those in the Joint Committee on Powder Diffraction Standards (JCPDS) database. Although the diffraction signal is dominated by the FTO-glass substrate, the XRD spectrum shows diffraction peaks at 29.57˚, which indicates TiO_2 in the anatase phase [237]. As previously mentioned, the crystallite size can be estimated from measured XRD peak half breadths [29.57˚ peak for anatase] by using the Scherrer equation. The angular width of the peak at

half maximum height was calculated from the XRD spectra to be 0.00680 radians and subsequently the crystal size was calculated to be 25 nm.

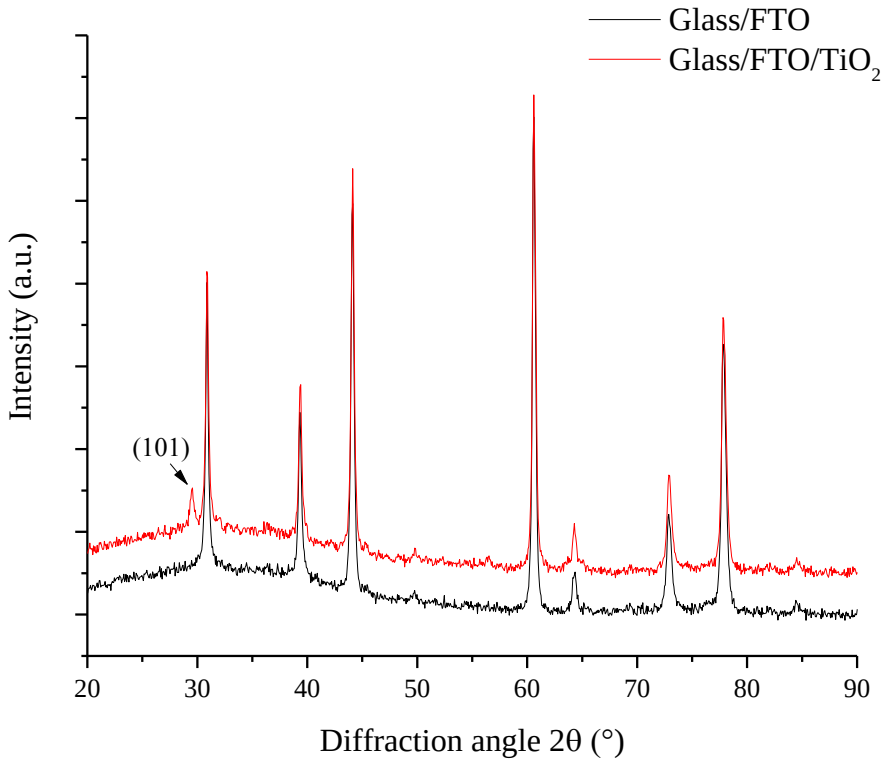

Figure 4.16 - XRD spectra of inkjet printed TiO_2 onto FTO glass.

The thickness of the printed layer was determined with a stylus surface profiler (Ambios XP-100). The diameter of the printed samples (after two printed layers) was found to be 4818 μm, with an average z-height of 1.8 μm (between the values of 1000 μm and 5500 μm on the x-axis) and a maximum z-height of 2.6 μm, as shown in Figure 4.17.

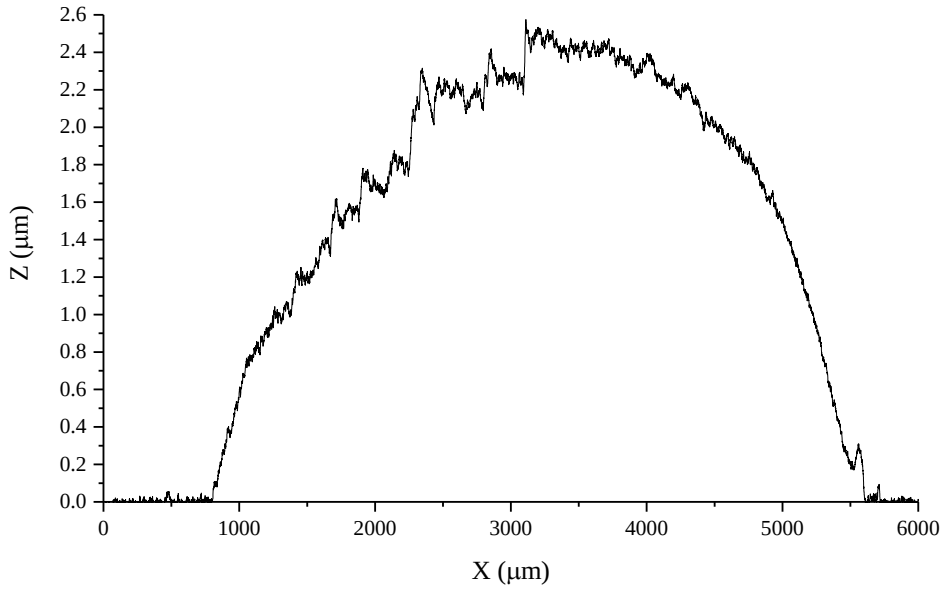

Figure 4.17 - Surface profile of inkjet printed TiO_2 onto FTO coated glass after 2 layers.

The printed films were analysed using a Carl Zeiss SEM, with an operating voltage of 5 kilovolts (kV). The SEM image of the printed TiO_2 film in Figure 4.18 and Figure 4.19, shows that the majority of particles retain the average size obtained from DLS, however many of the particles are connected into larger agglomerates. This will reduce the available surface area available for dye to be adsorbed onto the TiO_2 particles which could therefore negatively affect the overall conversion efficiency of the cell. The SEM images also show that the films were homogeneous without any cracks.

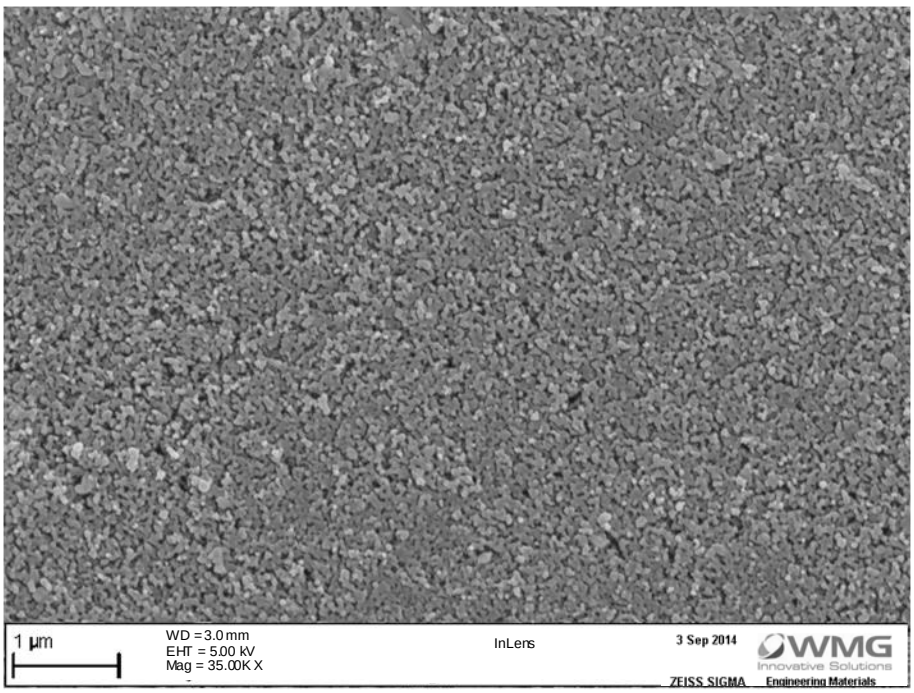

Figure 4.18 - SEM image of 2 layers of inkjet printed TiO_2 at low magnification.

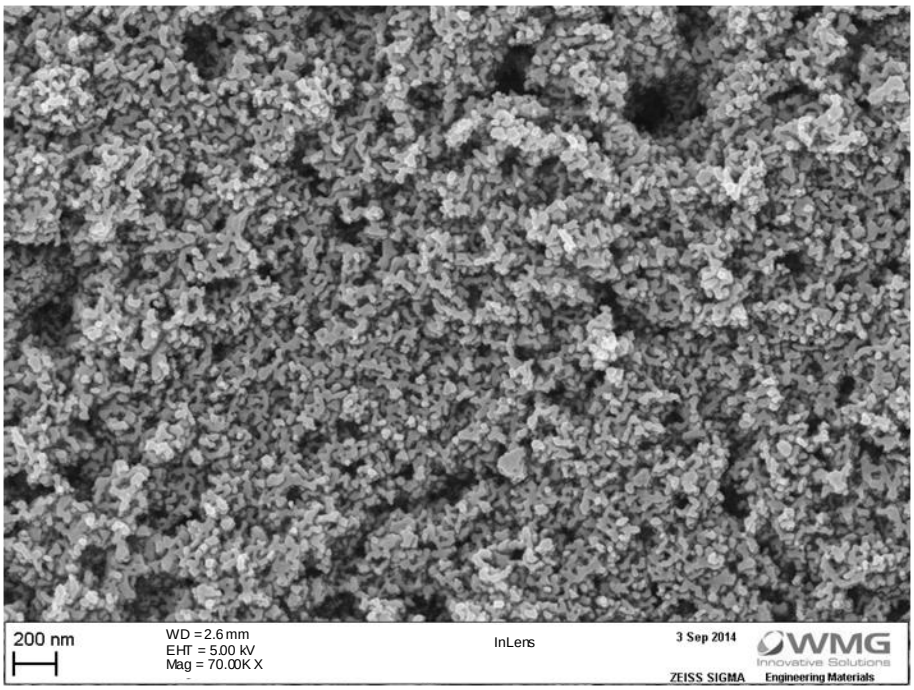

Figure 4.19 - SEM image of 2 layers of inkjet printed TiO_2 at high magnification.

The transmittance of the TiO_2 printed films was measured to determine how much sunlight would pass through the printed film. The transmittance was measured using a cary60 ultraviolet-visible (UV-Vis) spectrophotometer from Agilent Technologies,

in the wavelength range of 200-1100 nm. Visible light is defined as the wavelengths that are visible to most human eyes (390 to 700 nm) [247]. At a wavelength of 600 nm the FTO coated glass has a transmittance of 77.72 % compared with 48.66 % with the 2 layers of inkjet printed TiO_2. This indicates that a significant proportion of light is still being transmitted through the printed TiO_2 films.

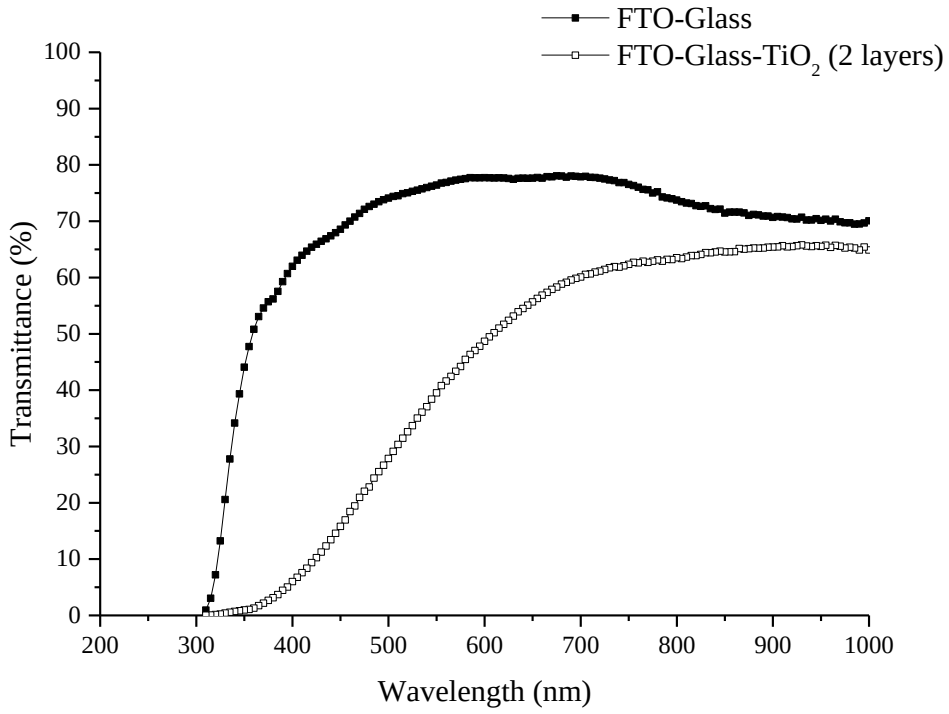

Figure 4.20 - Transmittance of light through 2 layers of inkjet printed TiO_2 films.

As previously mentioned, the efficiency of DSSCs is directly influenced by the thickness of the TiO_2 layer. The optimal thickness has been reported in several studies and it is widely accepted that somewhere between 9.5 - 20 µm produces the best results for traditional DSSCs incorporating an iodide/tri-iodide electrolyte [76, 85-89, 204, 248]. Therefore, the number of prints was increased to investigate the relationship with thickness. Figure 4.21 shows the average thickness and standard

deviation in relation to the number of printed layers. As the thickness increases, so does the standard deviation indicating an increase in the surface roughness.

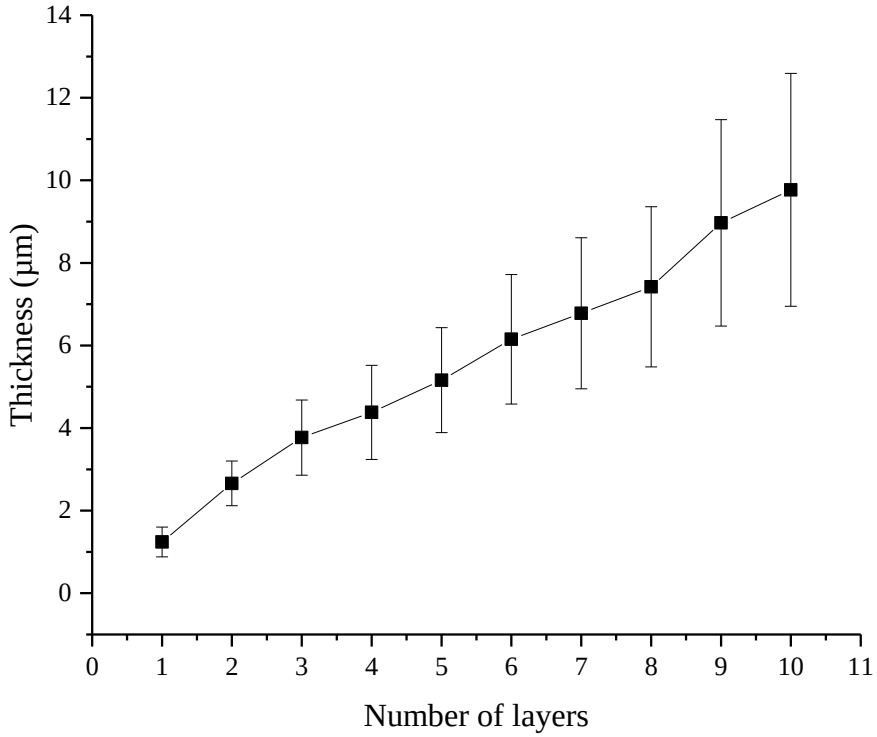

Figure 4.21 - Relationship between number of printed layers and thickness.

The same ink formulation was then used to print 10 layers onto FTO glass, which was then heated from room temperature to 250 ˚C to remove the solvent and humectant. However, this resulted in significant cracking and peeling from the glass substrate as shown in Figure 4.22 which was obtained using a Bruker ContourGT 3D Optical Microscope. The printed layer also had poor adhesion to the glass substrate and quickly peeled away, indicating that they would be unsuitable for dye-sensitization.

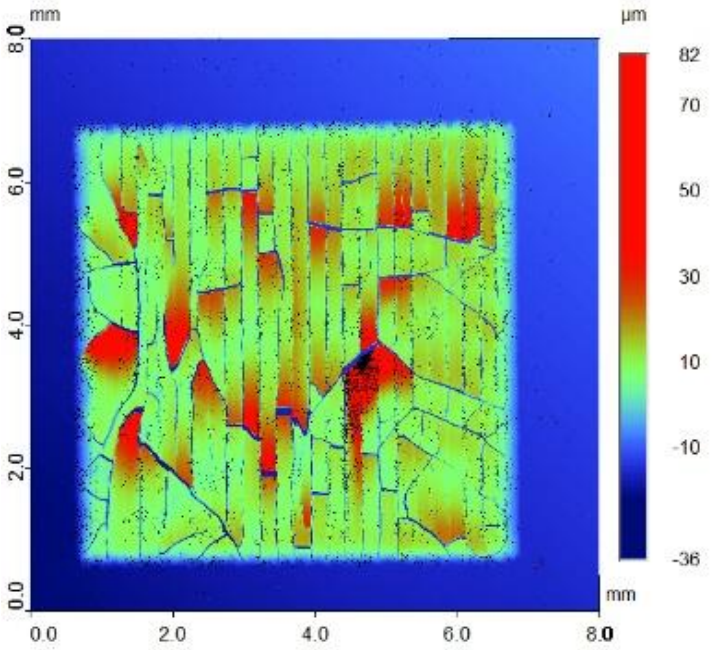

Figure 4.22 - Surface scan of the inkjet printed TiO_2 onto FTO coated glass (after 10 layers) using a Bruker ContourGT 3D Optical Microscope

4.6 Improving adhesion

4.6.1 Compression

One of the advantages of additive printing is that a range of rigid and flexible substrate materials can be used for printing. The use of flexible, thin and lightweight conducting plastic for DSSC applications has received significant attention recently for potential commercial applications [33]. However, due to the thermal instability of many plastic materials, high temperature sintering cannot be used. Mechanical compression has been reported to improve adhesion between the TiO_2 and the substrate and to promote interparticle connection within the printed layer resulting in crack-free films between 7 µm and 14 µm thick [33, 34]. This section investigates the use of compression for low-temperature preparation of the TiO_2 layer. The use of

the technique to overcome the issues of surface cracks and peeling of the coating from the substrate (seen in the previous section) is also considered.

TGA and DSC were performed to determine the thermal stability of the plastic substrates. PEN, PET and polyimide are commercially available films widely used in printed electronics applications. PET is reported to have an upper processing temperature of 150 ˚C and PEN is reported to have a slightly higher upper processing temperature of 180 ˚C [197]. However, both suffer with issues of shrinkage when heated. Polyimides, on the other hand, have high processing temperatures above 350˚C.

Figure 4.23 shows the DSC for ITO coated PET. The first change in heat flow is observed at 58 ºC which can be attributed to the glass transition temperature (T_g). A peak occurs at 260 ºC, which can be attributed to the melt transition temperature (T_m) and the TGA shows that it has fully degraded (T_d) at 464 ºC.

Figure 4.24 shows the DSC for ITO coated PEN. The first change in heat flow is observed at 47 ºC which can be attributed to the glass transition temperature (T_g). A peak occurs at 267 ºC, which can be attributed to the melt transition temperature (T_m) and the TGA shows that it has fully degraded (T_d) at 470 ºC.

Figure 4.25 shows that the polyimide film received from Dupont has excellent thermal stability. There are no clear peaks (positive or negative) until a small peak is observed at 521 ˚C. According to the literature, a second order transition occurs in polyimide between 360 °C and 410 °C and is assumed to be the glass transition temperature [249]. The sample provided was a non-commercial clear prototype film and was expected to perform well at high temperatures. It was therefore assumed that

the T_g occurred at 521 ˚C. Degradation (T_d) then occurred at a temperature of 600 ˚C.

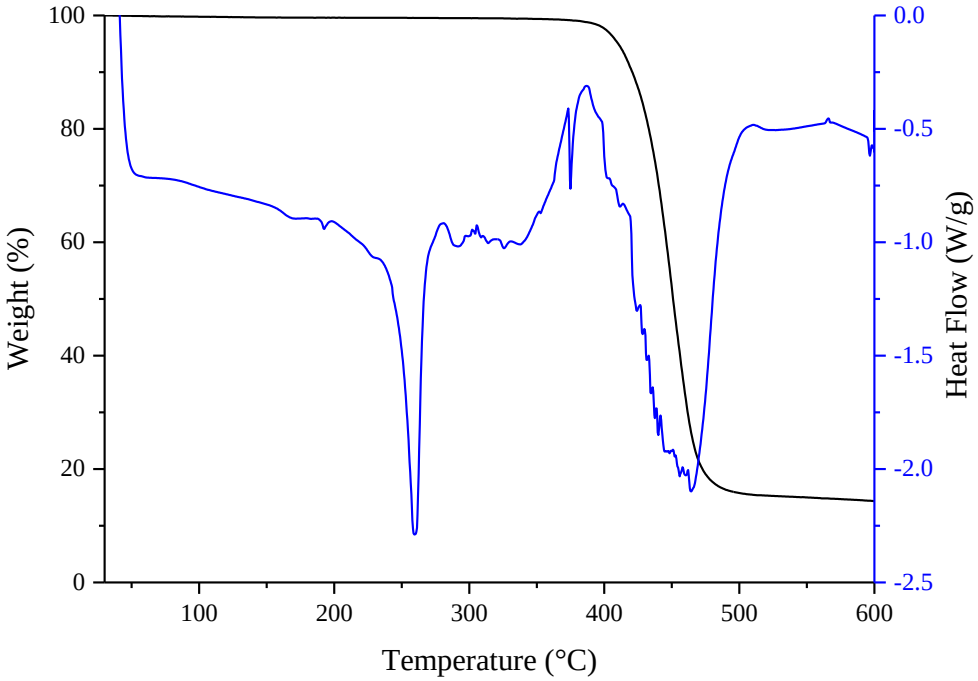

Figure 4.23 - Thermal analysis of ITO coated PET film

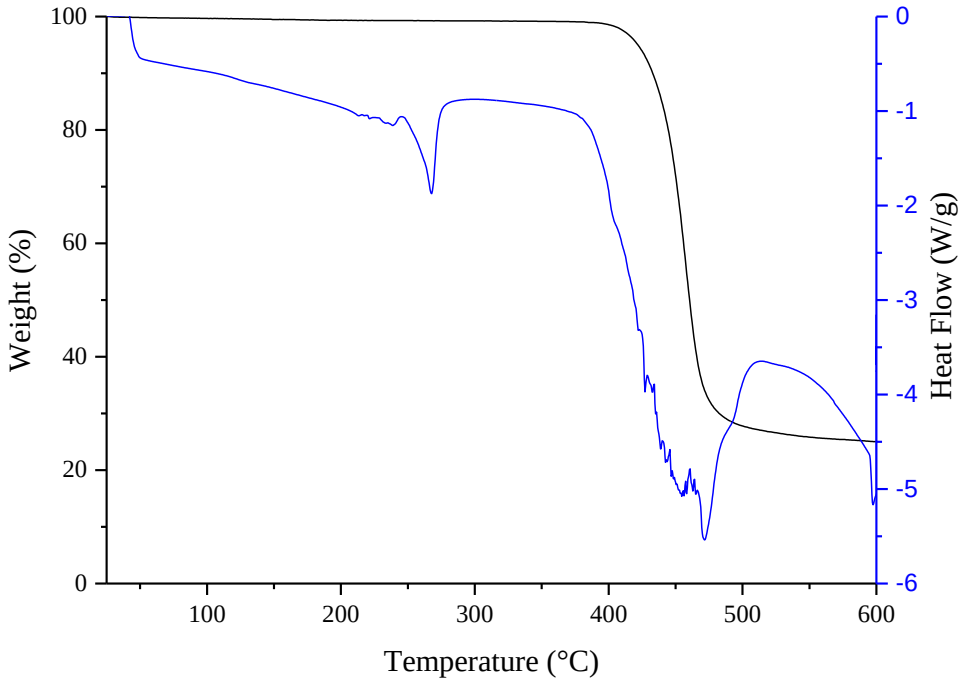

Figure 4.24 - Thermal analysis of ITO coated PEN film

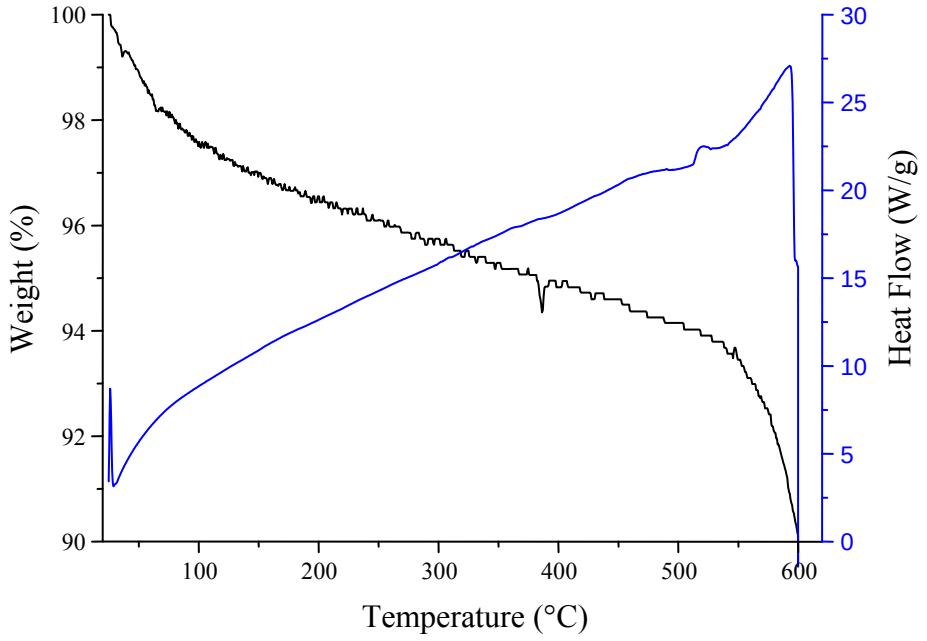

Figure 4.25 - Thermal analysis of Dupont polyimide film

To further understand the likely interaction between the ink and the substrate material, the surface energy of the each was calculated based on contact angle measurements as described in section 4.4. The use of surface treatment using methods such as corona [114], plasma [250] and chemical etching [125] could also be used to modify the surface energy and improve wettability.

Table 4.2 shows a comparison of the calculated surface energy for the plastic and glass substrate materials. The results indicate that ITO and FTO coatings reduce the surface energy of the substrates significantly. The high standard deviation observed for the glass microscope slide highlights significant irregularity with the surface and therefore further cleaning may have been required.

The surface tension of the aqueous TiO_2 ink was previously calculated to be an average of 26.3 mN/m. For adhesion to occur, the surface energy of the substrate should not exceed the surface tension of the fluid by more than 10-15 mN/m [221]. To enable good printing onto the plastic materials with a high surface energy, the surface tension of the ink could be increased to enable compatibility with the substrate. This may influence the printability of the ink, for example, high surface tension fluids have been shown to result in the formation of satellites [134]. The use of surface treatment using methods such as corona [114], plasma [223] and chemical etching [224] could also be used to modify the surface energy and improve wettability.

Table 4.2 - Surface energy of substrates

Substrate	Surface energy [mN/m]	Standard deviation [mN/m]
FTO coated glass	26.45	0.74
ITO coated PET	29.21	0.74
ITO coated PEN	32.82	0.61
PET	46.78	1.23
Dupont Polyimide	47.99	0.81
Glass microscope slide	63.03	7.52

Although the polyimide showed excellent thermal stability, a film pre-coated with a transparent conductive material could not be identified. The thermal performance of the PET and PEN were found to be similar and the surface energy of the ITO coated PET was closer to that of the FTO coated glass. Therefore the rest of this section continues with work printing onto ITO coated PET.

PEG 400 has a glass transition temperature (Tg) of -63 °C and a melting temperature (Tm) of 5.5 °C and is reported to degrade between 220 and 240ºC [251]. Ethylene glycol has a boiling point of between 195 and 198 °C. Differential scanning calorimetry (DSC) was conducted to find the temperature at which PEG 400 and ethylene glycol degrades to determine which would be most compatible with plastic substrates. Figure 4.26 shows the measured heat flow change of a PEG 400 (compared with a reference) with a peak observed at 221 ˚C. The DSC of ethylene glycol in Figure 4.27 shows a large peak which starts at 175 ˚C, indicating that the material starts degrading at a lower temperature than PEG 400.

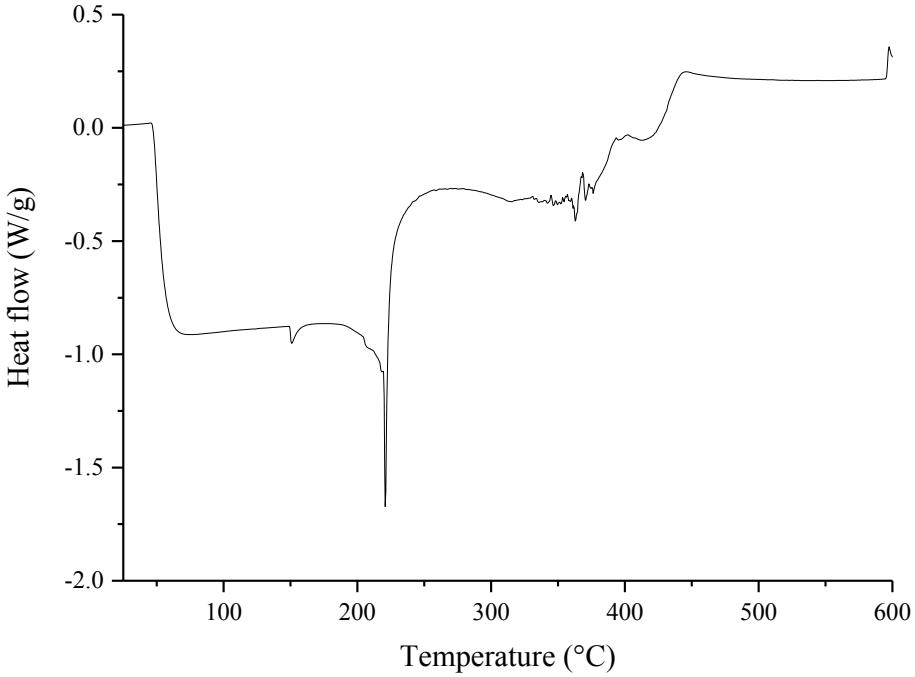

Figure 4.26 - Thermal analysis of PEG 400

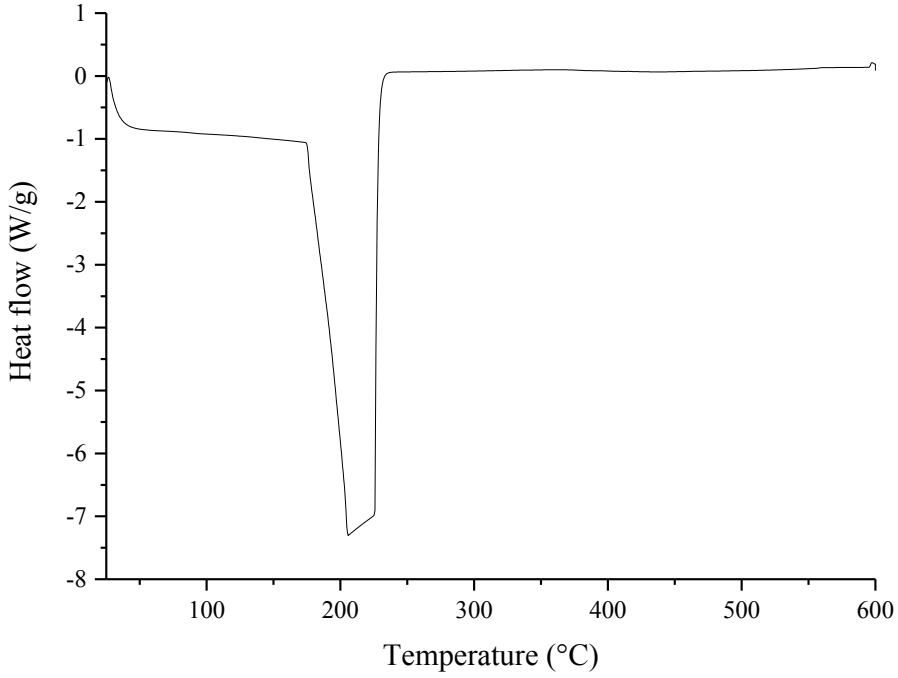

Figure 4.27 - Thermal analysis of ethylene glycol

Therefore, the ink was reformulated replacing PEG 400 with ethylene glycol as a humectant. The ink was passed through a 1.2 µm filter and injected into an ink cartridge. Printing was carried out as before, using the Dimatix Model Fluid waveform, a jetting frequency of 5 kHz, and the voltage waveform was adjusted to 10V and the nozzle temperature was maintained at 25 ºC. Since the surface energy of the FTO coated glass and ITO coated PET are similar, a drop spacing of 35 µm was maintained. Following inkjet printing onto ITO coated PET films, the samples were dried in a vacuum oven at 140 ºC for 30 minutes to remove the solvent carrier followed by cooling to room temperature. The films were then placed in between two polished aluminium sheets and loaded into a Collin200 M laboratory platen press and compressed at 25 MPa for 60 seconds.

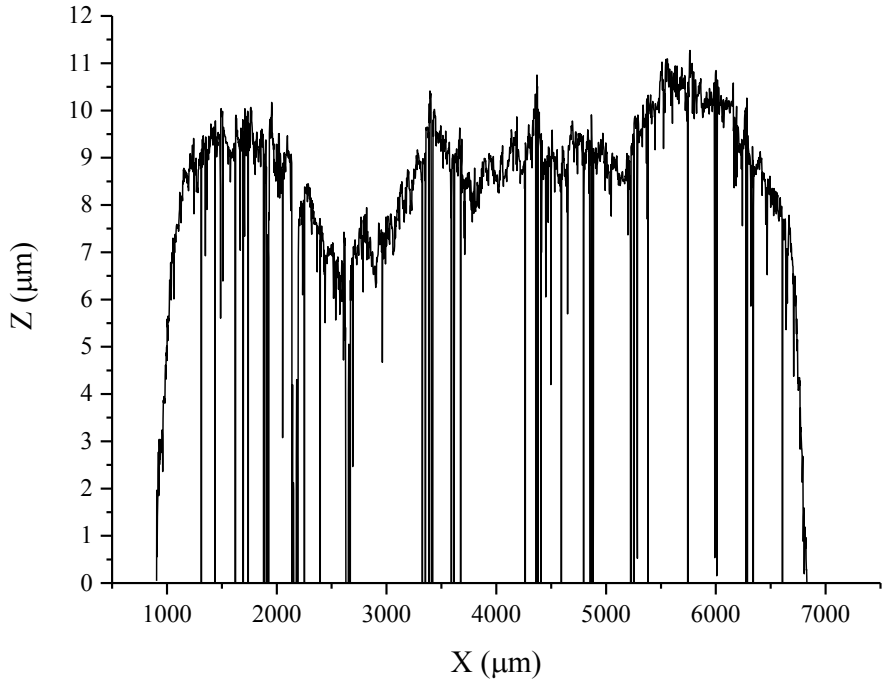

Figure 4.28 - Surface profile of inkjet printed TiO_2 onto ITO coated PET before compression

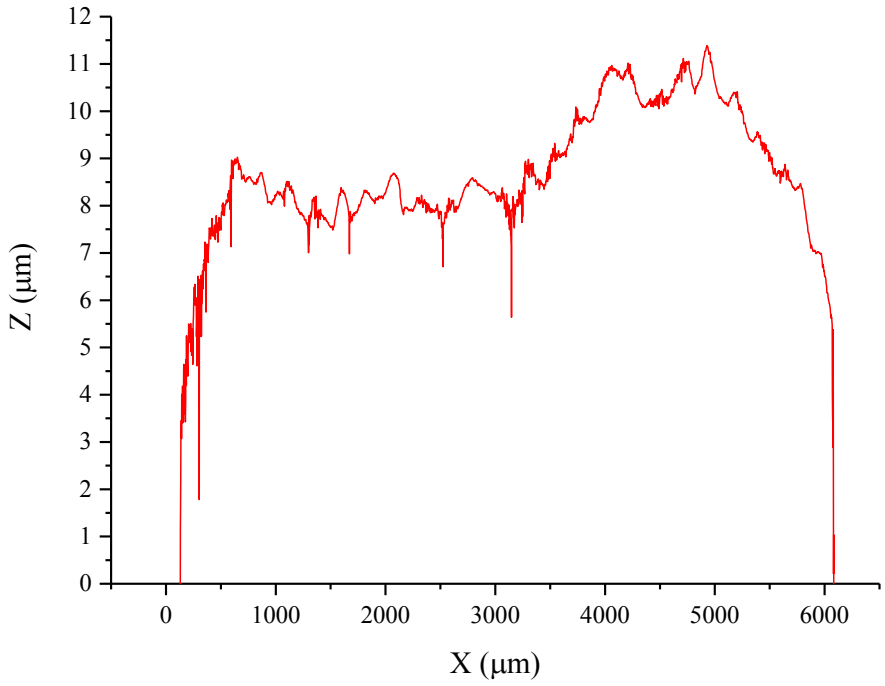

Figure 4.29 - Surface profile of inkjet printed TiO_2 onto ITO coated PET after compression

The surface of the printed layer was scanned using a 3D optical microscope (Bruker ContourGT). Figure 4.28 and Figure 4.29 show the surface profile of the TiO_2 films before and after compression. Before compression, it is clear that several cracks propagate through to the PET substrate and after compression the cracks appear to disappear. There is not a noticeable reduction in thickness after compression; however it does appear that the TiO_2 particles have been redistributed over the substrate so that voids within the coating are visibly reduced.

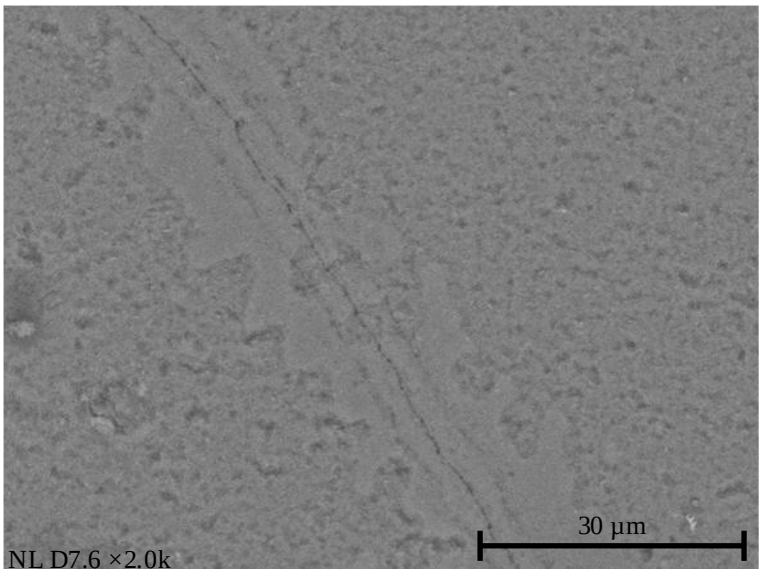

Figure 4.30 - SEM image of TiO_2 printed films onto ITO coated PET after compression

Figure 4.30 shows an SEM image of the films after compression. Although cracks can be observed on the surface, the inter-particle connection appears to have improved resulting in a less defined crack. However, the films still lacked sufficient adhesion with the substrate and separated upon sensitized in dye/ethanol solution. Therefore to further try and overcome the issue of adhesion, the next section will investigate the use of binder materials within the ink formation.

4.6.2 Evaluation of binder materials

In order to overcome the issues of surface cracks and peeling of the coating from the substrate seen in the previous section, an investigation was performed on binder materials. The incorporation of binders within inks enable crack free films to be printed. Without the binder, it is very difficult to control the film consistency over larger areas [32]. Binder-free formulations also suffer from poor inter-particle adhesion which can lead to cracking and poor substrate adhesion which can in turn lead to delamination. To improve the adhesion of the TiO_2 films, the addition of organic binders was investigated. Cellulose-based binders are commonly

incorporated in large quantities into pastes for screen printing or doctor blading to produce the high viscosities of between 1000 and 10,000 cP [118] [119]. However, heat treatment is required post-deposition to completely remove these large amounts of material from the printed layers [120]. Cellulose-based binders have degradation temperatures higher than 300 ºC, however if used in small quantities within an ink any residue may aid adhesion without compromising too much on the functionality of the printed device [137, 252, 253].

Figure 4.31 shows the TGA results of methyl cellulose (MC), hydroxyethylcellulose (HEC) and ethyl cellulose (EC) (purchased from Sigma Aldrich). During heat treatment, the cellulose binders melt and decompose. Higher temperature heat treatment result in more of the cellulose being removed; however a small amount of binder residue remains after heat treatment at 600 ºC. HEC has a lower initial degradation temperature then the other two cellulose materials tested and therefore was investigated further.

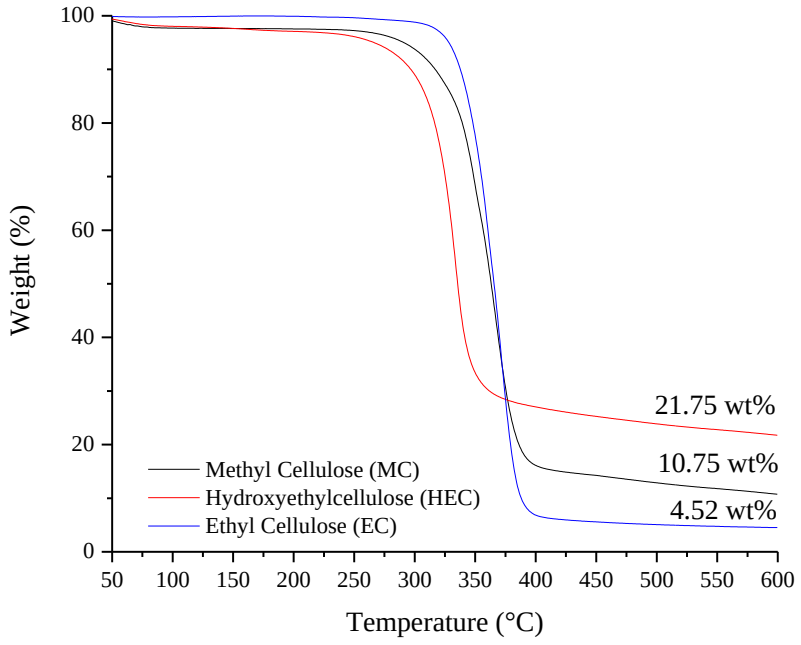

Figure 4.31 - TGA data for cellulose binders from 25 ºC to 450 ºC at 10 ºC/min.

HEC with an average molecular volume of 90,000 was added to DI water according the product information sheet. Approximately one third of the required water was heated to 80 ºC after which the cellulose powder was added with agitation until it was evenly dispersed. The remainder of the water was then added and the mixture was cooled to room temperature with continued agitation for a further 30 minutes. In order to determine the ideal quality required within an ink formulation, the HEC content was increased from 1-6 wt% to create 6 samples. Once cooled to room temperature, the viscosity of each was measured using a Brookfield rotational viscometer with a small sample adapter at a shear rate of 19.8 s^{-1}. As expected, Figure 4.32 shows that the viscosity increases with respect to HEC content.

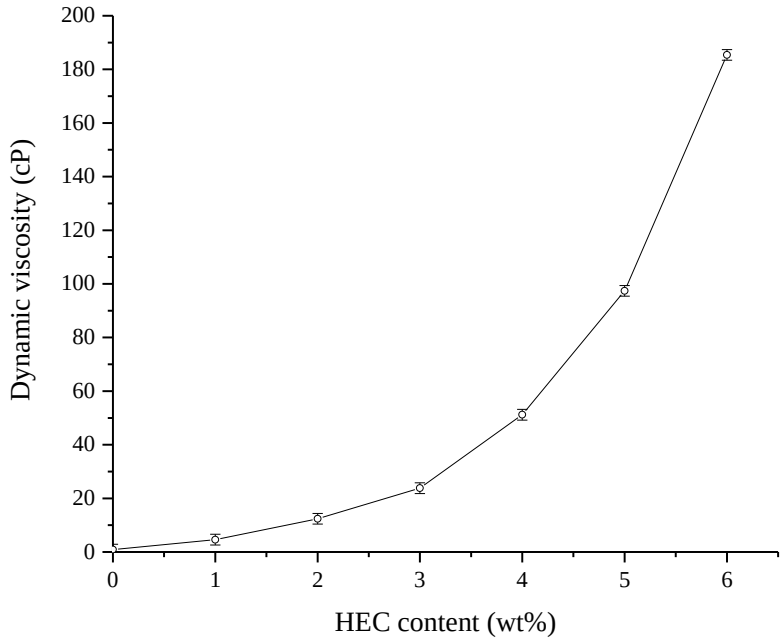

Figure 4.32 - Influence of HEC content in DI water on dynamic viscosity (at a shear rate of 19.8s^{-1}).

As previously discussed, the viscosity also has a huge influence on the reliability of printing and research suggests that for drop-on-demand printers a viscosity of less

20 cP should provide good droplet formation [127]. The viscosity at 3 wt% was 23.8 cP, therefore the HEC content within an ink formulation should be less than this to enable successful drop formation.

The aqueous TiO_2 ink was formulated the same as before (in section 4.4) with the addition of 2.5 wt% HEC. However after thorough mixing and sonication, the inks were unable to pass through a PVDF 1.2 µm syringe filter. The HEC content was reduced to 1.5 wt%, which successfully passed through the filter and therefore would be less likely clog the print head nozzles. The ink was loaded into a 1.5 ml Fuijifilm-Dimatix ink cartridge and printing was carried out onto commercially available FTO sputter coated glass substrates (TEC8, Pilkington with a sheet resistance of 8 Ω/sq). The Drop Manager software was used to evaluate the quality of jetting from the nozzles. The dimatix model fluid waveform (with a jetting frequency of 5 kHz) was used as a starting point to observe drop formation. High viscosity fluids require more energy to dispense a droplet e.g. a higher voltage is required. Following trials, the voltage waveform was increased to 18V to produce stable jetting of droplets. The nozzle temperature was maintained at 25 ºC.

Drop spacing was investigated between 50 µm to 10 µm using a 3D optical microscope (Bruker Contour GT) to observe surface roughness and height of printed features (shown in Figure 4.33). As before, the printed films were placed on a hot plate at 150 ºC for 30 minutes, followed by 250 ºC for a further 30 minutes. From Figure 4.33 it can be seen that the drops remained unconnected at 50 µm, at 40 µm the drops started to overlap and at 30 µm there was excessive overlap. As the lines were brought closer together, more of the material was deposited in a ridge. Excessively close spacing also resulted in an increase in film thickness as well as roughness. A drop-spacing of 35 µm was found to be optimal.

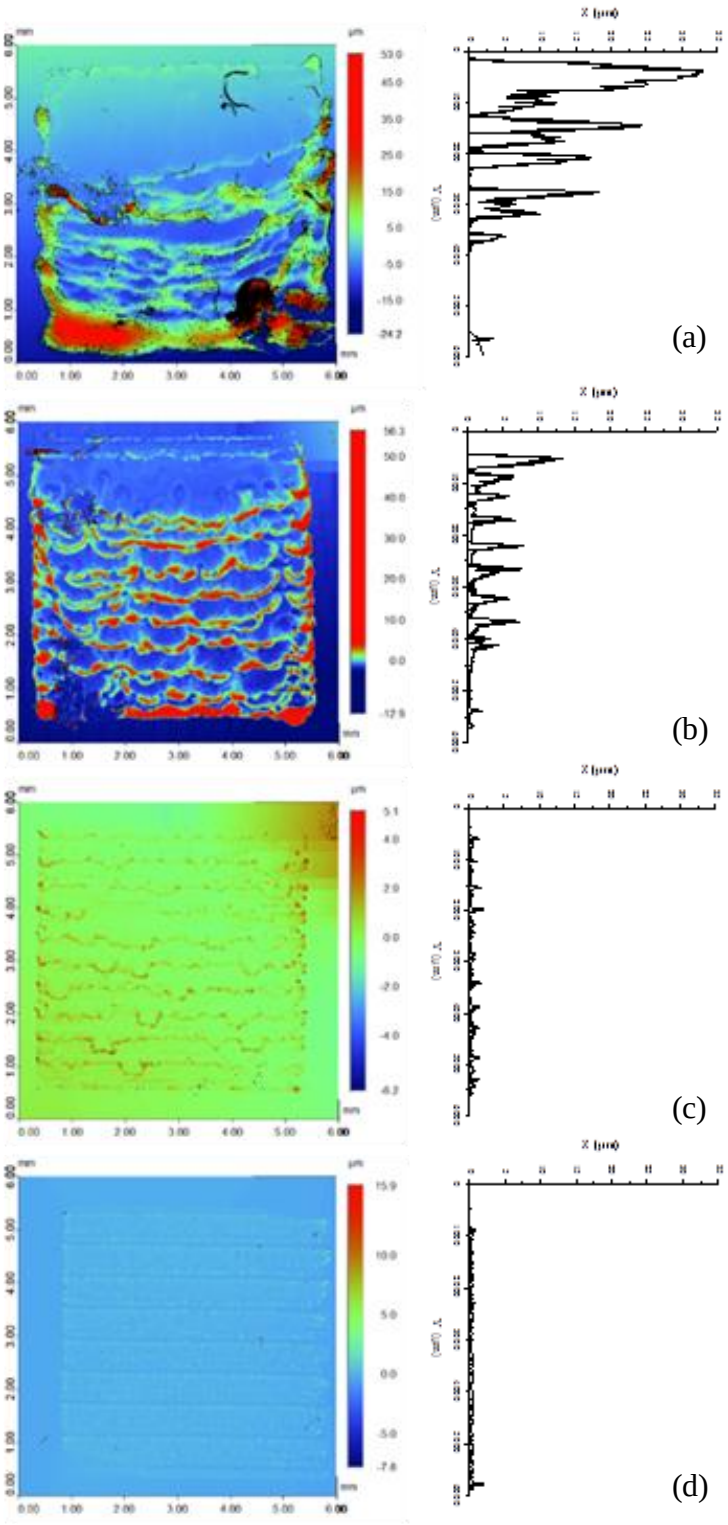

Figure 4.33 - Drop spacing of TiO_2 ink (with HEC binder) onto FTO glass investigated using a Bruker 3D optical microscope

(a) 10 µm (b) 20 µm (c) 40 µm (d) 50 µm

10 layers were printed and heated on a hot plate at 150 ºC for 30 minutes, followed by 250 ºC for a further 30 minutes to remove the solvent carrier and humectant. After heating to 250 ºC the films appeared a brown colouration as shown in Figure 4.34. This is likely to be due to residual organic matter, which will reduce dye uptake by blocking surface sorption sites. TiO_2 anatase eventually develops into rutile after heat treatment above 500 ºC [254]. Therefore, the films were placed into a vacuum oven from room temperature up to 450 ºC and maintained there for 60 minutes after which it was brought back down to room temperature and removed from the oven. The films then appeared white in colour indicating that that the majority of the cellulose binder had been burnt off.

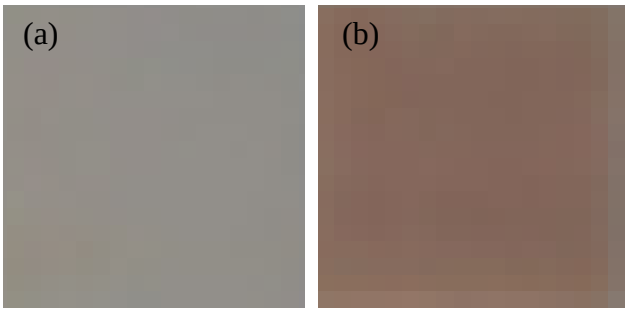

Figure 4.34 - Colour of TiO_2 after heating to (a) 150 ºC (b) 250 ºC

From Figure 4.35 it can be seen that the addition of the cellulose binder appeared to cause non-uniform drying. TiO_2 nanoparticles were transferred to the perimeter of the droplet resulting in a "coffee-ring" effect. However, the addition of the cellulose was successful in increasing the thickness. The thickness of printed layers was measured using a Bruker 3D optical microscope and found to have an average z-height of 7.64 μm (between the values of 1200 μm and 7000 μm on the x-axis) and a maximum z-height of 10.08 μm. The thicker areas were concentrated around the edges.

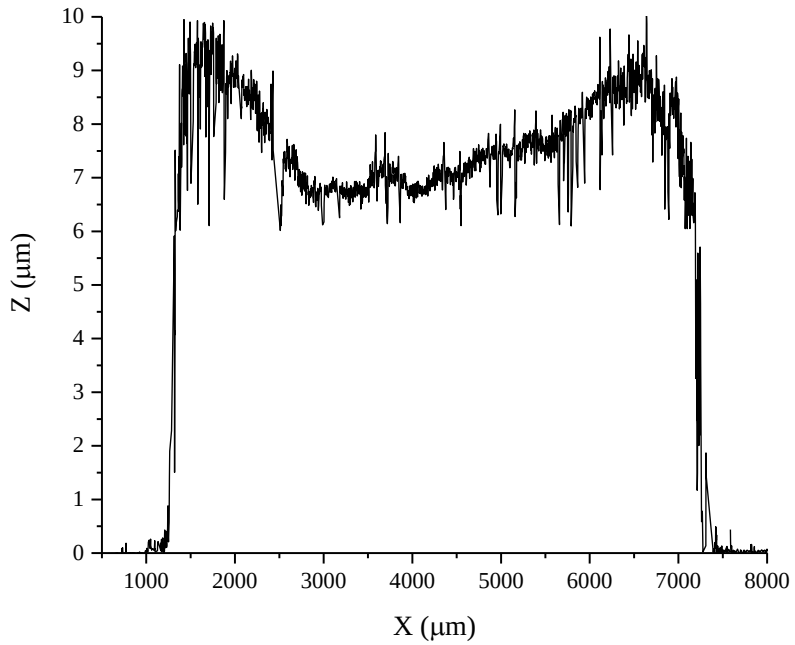

Figure 4.35 - Inkjet printed TiO_2 with HEC binder

The transmittance of the TiO_2 printed films was measured to determine how much sunlight would pass through the printed film. The transmittance was measured using a cary60 ultraviolet-visible (UV-Vis) spectrophotometer from Agilent Technologies, in the wavelength range of 200-1100 nm.At a wavelength of 600 nm the FTO coated glass has a transmittance of 77.72% compared with 48.66% with the 2 layers of inkjet printed TiO_2. Figure 4.36 shows that after 10 layers of inkjet printed TiO_2 with HEC, this is further decreased to 42.04%. However this still shows that a large proportion of visible light is able to pass through the printed film.

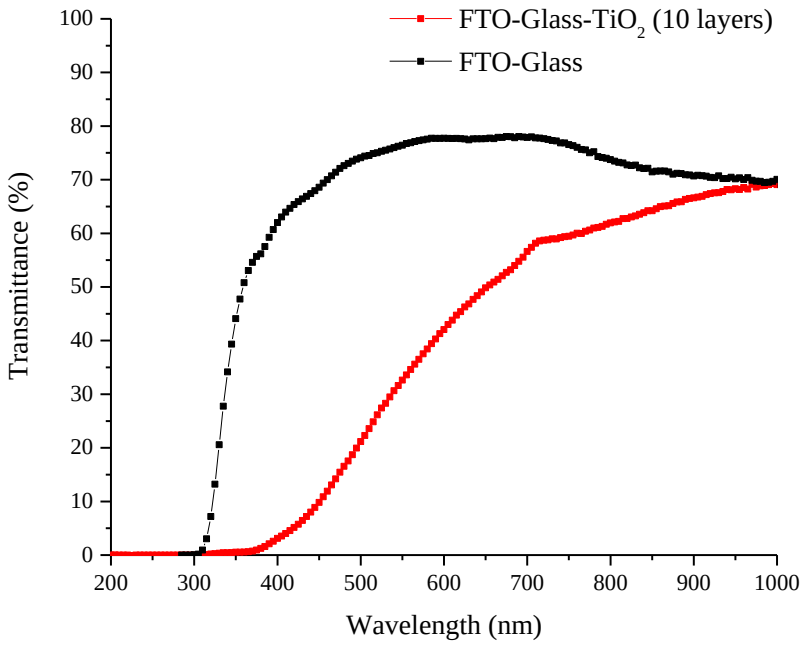

Figure 4.36 - Transmittance through 10 layers of inkjet printed TiO_2 films

4.7 DSSC manufacture and characterisation

To examine the commercial potential of inkjet printing in the manufacture of DSSCs, the printed films were produced into cells based on learning from previous sections. The key electrical performance parameters were used to characterize and compare the cells. Although hundreds of cells are customarily fabricated to ensure the reproducible performance of cells, to demonstrate the application of this work, efficiencies are reported as the mean of 3 devices.

In order to benchmark the proposed inkjet printed DSSC, a standard doctor-bladed cell was produced. TiO_2 photoelectrodes were prepared by doctor-blading a DSL 18NR-AO paste purchased from Dyesol, which has a blend of anatase particles of between 20 nm and 450 nm in size onto FTO glass (TEC8, Pilkington with a sheet resistance of 8 Ω/sq). The coatings must be heated slowly to avoid both cracking of

the glass substrate and on the surface of the TiO_2 film. The several heated stages were performed; the films were placed onto a hot plate and heated at 150 ˚C for 15 minutes, 250 ˚C for 15 minutes, 350 ˚C for 15 minutes, and 450 ˚C for 45 minutes and then returned to room temperature [78]. The thickness of the printed layer was determined with a stylus surface profiler (Ambios XP-100) and an average thickness value was calculated to be 18.0 μm as shown in Figure 4.37.

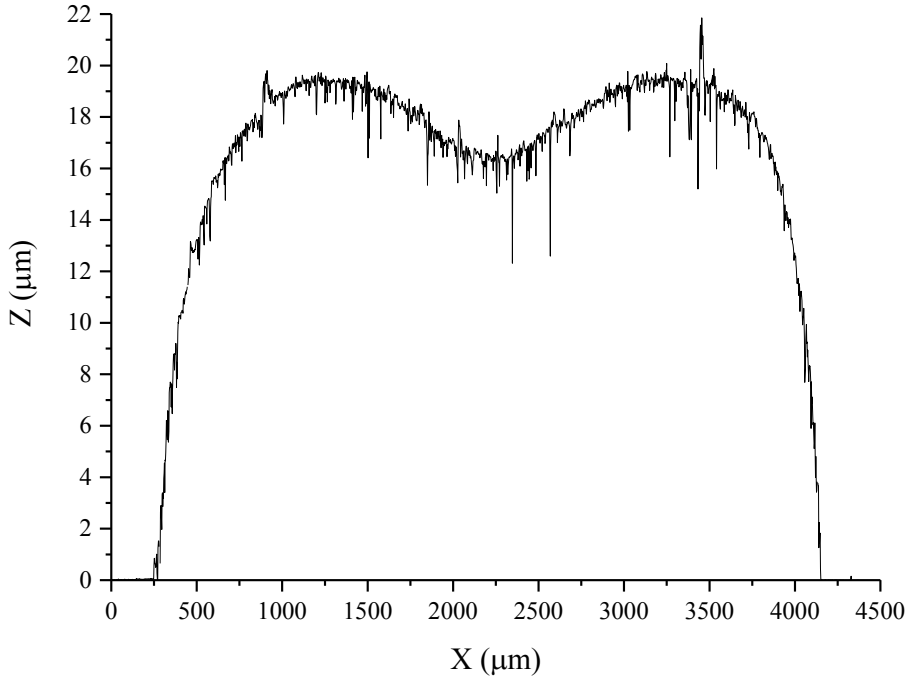

Figure 4.37 - Surface profile of the doctor-bladed TiO_2 onto FTO coated glass

The TiO_2 samples were made into a DSSC (illustrated in Figure 4.38) by soaking the printed substrates in a mixture solution of 20 ml of ethanol and 2 mg of N719 dye (Ruthenizer 535-bisTBA, Solaronix) at room temperature for 24 hours and dried in air. Surlyn film (Meltonix 1170 25 series, Solaronix) was then cut to size and sandwiched between the TiO_2 coated glass and the platinum coated glass (Solaronix). Iodide based low viscosity electrolyte with 50 mM of tri-iodide in

acetonitrile (AN-50, Solaronix) was used as the electrolyte and injected into a pre-drilled hole in the glass.

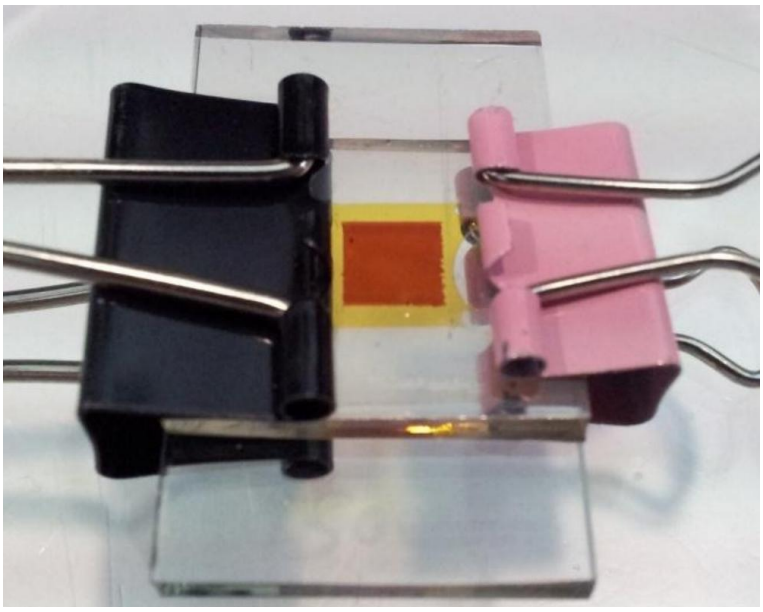

Figure 4.38 – Example of a DSSC incorporating a liquid electrolyte

The IV characteristics were measured under one sun (air mass 1.5, 100 mW/cm^2) by a source meter (Model 2400, Keithley Instrument, Inc.). These devices produced an average short circuit current (Jsc) of 11.12 mA/cm^2, open circuit voltage (Voc) of 756 mV and a fill factor (FF) of 0.57, resulting in a power conversion efficiency (PCE) of 4.8 ± 0.04%. This is similar to the performance of other cells reported using the same fabrication procedure, therefore was considered as a benchmark to which all further cells can be compared [255-257].

The inkjet printed TiO_2 samples were also made into a DSSC using the same method described above. Firstly, the glass substrates were cut into smaller manageable sizes (approximately 20 mm square) using a diamond glass cutter as shown in Figure 4.39.

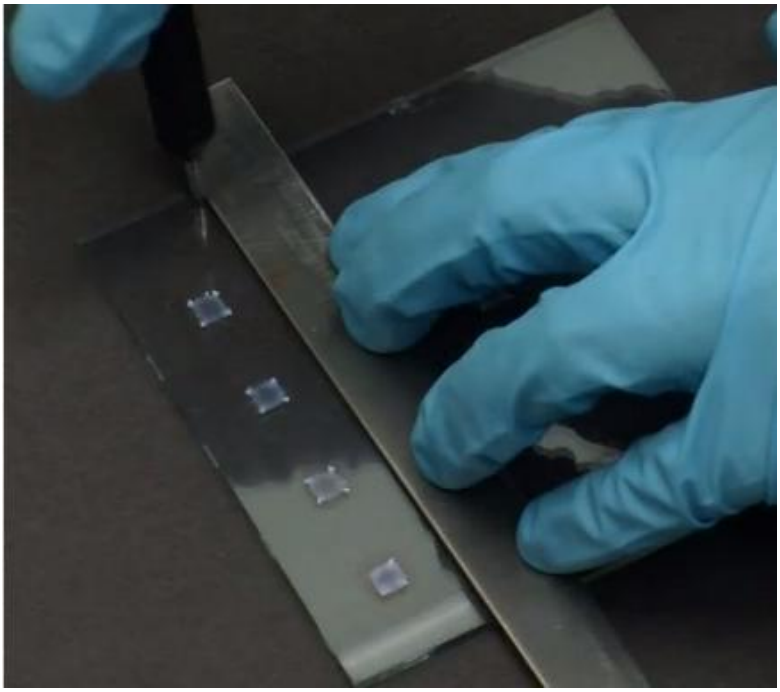

Figure 4.39 – Cutting the FTO glass with a diamond glass cutter

The IV characteristics were again measured under one sun (air mass 1.5, 100 mW/cm^2) by a source meter (Model 2400, Keithley Instrument, Inc.). The key performance characteristics of the cells are compared in Table 4.3 and Figure 4.40.

Table 4.3 - Performance of DSSCs with an active of 0.25 cm^2

	Inkjet printed (No binder)	Inkjet printed (HEC binder)	Doctor bladed benchmark
Isc [mA/cm^2]	9.42±0.33	6.02±0.56	11.12±0.05
Voc [mV]	756±2.50	706±2.92	756±4.90
FF	0.49±0.03	0.60±0.04	0.57±0.01
Efficiency [%]	3.50 ± 0.50	2.45 ± 0.42	4.80 ± 0.04
Average thickness [µm]	1.8	7.6	18.0

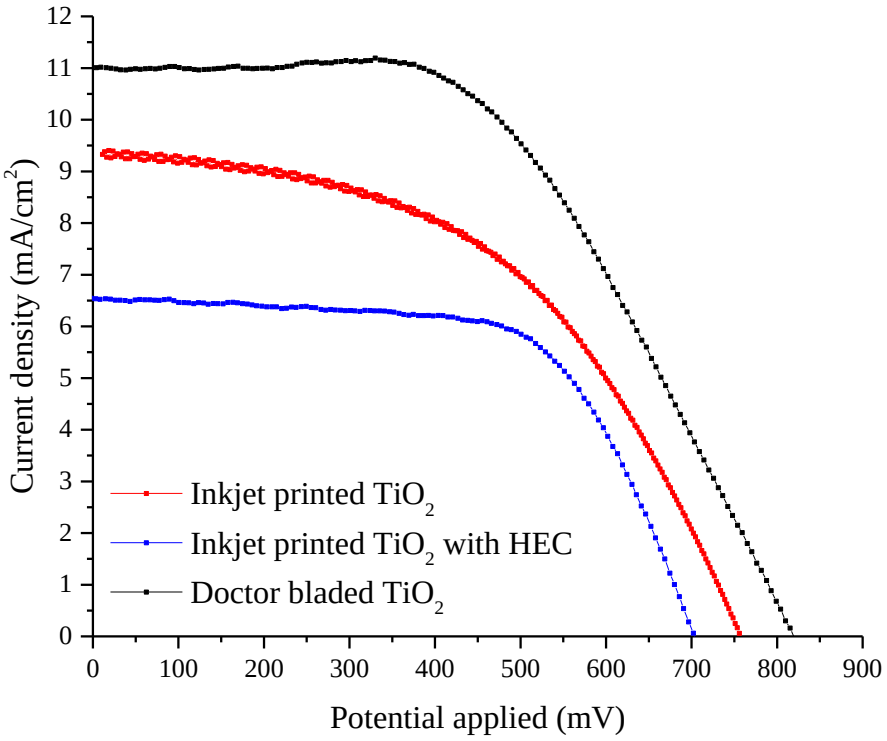

Figure 4.40 - Performance curves for DSSCs with inkjet printed TiO_2

The results show that when incorporated into traditional DSSCs, the ink without binder has a higher efficiency than the one with the HEC binder. There are several likely explanations for this. During heat treatment, the cellulose binders melt and decompose with higher temperatures resulting in more of the HEC being removed. A significant amount of binder residue (~25 wt %) remains after heat treatment at 450 ºC. This residue material reduces the amount of area available for dye to attach onto the surface of the TiO_2 particles. Additionally, it has been reported that with increasing sintering temperatures, the specific surface areas and porosity of TiO_2 nanoparticles steadily decreases [258]. This again reduces that amount of dye which can be adsorbed. Further testing to observe the dye absorption and desorption would need to be performed to confirm this. On the other hand, increased fill factor were

observed which may be due to better adhesion with the substrate which enables better charge transfer between the TiO_2 and FTO. Electrochemical Impedance Spectroscopy (EIS) testing would provide more information on whether this is the case. However the overall conclusion is that the inkjet printed variant has similar performance to the benchmark.

Chapter 5

Inkjet printed carbon black aqueous nanoparticle ink as a low cost replacement to platinum

5.1 Introduction

As previously discussed, there is a significant amount of research focussed on finding a replacement for the rare and expensive platinum material currently used as DSSCs. Carbon-based materials have been incorporated as counter electrodes in DSSCs to produce comparable efficiencies [109, 112]. This section reports on the inkjet printing of carbon nanoparticles. Once printed, the films will then be characterised to determine their suitability for use as a counter electrode in DSSCs.

5.2 Ink development

Carbon black is composed of nanometre sized primary particles which are bonded together to form aggregates or larger agglomerates of various shapes and structure. A sample of high conductivity carbon black (Vulcan XC72R) was received from James M. Brown Ltd, United Kingdom. This is a commercially available furnace black, which is made from petroleum feedstocks. "In the manufacturing of furnace black, the feedstock being injected into a high-temperature reactor where the hydrocarbon is cracked and dehydrogenated to form carbon with a quasi-graphitic microstructure" [259]. The isoelectric point has previously been found to be 5.36, therefore the pH needs to be raised to slightly above ten to improve the ease and stability of the dispersion [260]. In order to improve the dispersion of the nanoparticles within the ink, it is preferable to use a surfactant, generally of a non-ionic or anionic type. For

aqueous dispersions the percent of dispersing agent is dependent on both the particle size and percent of particles within the dispersion. The creation of a stable dispersion of carbon black particles is arguably the most challenging step in producing a high quality inkjet ink.

Following trials to determine the optimal components, a carbon nanoparticle aqueous ink was prepared using the following method:

- An aqueous solution of sodium hydroxide (NaOH) was prepared to produce a pH of approximately 11.The solution was mixed for 12 hours at 40 ºC using a large magnetic stirrer.
- 1 wt% of Zetasperse 3100 polymer dispersant was added to the base solution
- 25 wt% of PEG 400 was added to act as a humectant preventing drying at the nozzles and the blockage of nozzles.
- The solution was mixed for 8 hours using a magnetic stirring bar to ensure homogeneity.
- A few drops of the premixed solution was added to the carbon black (1 wt%) to create a concentrated paste, whilst stirring with a large magnetic stirrer. A dispersion of carbon black was created by slowly adding the remaining solution to the paste.
- The mixture was transferred into a round bottom flask and sonicated using a Hielscher UP200S ultrasonic probe for 10 minutes at a frequency of 60 Hz.

The particle size distribution was measured using DLS and was found to contain aggregates ranging in size up to 1122 nm with an average diameter of 430 nm, which have been formed from carbon spheres with a primary particle size of 30 nm. Further sonication was unable to break up the agglomerates and the dispersion proved

impossible to pass through a 1.2 μm filter. The addition of further surfactant did not result in a reduction of particle size and therefore the ink would likely result in significant nozzle clogging. The particles may need further surface treatment to overcome the attractive forces between them resulting in the formation of agglomerates. As an alternative, there are a number of carbon-based inks commercially available which can be used as an alternative.

Common fountain pen inks incorporate carbon black particles to provide long lasting durable colour. The ink has a highly uniform dispersion, is stable for several years and is made from environmentally friendly materials (mainly water). The ink has previously been applied to DSSCs fabrication and is ideally suited to wet processing methods such as spray coating and inkjet printing [261]. A fountain pen ink (Calli calligraphy ink made by Daler-Rowney in the United Kingdom) was purchased and the key fluid properties; particle size, carbon content, dynamic viscosity, surface tension, were characterised to determine printability and suitability for use in DSSCs. The average particle size was measured using DLS and found to be 146 nm as shown in Figure 5.1.

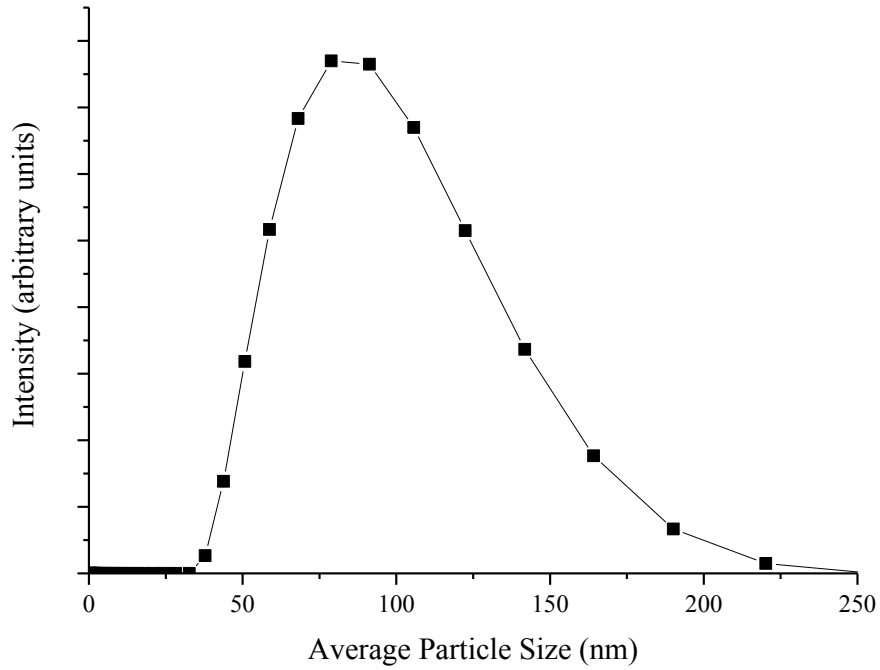

Figure 5.1 - Average particle size distribution of carbon particles in fountain pen ink

TGA was used to estimate the percentage of carbon black that is dispersed within the ink. Figure 5.2 shows the results, which indicate a very large weight loss peaking at around 165 ºC corresponding to the loss of solvent (Ic), a second significant weight loss peaks at around 230 ºC which is likely to be a polymeric component (IIc) and a third weight loss which peaks at around 425 ºC which corresponds to the burn-off of a binder material (IIIc). There was 12.7 wt% of solids left after the ink was heated to 600 ºC; the majority of this will be carbon black, with some remains of a binder material. According to the manufacturer information, the density of the ink (before modification) was 1.25 g/mL at 25 °C. The TGA confirms that there is a high percentage of carbon within the ink to enable a good deposition of material within a few print passes.

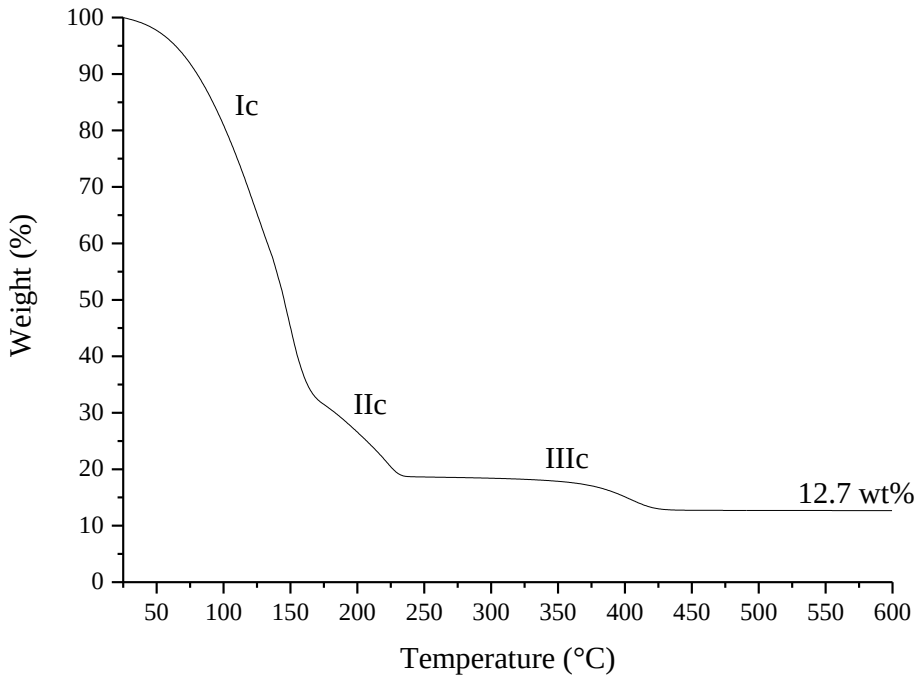

Figure 5.2 - TGA of carbon fountain pen ink

The carbon ink was further diluted with 10 wt% water (to enable the solution to be easily passed through a 1.2 µm and 0.45 µm filter) and approximately 20wt% ethylene glycol was added, which from previous work has been found to perform well as a humectant to prevent the ink from drying at the nozzles. TGA analysis found that this solution contained 10 wt% solids after heating to 600 ºC. The dynamic viscosity of the ink was measured using a Brookfield DV2T viscometer in addition to a small sample adapter with a link hanging spindle (SC4-18) using a 6 mL sample size. Measurements were taken up to the maximum measureable shear rate of 264 s^{-1} resulting in a shear rate of 10.83 cP (± 0.15) as shown in Figure 5.3.

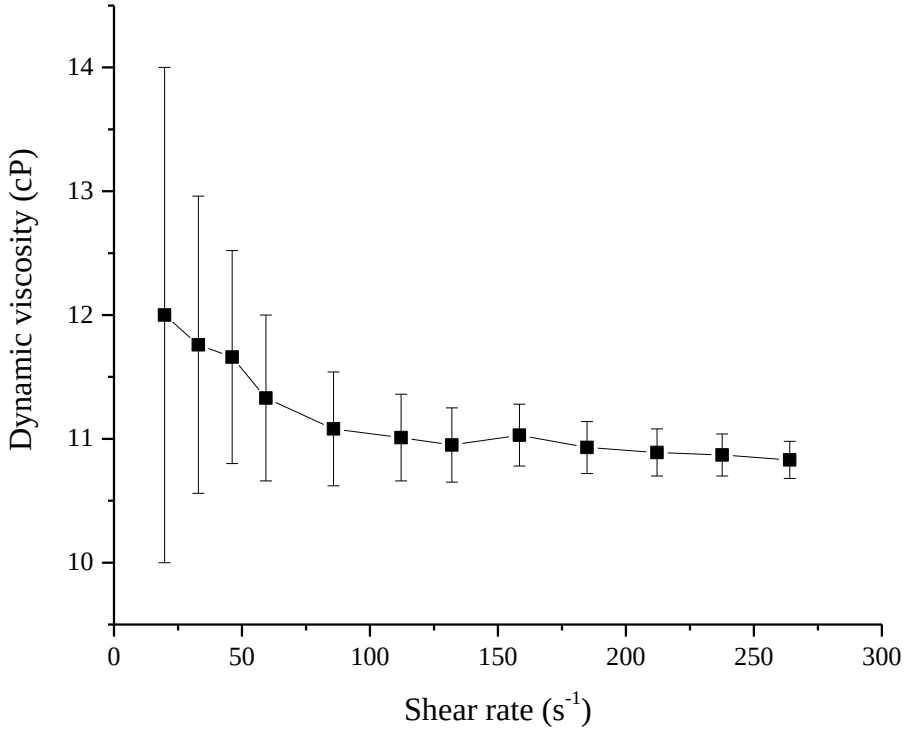

Figure 5.3 - Dynamic viscosity of carbon ink.

The surface energy was calculated using a Theta Lite optical tensiometer from Biolin Scientific as described in section 3.4.1, to determine whether the ink would wet the substrate. As a general guideline for adhesion to occur, the surface energy of the substrate should not exceed the surface tension of the fluid by more than 10-15 mN/m [221].

Table 5.1 - Average surface tension of carbon black ink

Surface tension mN/m	Volume µL
27.52	2.64
29.76	5.58
29.61	3.77

A surface free energy of the FTO coated glass was previously calculated, using the Fowkes method, to be 26.5 mN/m. Table 5.1 shows the surface tension measurements of the modified carbon ink, which was calculated to be an average of 28.96 mN/m. This resulted in an average contact angle of 25.88 ˚ on FTO glass measured 10 seconds after dispensing the drop, an example of how this was calculated is shown in Figure 5.4.

Figure 5.4 - Example contact angle measurement of carbon ink on FTO coated glass

These results indicate that the carbon ink should wet onto the FTO surface and therefore the next section details the optimisation of the print parameters to enable successful deposition of the ink.

5.1 Inkjet printing trials and optimisation of the print parameters

The carbon ink was passed through a 1.2 µm and 0.45 µm filter and loaded into a cartridge. Drop spacing was investigated as before and a drop spacing of 25 µm was selected to produce drops which overlapped on the FTO coated glass. The Drop Manager software was used alongside the dimatix model fluid waveform to monitor

drop formation from the nozzles using the built-in camera. A jetting frequency of 5 kHz, a cartridge temperature of 30 ˚C, a platen temperature of 60 ˚C and the voltage waveform was adjusted to 16 V to produce stable jetting of droplets. Each layer was printed onto the next without any further heating in-between. The films were then placed on a hot plate at 100˚C for 30 minutes followed by 250 ˚C for a further 30 minutes to remove all of the solvent material. Three thicknesses were printed to investigate the influence on the performance once the layers were incorporated within a DSSC.

The surface roughness and thickness of the printed films were characterised using a Bruker Contour GT laser profiler. The surface profile is shown in Figure 5.5. It is clear that as the number of prints increases toward 20 layers, the surface becomes rougher and the edges start to lose definition. The measured distance across the x-axis was 5.2 mm for both 5 and 15 layers, which then increased to 5.8 mm at 20 layers of printing. Sintering would be beneficial between layers to create more defined features from multiple prints.

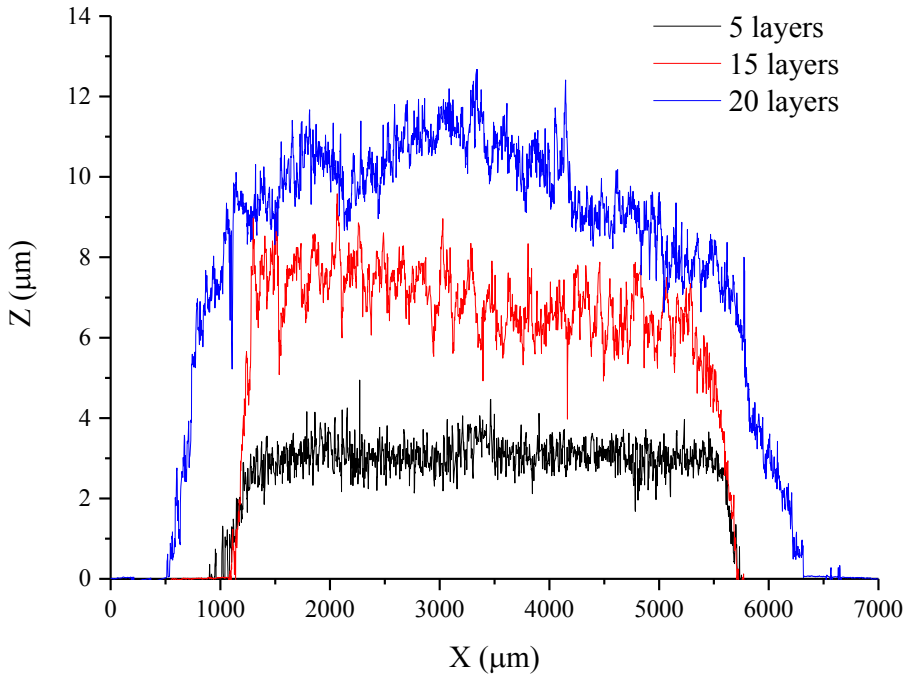

Figure 5.5 - Surface profile of the printed carbon samples

The SEM images in Figure 5.6 show that the printed film has well distributed nanoparticles, with no crack formations after annealing at 250 C. Figure 5.7 show a magnified image of the porous layer formed from the carbon ink.

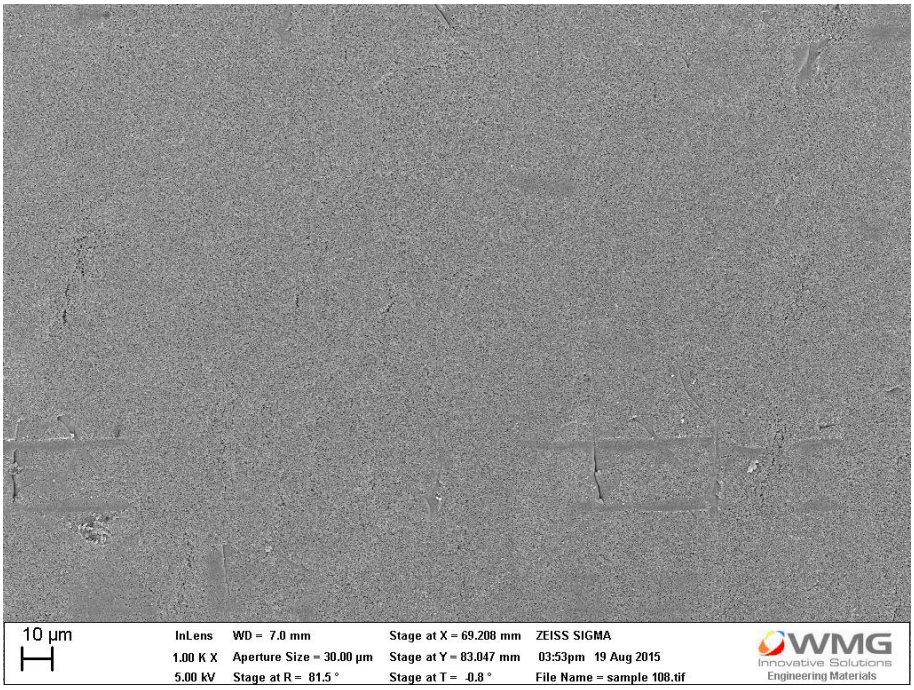

Figure 5.6 - SEM image of inkjet printed carbon onto FTO glass at low magnification

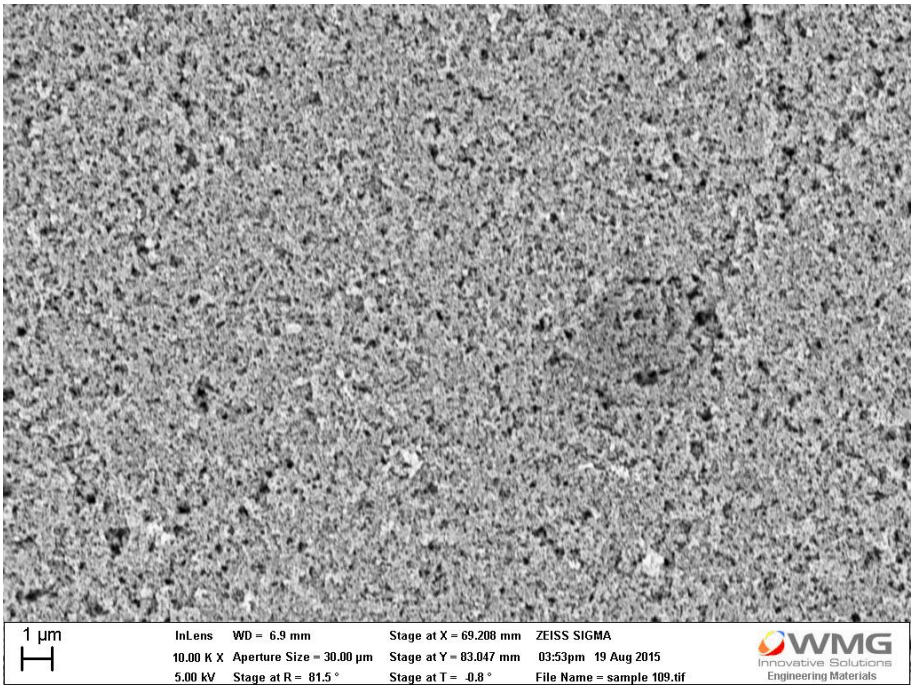

Figure 5.7 - SEM image of inkjet printed carbon onto FTO glass at high magnification

The resistance and sheet resistance was measured using a Jandel four point probe with a tip spacing of 0.5 mm. Table 5.2 shows the sheet resistance in comparison with the thickness of the carbon. The sheet resistance of the FTO coated glass substrate was also measured for comparison. According to the manufacturer it should have a sheet resistance of 8 Ω/square whereas the measured value was 7.56 Ω/square; an error of 5.5 %. As the thickness of the carbon is increased, there is a small decrease in resistance. However, to provide an accurate measurement of sheet resistance, the ink would need to be printed onto another substrate of equal surface energy to produce the same quality of coating.

Table 5.2 - Measured thickness and resistance of inkjet printed carbon

		FTO glass	**5 layers**	**15 layers**	**20 layers**
Thickness	µm	-	3.10	6.80	10.24
Resistance	Ω	1.667	1.647	1.644	1.632
Sheet resistance	Ω/square	7.56	7.46	7.45	7.40

5.2 Evaluation of performance as a counter electrode

The aim of this section is to compare the performance of the inkjet printed carbon with that of platinum with a DSSC. Firstly, the TiO_2 photoelectrodes were prepared by doctor-blading onto FTO glass (TEC8, Pilkington with a sheet resistance of 8 Ω/sq) to produce a layer 18.0 µm thick. These were then soaked in a premixed solution of 20 ml of ethanol and 2 mg of N719 dye (Ruthenizer 535-bisTBA, Solaronix) at room temperature for 24 hours in the dark and dried in air. Surlyn film (Meltonix 1170 25 series, Solaronix) was then cut to size and an iodide based low viscosity electrolyte was sandwiched between the TiO_2 coated glass and the carbon counter electrode.

Figure 5.8 shows the IV density characteristics for DSSCs made with an inkjet printed carbon electrode of varying thicknesses. The curve does not have the same smooth profile as the cell with a platinum counter electrode, which indicates there are energy losses occurring within the cell. This may be due to the fact that the resistivity of the carbon counter electrodes was significantly larger than that of the platinum counter electrodes. This high internal resistance may also be the reason for the low FF produced by the devices with carbon counter electrodes compared to the platinum devices.

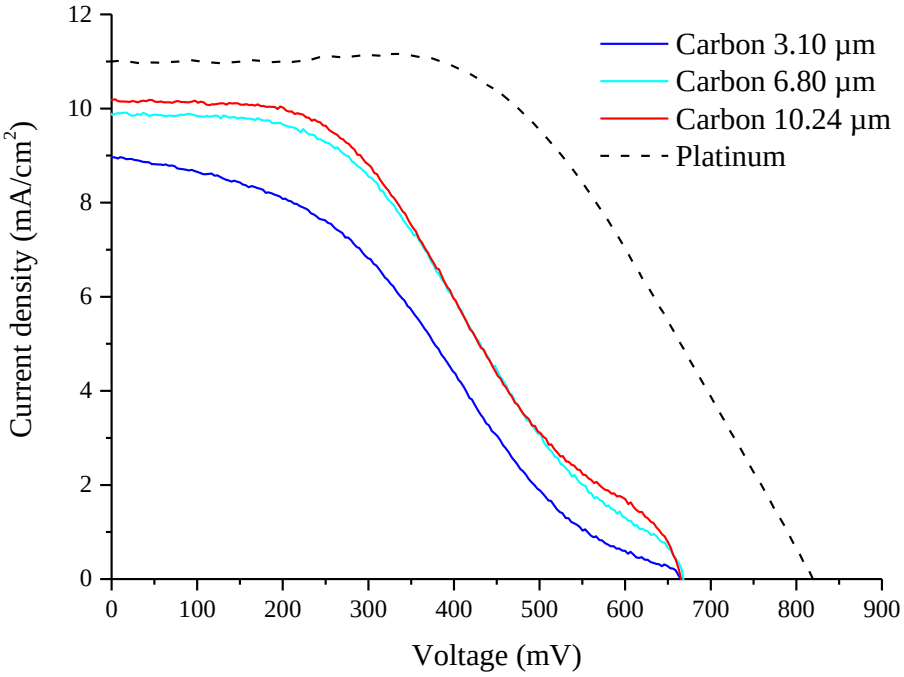

Figure 5.8 - Comparison of the IV density curves of cells with platinum and inkjet printed carbon counter electrodes

Table 5.3 presents the key parameters calculated from the IV curve. As previously mentioned, three different thicknesses were investigated to determine the influence on the performance of the DSSCs. As the thickness of the carbon layer increases, so does the open-circuit voltage (V_{oc}), short-circuit current (I_{sc}), fill factor and efficiency. However, the increase in performance between 3.10 µm to 6.80 µm is significantly larger than that between 6.80 µm to 10.24 µm, indicating that the optimal thickness is slightly higher than 10 µm. This is in agreement with the work by Murakami, T.N (2006) who investigated doctor-bladed samples and found that the cell performance improved with carbon thickness up to an approximately 15 µm, where it reached a plateau [109]. Carbon layers that are too thick result in an increase in the device's internal resistance, which has a negative effect on the fill factor (FF) and efficiency [261].

Table 5.3 - Comparative performance of DSSCs

	Inkjet printed Carbon black	Inkjet printed Carbon black	Inkjet printed Carbon black	Doctor bladed platinum benchmark
Isc [mA/cm^2]	10.09±0.02	9.66±0.33	8.94±0.04	11.12±0.05
Voc [mV]	665±2.56	659±14.94	631±8.06	756±4.90
FF	0.39±0.01	0.39±0.00	0.36±0.01	0.57±0.01
Efficiency [%]	2.59 ± 0.07	2.50 ± 0.16	2.02 ± 0.06	4.80 ± 0.04
Average thickness [µm]	10.24	6.80	3.10	18.0

In conclusion, this work shows that the counter electrode can be printed using inkjet technology. Carbon black shows promising properties as catalyst for the counter electrode of the DSSC, however the results indicate there are still areas of improvement to reduce the losses within the cells.

Chapter 6

Inkjet printed PEDOT:PSS conductive polymer as a hole-conductor for solid-state dye sensitized solar cells

6.1 Introduction

As previously discussed, traditionally DSSCs are electro-chemical cells, incorporating a liquid iodide/triiodide redox couple. However, substantial research is focussed on using gel and solid-state electrolytes to enable industrial commercialization. The key components of a ss-DSSC are the sensitizer, electron-transporting metal oxide and the molecular hole transporter. There are also several notable differences in architecture:

- Current solid state devices require a much thinner metal oxide layer (1-2 μm).
- They typically have a high work function metallic electrode such as gold or silver.
- The redox levels of the dye and p-type materials have to be adapted carefully and therefore indoline dyes (such as D102, D149 or D205) are typically used.

Conductive polymers have been successfully utilized as solid state hole transporters in DSSCs [9, 262]. This section describes the use of an Epson stylus photo P50 desktop inkjet printer to print conductive polymers. The research highlights the potential for low cost manufacturing using a household piece of equipment to produce customisable electronics.

The Epson printer can only take flexible substrates due to the design and therefore a PET film with a thickness of 100 µm was chosen. The PET was cleaned by soaking with isopropyl alcohol (IPA) to remove dirt, dust and any other contaminants. The surface energy was determined using a Theta Lite optical tensiometer from Biolin Scientific. Three drops of water, ethylene glycol and diiodomethane were dispensed onto the test piece and the Fowkes method was used to calculate the total surface energy (γ). The average surface energy of three measurements was calculated to be 46.78 mN/m, with a standard deviation of 1.23. The results are outlined in Table 6.1.

Table 6.1 - Surface energy of PET substrate

		Surface energy mN/m	**Contact angle θ [°]**	**Surface tension γtot [mN/m]**	**Dispersive interactions γd [mN/m]**	**Non-dispersive interactions γp [mN/m]**
1	Water Ethylene glycol Di-iodomethane	72.80 48.00 50.80	55.64 40.19 45.86	47.55	33.50	14.05
2	Water Ethylene glycol Di-iodomethane	72.80 48.00 50.80	60.67 47.06 42.97	45.36	34.72	10.65
3	Water Ethylene glycol Di-iodomethane	72.80 48.00 50.80	60.67 47.06 34.58	47.45	38.32	9.12

6.2 Conductive polymer ink

PEDOT:PSS solution (Orgacon IJ-1005) was purchased from Sigma Aldrich with a concentration of 0.8 wt% in water. The formulation has 1 -5 wt% ethanol and 5 -

10 wt% diethylene glycol to aid uniform coating. PEDOT:PSS is commonly doped with solvents, such as ethylene glycol (EG), glycerol, dimethyl sulfoxide (DMSO), and sorbitol to increase the conductivity [205]. This increase in conductivity has been attributed to a phase segregation of the excess PSS resulting in the formation of a three-dimensional conducting network [183]. Therefore, the PEDOT:PSS was mixed with 5 wt% DMSO for 12 hours using a magnetic stirrer to ensure homogeneity.

Although inkjet printing of PEDOT:PSS has been widely reported, the particle size of the ink was still tested to make sure that it would pass through the printer without significant loss of conductive material. Since PEDOT:PSS is a polymer rather than a rigid particle, any nozzle clogging could be more easily cleaned and therefore was not thought to cause any significant problems during printing. DLS analysis of the modified PEDOT:PSS showed that the average particle size was 246 nm, with peaks at 68 nm and 396 nm as shown in Figure 6.1.

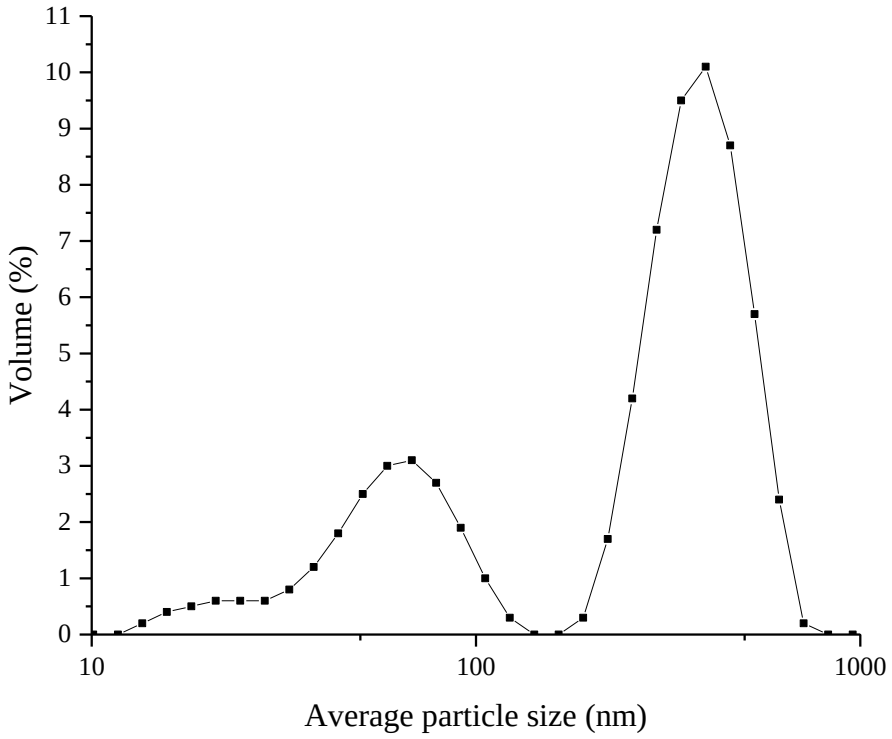

Figure 6.1 - Particle size distribution of PEDOT:PSS with 5 wt% DMSO

A Kinexus rotational rheometer from Malvern Instruments was used to measure the dynamic viscosity and rheology of the PEDOT:PSS/DMSO mixture. A shear viscosity of 8.19 cP was found at a shear rate of 264 s^{-1}, as shown in Figure 6.2. The addition of 5 wt% DMSO resulted in an increase in dynamic viscosity to 8.48 cP.

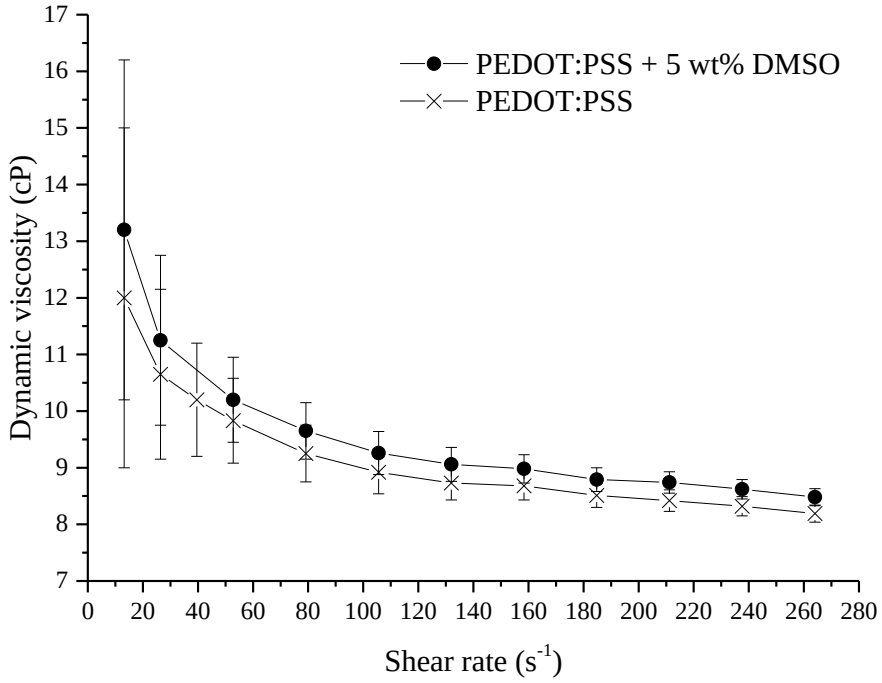

Figure 6.2 - Dynamic viscosity of PEDOT:PSS ink

The surface tension of the inks was determined using a Theta Lite optical tensiometer from Biolin Scientific. The addition of 5 wt% DMSO resulted in a drop in surface tension from 39.21 mN/m (standard deviation of 0.53) to 37.32 mN/m (standard deviation of 0.22). As previously discussed a surface tension less than 40 mN/m should enable reliable printing. As a general guideline for adhesion to occur, the surface energy of the substrate should not exceed the surface tension of the fluid by more than 10-15 mN/m [221]. The measured surface energy of the PET substrate was 46.78 mN/m (a difference of 9.46 mN/m) therefore good wetting should occur between the ink and the substrate [263].

The ink was then passed through a 0.45 µm PVDF filter and injected into an empty cartridge using a syringe. The PET was cleaned by soaking with isopropyl alcohol (IPA) to remove dirt, dust and any other contaminants. A simple square pattern with

dimensions of 20 mm x 20 mm was printed from a Bitmap image onto the PET substrate. After each layer was printed, the PET film was placed in a vacuum oven 130 ˚C for 6 minutes to remove the solvent carrier as recommended by the supplier. The process was then repeated to produce 10 layers.

6.3 Analysis of the printed films

The surface of the PET film was investigated using a Carl Zeiss optical microscope as shown in Figure 6.3. The image shows several pits (indicated by the red arrows) on the surface of the PET film. Figure 6.4 shows that after 10 layers of inkjet printed PEDOT:PSS, some of these pits are still visible (indicated by the red arrows).

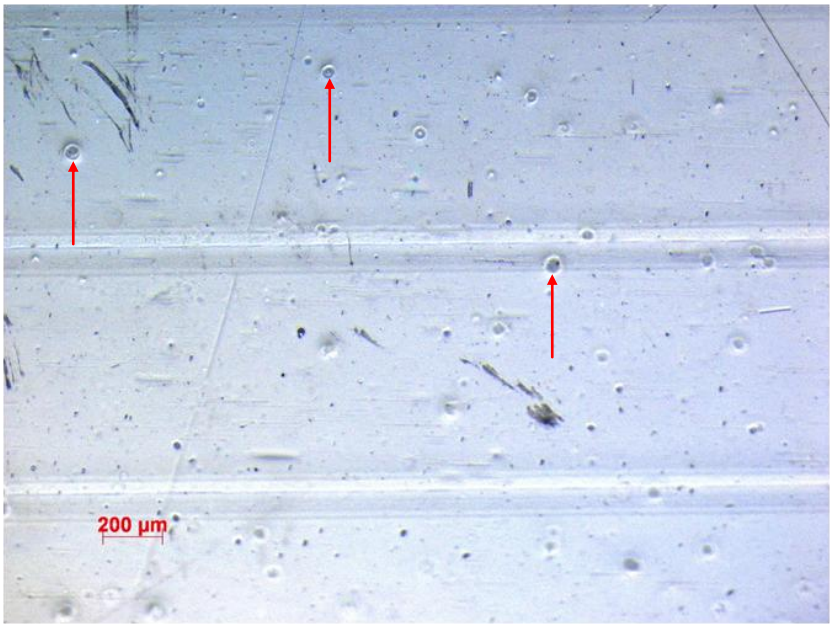

Figure 6.3 - Optical microscope image of the PET substrate

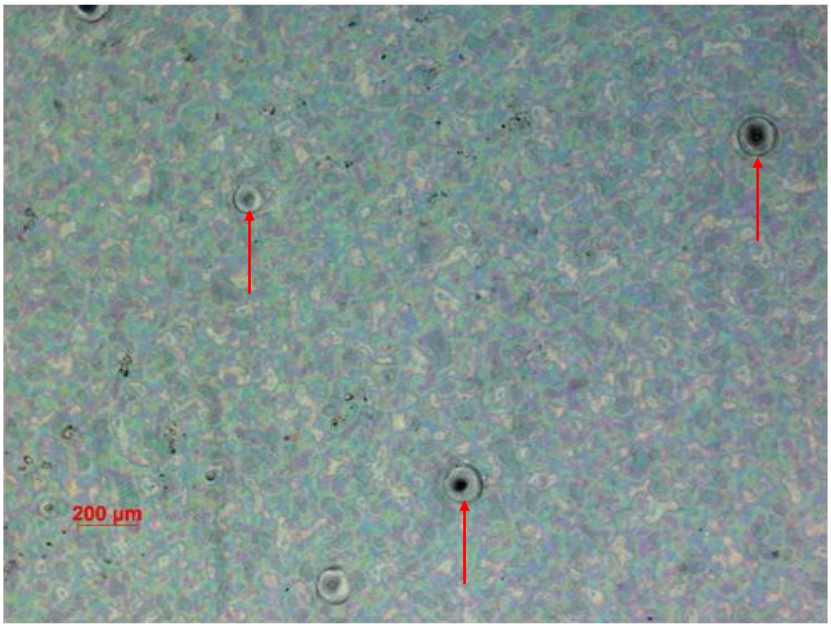

Figure 6.4 - Optical microscope image of the PET with inkjet printed PEDOT:PSS

The printed PEDOT:PSS film was analyzed in order to evaluate the thickness, transparency and conductivity. Conductivity is commonly measured using the 4-point probe method as described earlier in section 3.5.4, however due to the low conductivity of the samples a 2-point probe method was used. The resistance was measured using a Keithley multimeter at two points at a distance of 2 cm. The average resistance measured from 35 samples was found to be 0.12 MΩ.

The laser profiler failed to measure the thickness of the samples. this is due to the fact that both the PEDOT:PSS coating and the PET substrate are partially transparent, therefore the laser passed through them both without being able to differentiate between the two. The stylus was also used to measure the thickness of the samples most likely because the material was too soft. Therefore, 5 samples were selected as representatives and cut in half down the centre, sputtered with gold and the thickness was measured using SEM. A good quality image of the thickness was

obtained with correct adjustment of the image resolution as well as the brightness.The average thickness taken from 5 samples was found to be 4 µm.

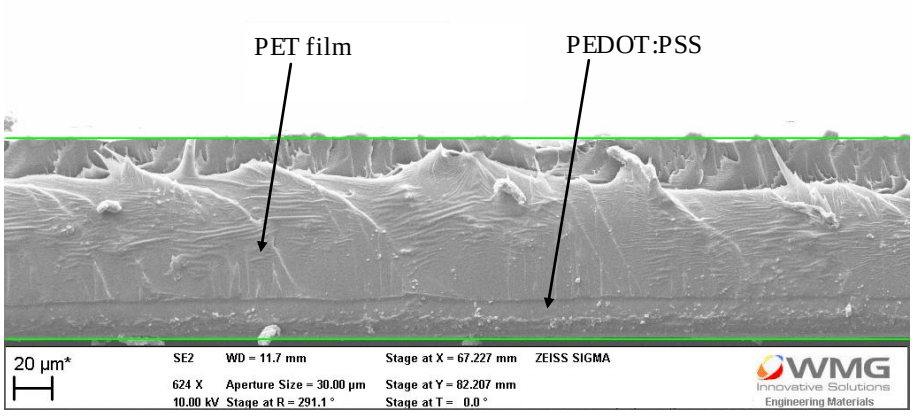

Figure 6.5 - SEM cross-sectional image of inkjet printed PEDOT:PSS

Using the previously measure resistance of 0.12 MΩ and taking the distance between the probes to be 2 cm, the equations below can be used to calculate the conductivity in the following way.

$$\rho = \frac{RA}{L}$$

$$\rho = (0.12 \times 10^{6}\Omega \times 8 \times 10^{-8}\ \mathrm{m}^2) \div 0.02\ \mathrm{m} = 0.48\ \Omega\mathrm{m} = 48\ \Omega\mathrm{cm}$$

$$\sigma = 1 / \rho = 1 / 0.48 = 2.08\ \mathrm{S/m} = 0.02\ \mathrm{S/cm}$$

These values are lower than expected, which may be due to ingress of air and moisture due to the ambient processing conditions. The use of PET as a substrate may also have compromised the performance of the printed films. A conductivity as high as 900 S/cm has been reported in the literature, using a PEDOT:PSS formulation PH1000 from H. C. Starck [63]. A similar study by S. Ummartyotin in 2011 reported a conductivity of 0.04 S/cm after 10 layers of printing to produce a thickness of 4.94 µm [264]. To determine whether the DMSO influenced the

conductivity of the PEDOT:PSS solution , 10 layers of the PEDOT:PSS without DMSO were printed. The results, shown below, indicate that the addition of DMSO improved the conductivity by over 200 times.

$$\rho = (27.08 \times 10^{6}\Omega \times 8 \times 10^{-8}\ \mathrm{m}^2) \div 0.02\ \mathrm{m} = 108.32\ \Omega\mathrm{m} = 10{,}832\ \Omega\mathrm{cm}$$

$$\sigma = \frac{1}{\rho} = \frac{1}{108.32} = 0.009\ \mathrm{S/m} = 0.00009\ \mathrm{S/cm}$$

To analyse how much visible light is transmitted through the printed PEDOT:PSS (with 5 wt% DMSO) films, the total transmittance, clarity and haze was measured using a haze meter (BYK-Gardner haze-gard plus). The results are shown in Table 6.2.

Table 6.2 - Optical measurements of inkjet printed PEDOT:PSS

	PET film	PET film + PEDOT:PSS (with 5 wt% DMSO)
Transmittance (%)	91.30	76.60
Haze (%)	1.55	3.27
Clarity (%)	98.27	93.27

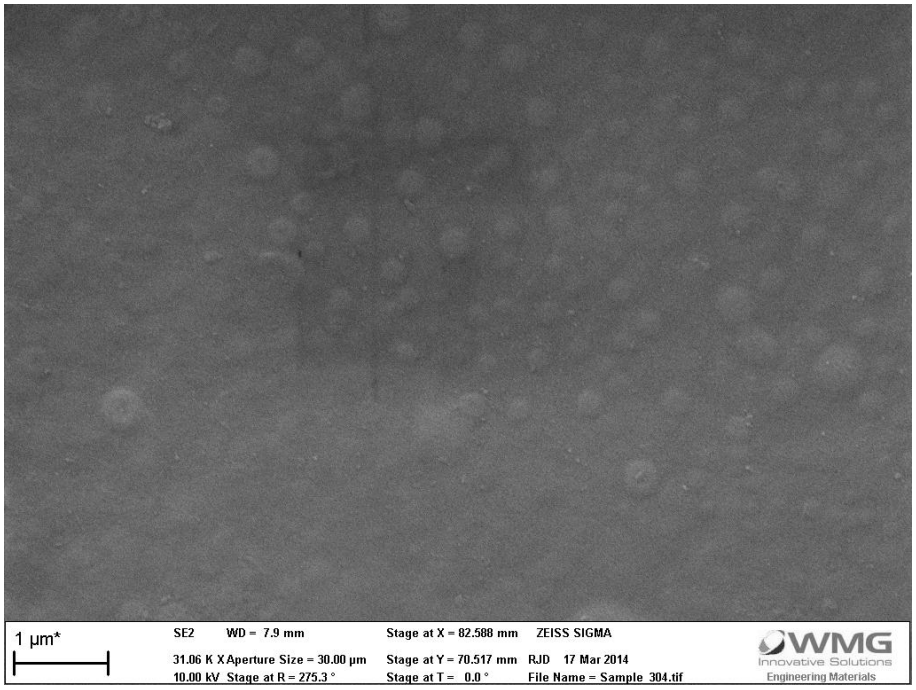

Figure 6.6 - SEM image of inkjet printed PEDOT:PSS (with 5 wt% DMSO) at low magnification

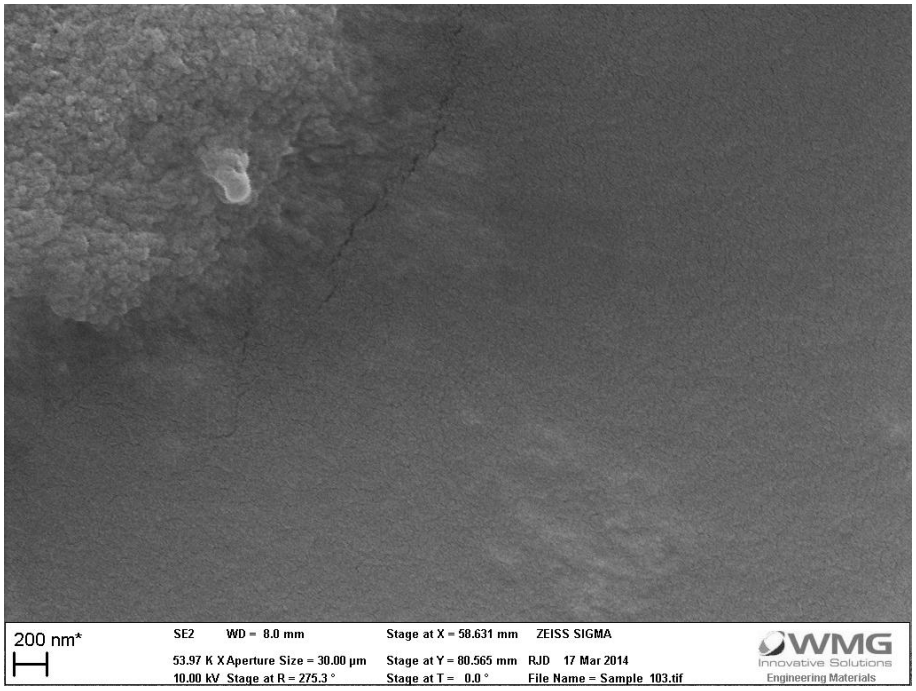

Figure 6.7 - SEM image of inkjet printed PEDOT:PSS (with 5 wt% DMSO) at high magnification

The SEM images shown in Figure 6.6 and Figure 6.7 show a good deposition of the PEDOT:PSS over the PET film. The printed films showed visibly good adhesion with the substrate. The magnified image shows the clusters of agglomerated particles. Even though the films show improved conductivity with the addition of DMSO, this may not be high enough to facilitate the transport of charge between the metal-oxide coated electrode and the counter electrode.

6.4 Characterisation of performance as a solid state hole transporter in DSSCs

This section reports on the performance of the printed conductive polymers when utilized as solid state hole transporters in DSSCs. The Epson p50 printer used in the previous section would need further modification to allow solid substrates to be used. However, to provide fair comparison with the benchmark cell (which was made using glass substrates), printing was carried out using the Fujifilm-Dimatix DMP2831 materials printer onto pre-coated glass substrates. Typically ss-DSSCs have a different structure to DSSC which incorporate a liquid redox electrolyte, to maintain consistency the same structure has been adopted as previous chapters.

The TiO_2 photoelectrodes were produced by screen printing onto FTO glass (2.2 mm thick with a sheet resistance of 7 Ω/sq) were purchased from Solaronix. TiO_2 thickness of 18.0 μm was measured using a surface profiler. These were then soaked in a premixed solution of 20 ml of ethanol and 2 mg of N719 dye (Ruthenizer 535-bisTBA, Solaronix) at room temperature for 24 hours in the dark and dried in air.

The ink was passed through a 0.45 μm PVDF filter to remove any large particulates and injected into a 1.5 ml Fujifilm-Dimatix cartridge. Printing was carried out using a model waveform at 16 V with a drop spacing of 20 μm. 10 layers of the

PEDOT:PSS ink (with 5 wt% of DMSO) was printed onto the dye soaked TiO_2 after which they were then left to dry at room temperature for 60 minutes. They were then placed on a hot plate at 130 ˚C for 60 minutes to remove the solvent carrier. A platinum coated counter electrode was placed on top of a pre-cut 60 µm thick thermoplastic sealing spacer so that the active sides of the anode and the cathode were facing each other. The glass was then heated on a hot plate to a temperature of 110 ˚C whilst applying light pressure by hand over the area of the sealing spacer for approximately 30 seconds to seal the cell together. The key performance parameters and IV density curve are shown in Table 6.3 and Figure 6.8.

Table 6.3 - Performance of DSSCs with inkjet printed PEDOT:PSS

Jsc (mA/cm^2)	Voc (mV)	FF	Efficiency (%)
0.22±0.02	589±132	0.61±0.12	0.08 ± 0.01

The solar cells showed very low Jsc values, which is an indication that one or several of the charge transfer processes in the solar cell do not work efficiently. In solid state devices, the role of the transport material is to receive holes from the oxidised dye and transport them out of the device. The conductivity is defined by how well a material can transport charge; in the case of PEDOT:PSS only holes contribute to charge transport. Highly conductive PEDOT:PSS films with a conductivity of 1000 S/cm have a hole mobility of approximately $\mu_p = 20\ cm^2/V_s$ [179]. Since the conductivity of the printed films was significantly lower than this, we can assume that the hole mobility was also significantly less, resulting in poor conversion efficiencies within the cell. However, further testing would need to be conducted to confirm this.

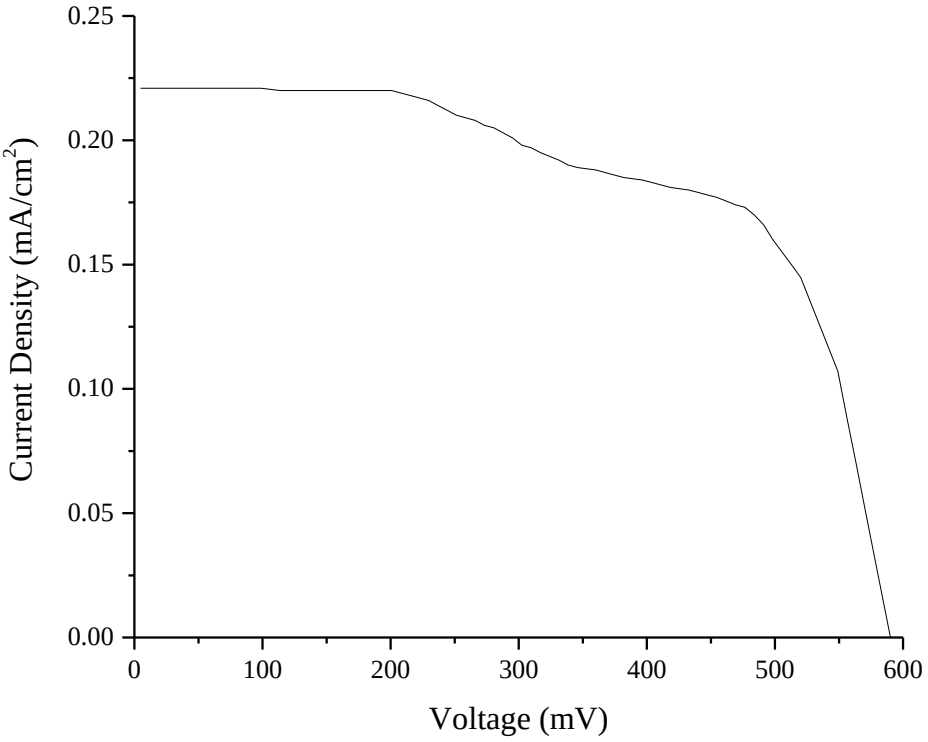

Figure 6.8 - IV density characteristics of the DSSCs incorporating inkjet printed PEDOT:PSS as a solid state hole conductor

In conclusion, the results indicate that there are still areas of improvement to utilise conductive polymers as solid state hole transporters in DSSCs . However, the work does show the potential for development of an inkjet-printable solid state hole transporter, which would ultimately lead to a fully printable DSSC.

Chapter 7

Analysis of the cost and environmental implications of inkjet printed solid state DSSCs

The potential market for DSSCs has been reported to include several indoor and outdoor applications including portable electronics, motorised blinds and rooftop systems. However, for DSSCs to become commercially viable they must have long term operational stability, be efficient, have a low environmental impact and low manufacturing cost.

Inkjet printing is an additive manufacturing process, meaning that material is only deposited where needed, minimising the material wastage. The technology can be custom-made for industrial scale roll-to-roll manufacturing or more modest desktop printing. Although the systems differ in accuracy and quality, the technology is accessible to most people and with the development of functional inks could enable the manufacture of electronic components within the home or in more remote areas. One of the advantages of inkjet printing is that it can be operated under ambient conditions. Although the contamination of materials should be avoided to prevent a negative impact on the performance of the device, only moderate control of atmospheric dust and moisture is required and therefore high cost cleanroom facilities should not be required for the manufacture of DSSCs [60, 265].

After the initial capital costs there are three key costs associated with the manufacture of DSSCs; processing costs, labour costs and materials. For large roll-to-roll manufacturing of DSSCs, all processing steps should be designed for moderate to high line speeds (2 to 20 m/min) to obtain maximum production yield

[32, 60]. Inkjet printers are capable of printing at the speeds required for producing roll-to-roll electronic devices, with commercial speeds up to 244 m/min from 1200 dpi (dots per inch) as standard [207]. High speed printing (18m/min) of TiO_2 for DSSCs applications has been also been reported [266]. Additionally, two significant challenges that have recently been overcome have been achieved through firstly the use of infra-red radiation to sinter the TiO_2 printed layers within 12 seconds and secondly the reduction of the dyeing process to within minutes through ultra-fast dye sensitisation [17, 267]. At this scale the majority of coating and printing processes are automated, it can also be assumed that the labour costs will be minimal. The production of the technology is therefore dominated by the material costs. A reduction in the material costs can be achieved by minimizing material wastage and replacing or reducing the amount of high-cost components within a device.

The carrier solvent is usually the largest constituent within an inkjet ink and therefore has significant environmental and cost implications. Solvents are an integral part of any manufacturing and processing industry, with almost 15 billion kilograms of organic and halogenated solvents produced worldwide each year [268]. Recently there have been concerns about the release of toxins into the environment and therefore several industries have eliminated solvents from key process steps to reduce the environmental impact [268]. The use of water in applications such as coatings is preferable to organic solvents. For these reasons, although other solvents were initially considered, the inks in this work were formulated using water as the main solvent.

There are a wide range of materials reported in the literature for use within DSSCs, often evaluated individually rather than holistically as part of a cell. As previously discussed, solid-state devices have been identified by many researchers as the most

likely route to large scale production of DSSCs [60]. Optimisation of the electrolyte will enable the long term stability of devices. Solid state devices also require much thinner metal oxide layers, which will reduce the cost associated with the manufacture of the TiO_2 layer [15, 103, 104]. The main factors that limit the efficiency of solid-state devices are similar to that encountered with devices that incorporate a liquid electrolyte. However, the main reason why solid-state devices may result in low efficiencies is due to low conductivity within the hole transport material (HTM), resulting in a higher resistance which impedes the flow of charge. The highest efficiencies have been achieved by using spiro-MeOTAD as the hole conductor [1]. However, spiro-OMeTAD, has a commercial price that is more than 10 times that of gold and platinum [102]. Hole conducting polymers can also be used to replace the volatile, toxic electrolyte currently used within liquid DSSCs. Conducting polymers have a significantly lower commercial price and also benefit from being dispersable in water, which has low volatility and is non-toxic. PEDOT:PSS conducting polymer was inkjet printed and incorporated into a DSSC, showing the potential for development of an inkjet-printable solid state hole transporter. The most efficient solid-state DSSCs contain a metal counter electrode deposited by vacuum co-evaporation of the elements [1]. The cost of owning large area vacuum evaporation technology is high and therefore to minimize the manufacturing cost of solid-state DSSC, the use of such equipment to should be avoided.

Platinum is still the most efficient and widely used counter electrode in DSSCs, with a reported cost of 32,000-70,000 $/kg [60]. Although it is a high-value component, due to the small amount currently required to produce a photo catalytic layer, it is not the most expensive component within a DSSC. However, platinum is a rare metal

with rising demand from a number of industries, most notibly the automotive industry [269]. This is likely to impact the future price and availability of platinum. Concerns over platinum's cost and stability have led to a research investigating alternative catalysts [107, 108]. Carbon-based materials (e.g. carbon black, carbon nanotubes, graphite, graphene and graphene oxide) are low cost and widely available, which show promising potential as a replacement to platinum as counter electrodes in DSSCs [109, 110]. This work investigated the development and printing of an aqueous carbon black nanoparticle ink for use as a counter electrode. It showed that inkjet printing can be used to manufacture a platinum-free coating, demonstrating the exciting potential of additive printing to produce one of the key components within a DSSC.

Silicon solar panels are manufactured from a number of batch processing steps that are both time consuming and costly. The majority of silicon panels are produced onto inexpensive soda-lime glass, however glass with low iron content has a higher transmittance and therefore achieves higher efficiencies [270]. Solution processing methods, such as inkjet, allow for roll-to-roll processing to be used. The processing costs are thought to have significant cost reduction in terms of ease of manufacture and transportation of lightweight panels. Inexpensive polymeric substrates such as polyethylene terephthalate (PET) could provide a cost effective alternative to glass. Thermal analysis of the PET film shows that the glass transition temperature (T_g) occurred at approximately 58 ˚C and is reported to have an upper processing temperature of 150 ˚C [197]. The polyimide showed much better thermal stability, however the high cost of the film may limit its application to the production of DSSCs. Although the production of plastic films are more costly and energy

intensive, the overall energy consumption is considerably reduced due to savings in transportation costs [271].

In summary, there are several materials within a traditional DSSC that can be replaced to minimise the cost and environmental impact of the device. The work has also demonstrated the exciting potential of additive printing to produce devices with minimal wastage and processing costs. The next section will continue by summarising the key findings from the results along with areas identified for further work.

Chapter 8

Conclusions

The aim of this research project was to further develop the scientific knowledge of functional inks for printing DSSC devices using inkjet techniques. A literature review was performed to understand the materials required in the manufacture of DSSCs, the inkjet technology and the requirements for functional inks. Following the literature review several research opportunities were identified. These centre on gaps in the knowledge required to develop suitable inks for liquid processing and optimisation of the print parameters for a high-quality deposition of material.

During initial trials, inkjet printing was used to produce several layers within a DSSC to establish the capability of the technique to produce a printed device. This demonstrates the use of additive techniques to manufacture complex electronic devices. To examine the potential and performance of such materials in a fully printed DSSC, demonstrator devices were manufactured and evaluated.

The perceived scientific contribution of this work is the development of novel inks that are compatible both with the inkjet process and for use within a DSSC. The complexity and time-consuming nature of ink development is often over-looked in reports on inkjet printing of functional materials. It requires the selection of suitable materials, dispersion within a fluid and the investigation of suitable additives to enable printing. Nanoparticles can be introduced into inks to incorporate functionality within a printed layer. Any particles within an ink must be less than 100 times smaller than the nozzles size; therefore detailed characterisation of particle size using several techniques was undertaken.

This work has shown that the (as received) Degussa Aeroxide P25 TiO_2 nanoparticles are highly agglomerated, and the particle size depends strongly on the degree of dispersion carried out prior to measurement. XRD analysis determined that the phase composition is a mixture of anatase (71 %) and rutile (29 %). The angular width of the peak at half maximum height was measured from the XRD spectra and subsequently the crystal size was calculated to be 23 nm. From SEM analysis it was seen that the particle size of the powder (as received) ranges significantly with small primary particles and larger agglomerates and aggregates (>5 μm) which have formed over time. DLS analysis of the nanoparticles in water also showed a large spread or particle sizes with peaks at 1281 nm (indicating the formation of agglomerates) and 5560 nm (indicating the formation of aggregates). Ultrasonic processing de-agglomerated the nanoparticles to give a reasonably fine size distribution, with a reduction in the average particle size of 380 nm after 10 minutes. Modification of the solution pH provided further stabilisation of the nanoparticle suspensions and the addition of polymeric dispersants reduced the average particle size further to 80 nm.

From the literature review, carbon black was identified as a widely available, low-cost alternative to platinum for use as the counter electrode. An aqueous dispersion was purchased and DLS analysis determined an average particle size of 146 nm, suitably small enough for printing. The first printing trials demonstrated the necessity of adding humectant into the ink formulations, to prevent the ink drying and blocking the surface of the nozzles. PEG with a molecular weight of 400 was added at 25 wt% as the humectant. The surface tension and dynamic viscosity of each ink was evaluated to ensure that they met the fluid constraints of the inkjet printing process. In conclusion, carbon black shows promising properties as a

catalyst for the counter electrode of the DSSC, however further carbon-based materials should be investigated for their potential to produce better results. The results indicate there are still areas of improvement to reduce the electrical losses within the cells. The work also shows that the counter electrode can be printed using inkjet technology.

With all three of the materials investigated (TiO_2, carbon black and PEDOT:PSS), previous research has shown that the thickness has a major bearing on the functionality. The optimal thickness for TiO_2 within conventional DSSCs has previously been reported in the literature to be between 9.5 µm and 20 µm. Multiple layers were printed to increase the thickness of the deposited material, however cracking and peeling was observed upon drying of the printed films. The addition of cellulose binders was investigated to enhance the binder strength, increase the thickness of the printed layers and prevent the formation of cracks during drying. Analysis of the surface quality of the printed films under optical microscope found that the films suffered an uneven topography due to solid migration during drying. Likewise with carbon, multiple layers were printed to produce three thicknesses (3.10 µm, 6.80 µm and 10.24 µm). As the printed thickness was increased, the surface appeared rougher and the edges were less defined. However, increased thickness resulted in lower sheet resistance and subsequently higher conversion efficiencies when incorporated as a counter electrode in cells.

Solid state devices, which replace the liquid electrolyte with a solid hole transport material are seen as the most likely route to large scale production. They require much thinner metal oxide layers (less than 2 µm) and would therefore be more suited to inkjet manufacturing due to the thin layers which it is able to deposit. Solid-state devices which use PEDOT as a hole conductor have been previously investigated in

the literature and inkjet printing of PEDOT:PSS has also been widely reported. However, the use of inkjet printing to deposit PEDOT:PSS as a hole conductor in solid-state DSSCs is unreported. A 0.8 wt% solution of PEDOT:PSS in water (formulated with ethanol and diethylene glycol) was purchased and modified with the addition of 5 wt% DMSO. A desktop piezoelectric printer was used to print 10 layers of the ink solution onto PET to produce a layer 4 μm thick when dry. The addition of DMSO was found to improve the conductivity of the printed film by more than 200 times. However, this was still significantly less than the value of 1000 S/cm previously reported in the literature. Since the conductivity of the printed films was significantly lower than this, it was assumed that the hole mobility will also be negatively affected. However, characterising the films in this way provides further understanding on the performance of the material so that more suitable hole transport polymers can be selected if required in the development of future DSSC devices.

Demonstrator devices were manufactured based on the research outcomes. The functionality of the printed devices was shown to be entirely dependent on careful ink formulation and optimization of the print parameters, which highlighted the difficulty of inkjet manufacturing. The devices were characterised directly after fabrication to minimize the effect of degradation caused by water and oxygen in the air. Four key electrical performance parameters (Jsc, Voc, FF and efficiency) were used to characterize and compare the cells produced. Each layer was printed separately to determine the influence of each on the performance of the cell.

An initial aqueous titanium dioxide nanoparticle dispersion was formulated and two layers were printed to produce a layer 2.6 μm thick. Once integrated into a cell, this

resulted in an efficiency of 3.50 %. In an effort to improve the performance, a HEC binder was incorporated to increase the layer thickness. Although the thickness and adhesion were improved, the printed layers resulted in reduced DSSC efficiency. From TGA analysis it was seen that a significant amount of the HEC binder residue (~25 wt %) remained after heating to 450 ºC. This could have led to poor dye absorption on the surface of the TiO_2 particles leading to reduced performance. Further testing to observe the dye absorption and desorption would need to be performed to confirm this.

Of the DSSCs tested with carbon black counter electrodes, those with a layer thickness of 10.24 µm resulted in the highest efficiency of 2.59 %. These devices had an average FF of 0.39 compared with an average of 0.57 from the devices made with platinum counter electrodes. This indicates a high amount of electrical energy losses within the cell, most likely due to high internal resistance. Electrochemical analysis would provide further information on the interfacial properties and may help to identify ways in which the efficiencies of the cells can be improved to match the values of more than 7% reported in the literature for traditionally manufactured DSSCs.

The performance of the devices incorporating PEDOT:PSS as a hole conductor in solid-state DSSCs was also tested. The efficiencies of these devices were poor and further work is needed to find an alternative formulation which is better as a hole conductor or investigate the use of alternative solid state HTMs. The work does show the potential for development of an inkjet-printable solid state hole transporter, which would ultimately lead to a fully printable DSSC.

This work has identified exciting potential for the use of inkjet technology in the manufacture of DSSCs. Further work is required to unlock the potential and alternative materials should be considered to further improve the conversion efficiencies. Some suggestions which have been gathered from the literature are provided in the next section.

8.1 Recommendations for future work

This project has made a significant step forward by showing how inkjet technology can be used to manufacture DSSCs; however there are many ways in which this work can be further extended to take the technology closer to market. In order to improve the poor fill factors (FF) of the devices reported in this work, post-treatment of the porous TiO_2 anodes with zirconium oxide (ZrO_2) would prevent charge recombination thus enhancing the efficiency of the cells [82]. There are also many nanomaterials that could be investigated to replace the traditional ones.

Although FTO/ITO replacements were not used within this work, several nanomaterial solutions were identified which could provide similar performance. Silver nanowires, graphene and single walled carbon nanotubes have produced promising results and appear to be the best candidates so far [65-68]. For these materials to succeed, they need to be specially formulated to be used as a coating. The stability of the inks is vital to provide repeatability and reliability of the print and therefore further work is required to establish the industrial viability of the inks. Improving the performance of the printed devices would further demonstrate the commercial potential of the process.

References

1. Docampo, P., S. Guldin, T. Leijtens, N.K. Noel, U. Steiner, and H.J. Snaith, *Lessons Learned: From Dye-Sensitized Solar Cells to All-Solid-State Hybrid Devices.* Advanced Materials, 2014. **26**(24): p. 4013.
2. Cummins, G. and M.P. Desmulliez, *Inkjet printing of conductive materials: a review.* Circuit World, 2012. **38**(4): p. 193.
3. Krebs, F.C., *Fabrication and processing of polymer solar cells: A review of printing and coating techniques.* Solar Energy Materials and Solar Cells, 2009. **93**(4): p. 394.
4. Adachi, M., Y. Murata, J. Takao, J. Jiu, M. Sakamoto, and F. Wang, *Highly Efficient Dye-Sensitized Solar Cells with a Titania Thin-Film Electrode Composed of a Network Structure of Single-Crystal-like TiO2 Nanowires Made by the "Oriented Attachment" Mechanism.* Journal of the American Chemical Society, 2004. **126**(45): p. 14943.
5. Law, M., L.E. Greene, A. Radenovic, T. Kuykendall, J. Liphardt, and P. Yang, *ZnO−Al2O3 and ZnO−TiO2 Core−Shell Nanowire Dye-Sensitized Solar Cells.* The Journal of Physical Chemistry B, 2006. **110**(45): p. 22652.
6. Qi, J., X. Dang, P.T. Hammond, and A.M. Belcher, *Highly Efficient Plasmon-Enhanced Dye-Sensitized Solar Cells through Metal@Oxide Core–Shell Nanostructure.* ACS Nano, 2011. **5**(9): p. 7108.
7. de Jong, J., R. Jeurissen, H. Borel, M. van den Berg, H. Wijshoff, H. Reinten, M. Versluis, A. Prosperetti, and D. Lohse, *Entrapped air bubbles in piezo-driven inkjet printing: Their effect on the droplet velocity.* Physics of Fluids, 2006. **18**(12): p. 121511.

8. Ding, I.K., J. Melas-Kyriazi, N.-L. Cevey-Ha, K.G. Chittibabu, S.M. Zakeeruddin, M. Grätzel, and M.D. McGehee, *Deposition of hole-transport materials in solid-state dye-sensitized solar cells by doctor-blading.* Organic Electronics, 2010. **11**(7): p. 1217.

9. Kim, J., J.K. Koh, B. Kim, S.H. Ahn, H. Ahn, D.Y. Ryu, J.H. Kim, and E. Kim, *Enhanced Performance of I2-Free Solid-State Dye-Sensitized Solar Cells with Conductive Polymer up to 6.8%.* Advanced Functional Materials, 2011. **21**(24): p. 4633.

10. Li, B., L. Wang, B. Kang, P. Wang, and Y. Qiu, *Review of recent progress in solid-state dye-sensitized solar cells.* Solar Energy Materials and Solar Cells, 2006. **90**(5): p. 549.

11. Liu, Q., C. Li, K. Jiang, Y. Song, and J. Pei, *A high-efficiency solid-state dye-sensitized solar cell with P3HT polymer as a hole conductor and an assistant sensitizer.* Particuology, 2013(0).

12. Matteocci, F., G. Mincuzzi, F. Giordano, A. Capasso, E. Artuso, C. Barolo, G. Viscardi, T.M. Brown, A. Reale, and A. Di Carlo, *Blocking layer optimisation of poly(3-hexylthiopene) based Solid State Dye Sensitized Solar Cells.* Organic Electronics, 2013. **14**(7): p. 1882.

13. Wahlström, N., *Conductive polymers as hole conductors for solid state dye sensitized solar cells*. 2014, Uppsala University. p. 70.

14. Xue, Z., C. Jiang, L. Wang, W. Liu, and B. Liu, *Fabrication of Flexible Plastic Solid-State Dye-Sensitized Solar Cells Using Low Temperature Techniques.* The Journal of Physical Chemistry C, 2013.

15. Yang, L., U.B. Cappel, E.L. Unger, M. Karlsson, K.M. Karlsson, E. Gabrielsson, L. Sun, G. Boschloo, A. Hagfeldt, and E.M.J. Johansson, *Comparing spiro-OMeTAD*

and P3HT hole conductors in efficient solid state dye-sensitized solar cells. Physical Chemistry Chemical Physics, 2012. **14**(2): p. 779.

16. Zhang, W., R. Zhu, F. Li, Q. Wang, and B. Liu, *High-Performance Solid-State Organic Dye Sensitized Solar Cells with P3HT as Hole Transporter.* The Journal of Physical Chemistry C, 2011. **115**(14): p. 7038.
17. Watson, T., I. Mabbett, H. Wang, L. Peter, and D. Worsley, *Ultrafast near infrared sintering of TiO2 layers on metal substrates for dye-sensitized solar cells.* Progress in Photovoltaics: Research and Applications, 2011. **19**(4): p. 482.
18. Galagan, Y., D.J.D. Moet, D.C. Hermes, P.W.M. Blom, and R. Andriessen, *Large area ITO-free organic solar cells on steel substrate.* Organic Electronics, 2012. **13**(12): p. 3310.
19. Tebby, Z., O. Babot, D. Michau, L. Hirsch, L. Carlos, and T. Toupance, *A simple route towards low-temperature processing of nanoporous thin films using UV-irradiation: Application for dye solar cells.* Journal of Photochemistry and Photobiology A: Chemistry, 2009. **205**(1): p. 70.
20. Tobjörk, D., H. Aarnio, P. Pulkkinen, R. Bollström, A. Määttänen, P. Ihalainen, T. Mäkelä, J. Peltonen, M. Toivakka, H. Tenhu, and R. Österbacka, *IR-sintering of ink-jet printed metal-nanoparticles on paper.* Thin Solid Films, 2012. **520**(7): p. 2949.
21. Cruz, R., D.A. Pacheco Tanaka, and A. Mendes, *Reduced graphene oxide films as transparent counter-electrodes for dye-sensitized solar cells.* Solar Energy, 2012. **86**(2): p. 716.
22. Margulis, G.Y., M.G. Christoforo, D. Lam, Z.M. Beiley, A.R. Bowring, C.D. Bailie, A. Salleo, and M.D. McGehee, *Spray Deposition of Silver Nanowire Electrodes for Semitransparent Solid-State Dye-Sensitized Solar Cells.* Advanced Energy Materials, 2013. **3**(12): p. 1657.

23. Gemeiner, P. and M. Mikula, *Efficiency of dye sensitized solar cells with various compositions of TiO2 based screen printed photoactive electrodes.* Acta Chimica Slovaca, 2013. **6**(1): p. 29.

24. Hwang, M.-s., B.-y. Jeong, J. Moon, S.-K. Chun, and J. Kim, *Inkjet-printing of indium tin oxide (ITO) films for transparent conducting electrodes.* Materials Science and Engineering: B, 2011. **176**(14): p. 1128.

25. Lin, L.-Y., C.-P. Lee, K.-W. Tsai, M.-H. Yeh, C.-Y. Chen, R. Vittal, C.-G. Wu, and K.-C. Ho, *Low-temperature flexible Ti/TiO2 photoanode for dye-sensitized solar cells with binder-free TiO2 paste.* Progress in Photovoltaics: Research and Applications, 2012. **20**(2): p. 181.

26. Gong, J., J. Liang, and K. Sumathy, *Review on dye-sensitized solar cells (DSSCs): Fundamental concepts and novel materials.* Renewable and Sustainable Energy Reviews, 2012. **16**(8): p. 5848.

27. Bosch-Jimenez, P., Y. Yu, M. Lira-Cantu, C. Domingo, and J.A. Ayllón, *Solution processable titanium dioxide precursor and nanoparticulated ink: Application in Dye Sensitized Solar Cells.* Journal of Colloid and Interface Science, 2014. **416**(1): p. 112.

28. Jose, R., V. Thavasi, and S. Ramakrishna, *Metal Oxides for Dye-Sensitized Solar Cells.* Journal of the American Ceramic Society, 2009. **92**(2): p. 289.

29. Lee, K.E., C. Charbonneau, and G.P. Demopoulos, *Thin single screen-printed bifunctional titania layer photoanodes for high performing DSSCs via a novel hybrid paste formulation and process.* Journal of Materials Research, 2013. **28**(03): p. 480.

30. Oh, Y., H.G. Yoon, S.-N. Lee, H.-K. Kim, and J. Kim, *Inkjet-Printing of TiO2 Co-Solvent Ink: From Uniform Ink-Droplet to TiO2 Photoelectrode for Dye-Sensitized Solar Cells.* Journal of the Electrochemical Society, 2011. **159**(1): p. B34.

31. Senthilarasu, S., T.A.N. Peiris, J. García-Cañadas, and K.G.U. Wijayantha, *Preparation of Nanocrystalline TiO2 Electrodes for Flexible Dye-Sensitized Solar Cells: Influence of Mechanical Compression.* The Journal of Physical Chemistry C, 2012. **116**(36): p. 19053.

32. Holliman, P.J., D.K. Muslem, E.W. Jones, A. Connell, M.L. Davies, C. Charbonneau, M.J. Carnie, and D.A. Worsley, *Low temperature sintering of binder-containing TiO2/metal peroxide pastes for dye-sensitized solar cells.* Journal of Materials Chemistry A, 2014. **2**(29): p. 11134.

33. Yamaguchi, T., N. Tobe, D. Matsumoto, and H. Arakawa, *Highly efficient plastic substrate dye-sensitized solar cells using a compression method for preparation of TiO2 photoelectrodes.* Chemical Communications, 2007(45): p. 4767.

34. Halme, J., J. Saarinen, and P. Lund, *Spray deposition and compression of TiO2 nanoparticle films for dye-sensitized solar cells on plastic substrates.* Solar Energy Materials and Solar Cells, 2006. **90**(7–8): p. 887.

35. Burschka, J., N. Pellet, S.-J. Moon, R. Humphry-Baker, P. Gao, M.K. Nazeeruddin, and M. Gratzel, *Sequential deposition as a route to high-performance perovskite-sensitized solar cells.* Nature, 2013. **499**(7458): p. 316.

36. Nelson, J., *The Physics of Solar Cells*. 2003: Imperial College Press.

37. Mariani, G., Y. Wang, R.B. Kaner, and D.L. Huffaker, *Hybrid Solar Cells: Materials, Interfaces, and Devices*, in *High-Efficiency Solar Cells. Physics, Materials, and Devices*, X. Wang and Z.M. Wang, Editors. 2014, Springer Series in Materials Science. p. 357.

38. Okuwada, H.K.a.K., *Development Trend for High Purity Silicon Raw Material Technologies* in *Science and Technology Trends*. 2007. p. 38.

39. Green, M.A., K. Emery, Y. Hishikawa, W. Warta, and E.D. Dunlop, *Solar cell efficiency tables (version 39).* Progress in Photovoltaics: Research and Applications, 2012. **20**(1): p. 12.

40. Green, R., A. Morfa, A.J. Ferguson, N. Kopidakis, G. Rumbles, and S.E. Shaheen, *Performance of bulk heterojunction photovoltaic devices prepared by airbrush spray deposition.* Applied Physics Letters, 2008. **92**(3): p. 033301.

41. Chung, S.J., J.P. Leonard, I. Nettleship, J.K. Lee, Y. Soong, D.V. Martello, and M.K. Chyu, *Characterization of ZnO nanoparticle suspension in water: Effectiveness of ultrasonic dispersion.* Powder Technology, 2009. **194**(1–2): p. 75.

42. Ward, J.S., K. Ramanathan, F.S. Hasoon, T.J. Coutts, J. Keane, M.A. Contreras, T. Moriarty, and R. Noufi, *A 21.5% efficient Cu(In,Ga)Se2 thin-film concentrator solar cell.* Progress in Photovoltaics: Research and Applications, 2002. **10**(1): p. 41.

43. Avrutin, V., N. Izyumskaya, and H. Morkoç, *Semiconductor solar cells: Recent progress in terrestrial applications.* Superlattices and Microstructures, 2011. **49**(4): p. 337.

44. Eyderman, S., A. Deinega, and S. John, *Near perfect solar absorption in ultra-thin-film GaAs photonic crystals.* Journal of Materials Chemistry A, 2014. **2**(3): p. 761.

45. Anil Kumar, R., M.S. Suresh, and J. Nagaraju, *Measurement and comparison of AC parameters of silicon (BSR and BSFR) and gallium arsenide (GaAs/Ge) solar cells used in space applications.* Solar Energy Materials and Solar Cells, 2000. **60**(2): p. 155.

46. Fraas, L., J. Avery, V.S. Sundaram, V.T. Dinh, T.M. Davenport, J.W. Yerkes, J. Gee, and K. Emery. *Over 35% efficient GaAs/GaSb stacked concentrator cell assemblies for terrestrial applications*. in *Photovoltaic Specialists Conference, 1990., Conference Record of the Twenty First IEEE*. 1990.

47. Green, M.A., K. Emery, Y. Hishikawa, W. Warta, and E.D. Dunlop, *Solar cell efficiency tables (version 46).* Progress in Photovoltaics: Research and Applications, 2015. **23**(7): p. 805.

48. Meijer, A., M.A.J. Huijbregts, J.J. Schermer, and L. Reijnders, *Life-cycle assessment of photovoltaic modules: Comparison of mc-Si, InGaP and InGaP/mc-Si solar modules.* Progress in Photovoltaics: Research and Applications, 2003. **11**(4): p. 275.

49. McCandless, B.E. and J.R. Sites, *Cadmium telluride solar cells.* Handbook of Photovoltaic Science and Engineering, 2003. **2**.

50. Bouroushian, M., *Electrochemistry of Metal Chalcogenides*. 2010: Springer.

51. Brabec, C.J., N.S. Sariciftci, and J.C. Hummelen, *Plastic solar cells.* Advanced Functional Materials, 2001. **11**(1): p. 15.

52. Reddy, P.J., *Solar Power Generation: Technology, New Concepts & Policy*. 2012: Taylor & Francis.

53. Yu, G., J. Gao, J.C. Hummelen, F. Wudl, and A.J. Heeger, *Polymer Photovoltaic Cells: Enhanced Efficiencies via a Network of Internal Donor-Acceptor Heterojunctions.* Science, 1995. **270**(5243).

54. Krebs, F.C., *Polymeric Solar Cells: Materials, Design, Manufacture*. 2010: DEStech Publications, Inc.

55. Dang, M.T., L. Hirsch, and G. Wantz, *P3HT:PCBM, Best Seller in Polymer Photovoltaic Research.* Advanced Materials, 2011. **23**(31): p. 3597.

56. Howells, T.J., *Asymmetric Tandem Organic Solar Cells*, in *Department of Chemistry*. 2011, University of Warwick.

57. Rowell, M.W. and M.D. McGehee, *Transparent electrode requirements for thin film solar cell modules.* Energy & Environmental Science, 2011. **4**(1): p. 131.

58. Phillips, T.W. and J.C.d. Mello, *New Materials for Transparent Electrodes*, M. Organic Electronics: Materials, and Applications, Editor. 2006, Wiley. p. 139.

59. The United States Geological Survey (USGS), *Mineral Commodity Summaries - Indium*. 2013. p. 74.

60. Kalyanasundaram, K., *Dye-sensitized Solar Cells*. 2010: EFPL Press.

61. Organic Electronics Association, *Organic and Printed Electronics*, D.K. Hecker, Editor. 2011.

62. Galagan, Y., B. Zimmermann, E.W.C. Coenen, M. Jørgensen, D.M. Tanenbaum, F.C. Krebs, H. Gorter, S. Sabik, L.H. Slooff, S.C. Veenstra, J.M. Kroon, and R. Andriessen, *Current Collecting Grids for ITO-Free Solar Cells.* Advanced Energy Materials, 2012. **2**(1): p. 103.

63. Gupta, D., M.M. Wienk, and R.A. Janssen, *Efficient polymer solar cells on opaque substrates with a laminated PEDOT: PSS top electrode.* Advanced Energy Materials, 2013. **3**(6): p. 782.

64. Liu, J., A.W. Hains, J.D. Servaites, M.A. Ratner, and T.J. Marks, *Highly Conductive Bilayer Transparent Conducting Oxide Thin Films for Large-Area Organic Photovoltaic Cells.* Chemistry of Materials, 2009. **21**(21): p. 5258.

65. Roy-Mayhew, J.D., G. Boschloo, A. Hagfeldt, and I.A. Aksay, *Functionalized Graphene Sheets as a Versatile Replacement for Platinum in Dye-Sensitized Solar Cells.* ACS Applied Materials & Interfaces, 2012. **4**(5): p. 2794.

66. Fan, B., X. Mei, K. Sun, and J. Ouyang, *Conducting polymer/carbon nanotube composite as counter electrode of dye-sensitized solar cells.* Applied Physics Letters, 2008. **93**(14): p. 143103.

67. Kymakis, E., G. Klapsis, E. Koudoumas, E. Stratakis, N. Kornilios, N. Vidakis, and Y. Franghiadakis, *Carbon nanotube/PEDOT:PSS electrodes for organic*

photovoltaics. The European Physical Journal - Applied Physics, 2006. **36**(03): p. 257.

68. Mustonen, T., K. Kordás, S. Saukko, G. Tóth, J.S. Penttilä, P. Helistö, H. Seppä, and H. Jantunen, *Inkjet printing of transparent and conductive patterns of single-walled carbon nanotubes and PEDOT-PSS composites.* physica status solidi (b), 2007. **244**(11): p. 4336.

69. Kalyanasundaram, K., *Photochemical and Photoelectrochemical approaches to energy conversion*. 2010, EFPL Press. p. 1.

70. Mo, S.-D. and W.Y. Ching, *Electronic and optical properties of three phases of titanium dioxide: Rutile, anatase, and brookite.* Physical Review B, 1995. **51**(19): p. 13023.

71. Di Paola, A., M. Bellardita, and L. Palmisano, *Brookite, the Least Known TiO2 Photocatalyst.* Catalysts, 2013. **3**(1): p. 36.

72. Černá, M., M. Veselý, and P. Dzik, *Physical and chemical properties of titanium dioxide printed layers.* Catalysis Today, 2011. **161**(1): p. 97.

73. Brus, L., *Electronic wave functions in semiconductor clusters: experiment and theory.* The Journal of Physical Chemistry, 1986. **90**(12): p. 2555.

74. Bertrand, F., S.-A. German, A. Anwar, V. Irune, B. Gemma, R.D.M. Yolanda, and B. Lennart, *Dispersion and surface functionalization of oxide nanoparticles for transparent photocatalytic and UV-protecting coatings and sunscreens.* Science and Technology of Advanced Materials, 2013. **14**(2): p. 023001.

75. Zhang, Z., C.-C. Wang, R. Zakaria, and J.Y. Ying, *Role of Particle Size in Nanocrystalline TiO2-Based Photocatalysts.* The Journal of Physical Chemistry B, 1998. **102**(52): p. 10871.

76. Jeng, M.-J., Y.-L. Wung, L.-B. Chang, and L. Chow, *Particle Size Effects of TiO2 Layers on the Solar Efficiency of Dye-Sensitized Solar Cells.* International Journal of Photoenergy, 2013. **2013**: p. 9.

77. Cojocaru, L., C. Olivier, T. Toupance, E. Sellier, and L. Hirsch, *Size and shape fine-tuning of SnO2 nanoparticles for highly efficient and stable dye-sensitized solar cells.* Journal of Materials Chemistry A, 2013. **1**(44): p. 13789.

78. Hara, K. and H. Arakawa, *Dye-sensitized Solar Cells*, in *Handbook of Photovoltaic Science and Engineering*. 2003, John Wiley & Sons, Ltd. p. 663.

79. Ito, S., P. Liska, P. Comte, R. Charvet, P. Pechy, U. Bach, L. Schmidt-Mende, S.M. Zakeeruddin, A. Kay, M.K. Nazeeruddin, and M. Gratzel, *Control of dark current in photoelectrochemical (TiO2/I--I3-) and dye-sensitized solar cells.* Chemical Communications, 2005(34): p. 4351.

80. Huang, F., D. Chen, Q. Li, R.A. Caruso, and Y.-B. Cheng, *Construction of nanostructured electrodes on flexible substrates using pre-treated building blocks.* Applied Physics Letters, 2012. **100**(12): p. 123102.

81. Ito, S., *How to make high-efficiency dye-sensitized solar cells*, D.-s.s. cells, Editor. 2010, EFPL Press. p. 251.

82. Kim, B.-S., J.-Y. Park, C.-S. Kim, S.-B. Kim, D.-K. Song, H.-D. Jang, S.-E. Lee, and T.-O. Kim, *Zirconium Oxide Post-treatment for TiO2 Photoelectrodes in Dye-Sensitized Solar Cells.* Electrochimica Acta, 2015. **174**: p. 502.

83. Al-Juaid, F., A. Merazga, F. Abdel-Wahab, and M. Al-Amoudi, *ZnO Spin-Coating of TiO2 Photo-Electrodes to Enhance the Efficiency of Associated Dye-Sensitized Solar Cells.* World Journal of Condensed Matter Physics, 2012. **2**(4): p. 5.

84. Chen, S.G., S. Chappel, Y. Diamant, and A. Zaban, *Preparation of Nb2O5 Coated TiO2 Nanoporous Electrodes and Their Application in Dye-Sensitized Solar Cells.* Chemistry of Materials, 2001. **13**(12): p. 4629.

85. Song-Yuan, D. and W. Kong-Jia, *Optimum Nanoporous TiO2 Film and Its Application to Dye-sensitized Solar Cells.* Chinese Physics Letters, 2002. **20**(6): p. 953.

86. Baglio, V., M. Girolamo, V. Antonucci, and A.S. Aricò, *Influence of TiO2 Film Thickness on the Electrochemical Behaviour of Dye-Sensitized Solar Cells.* International Journal of Electrochemical Science, 2011. **6**: p. 3375.

87. Ito, S., S.M. Zakeeruddin, R. Humphry-Baker, P. Liska, R. Charvet, P. Comte, M.K. Nazeeruddin, P. Péchy, M. Takata, H. Miura, S. Uchida, and M. Grätzel, *High-Efficiency Organic-Dye- Sensitized Solar Cells Controlled by Nanocrystalline-TiO2 Electrode Thickness.* Advanced Materials, 2006. **18**(9): p. 1202.

88. Tsai, J., W. Hsu, T. Wu, T. Meen, and W. Chong, *Effect of compressed TiO2 nanoparticle thin film thickness on the performance of dye-sensitized solar cells.* Nanoscale Research Letters, 2013. **8**(1): p. 1.

89. Shin, I., H. Seo, M.-K. Son, J.-K. Kim, K. Prabakar, and H.-J. Kim, *Analysis of TiO2 thickness effect on characteristic of a dye-sensitized solar cell by using electrochemical impedance spectroscopy.* Current Applied Physics, 2010. **10**(3, Supplement): p. S422.

90. Lee, C.-P., C.-Y. Chou, C.-Y. Chen, M.-H. Yeh, L.-Y. Lin, R. Vittal, C.-G. Wu, and K.-C. Ho, *Zinc oxide-based dye-sensitized solar cells with a ruthenium dye containing an alkyl bithiophene group.* Journal of Power Sources, 2014. **246**(0): p. 1.

91. Seimei, S. and M. Kimiaki, *Nanoscale Roughness Control of Electron Transport Layer in Organic Solar Cells Fabricated by Sol–Gel Method.* Japanese Journal of Applied Physics, 2012. **51**(9R): p. 095803.

92. Quintana, M., T. Edvinsson, A. Hagfeldt, and G. Boschloo, *Comparison of Dye-Sensitized ZnO and TiO2 Solar Cells: Studies of Charge Transport and Carrier Lifetime.* The Journal of Physical Chemistry C, 2007. **111**(2): p. 1035.

93. Abdul Rani, R., A.S. Zoolfakar, J. Subbiah, J.Z. Ou, and K. Kalantar-zadeh, *Highly ordered anodized Nb2O5 nanochannels for dye-sensitized solar cells.* Electrochemistry Communications, 2014. **40**: p. 20.

94. Wang, D., S. Watson, L.-P. Sung, I.H. Tseng, C. Bouis, and R. Fernando, *Effect of TiO2 pigment type on the UV degradation of filled coatings.* Journal of Coatings Technology and Research, 2011. **8**(1): p. 19.

95. Staniland, P., *Nanotechnology and Sun Care A Risk Review.* Household and personal care today, 2013. **8**(2): p. 18.

96. Zhu, S., Z. An, X. Sun, Z. Wu, X. Chen, and P. Chen, *Synthesis and evaluation of simple molecule as a co-adsorbent dye for highly efficient co-sensitized solar cells.* Dyes and Pigments, 2015. **120**(0): p. 85.

97. Reinders, A., *Options for photovoltaic solar energy systems in portable products.* proceedings of TMCE, Wuhan, China, 2002.

98. Zhang, K., C. Qin, X. Yang, A. Islam, S. Zhang, H. Chen, and L. Han, *High-Performance, Transparent, Dye-Sensitized Solar Cells for See-Through Photovoltaic Windows.* Advanced Energy Materials, 2014. **4**(11): p. n/a.

99. Lim, J., M. Lee, S.K. Balasingam, J. Kim, D. Kim, and Y. Jun, *Fabrication of panchromatic dye-sensitized solar cells using pre-dye coated TiO2 nanoparticles by a simple dip coating technique.* RSC Advances, 2013. **3**(14): p. 4801.

100. Opara Krašovec, U., M. Bokalič, and M. Topič, *Ageing of DSSC studied by electroluminescence and transmission imaging.* Solar Energy Materials and Solar Cells, 2013. **117**: p. 67.

101. Hardin, B.E., H.J. Snaith, and M.D. McGehee, *The renaissance of dye-sensitized solar cells.* Nat Photon, 2012. **6**(3): p. 162.

102. Christians, J.A., R.C.M. Fung, and P.V. Kamat, *An Inorganic Hole Conductor for Organo-Lead Halide Perovskite Solar Cells. Improved Hole Conductivity with Copper Iodide.* Journal of the American Chemical Society, 2013. **136**(2): p. 758.

103. Zhao, Y., A.M. Nardes, and K. Zhu, *Solid-State Mesostructured Perovskite CH3NH3PbI3 Solar Cells: Charge Transport, Recombination, and Diffusion Length.* The Journal of Physical Chemistry Letters, 2014. **5**(3): p. 490.

104. Bandara, J. and M. Thelakkat, *Thickness dependence of device parameters in solid state dye sensitized solar cells.* Journal of the National Science Foundation of Sri Lanka, 2011. **39**(1): p. 35.

105. Zukalová, M., J. Procházka, A. Zukal, J.H. Yum, and L. Kavan, *Structural parameters controlling the performance of organized mesoporous TiO2 films in dye sensitized solar cells.* Inorganica Chimica Acta, 2008. **361**(3): p. 656.

106. Kouhnavard, M., N.A. Ludin, B.V. Ghaffari, K. Sopian, and S. Ikeda, *Carbonaceous Materials and Their Advances as a Counter Electrode in Dye-Sensitized Solar Cells: Challenges and Prospects.* ChemSusChem, 2015. **8**(9): p. 1510.

107. Kim, D.H., S.E. Atanasov, P. Lemaire, K. Lee, and G.N. Parsons, *Platinum-Free Cathode for Dye-Sensitized Solar Cells Using Poly(3,4-ethylenedioxythiophene) (PEDOT) Formed via Oxidative Molecular Layer Deposition.* ACS Applied Materials & Interfaces, 2015. **7**(7): p. 3866.

108. Wu, M. and T. Ma, *Platinum-Free Catalysts as Counter Electrodes in Dye-Sensitized Solar Cells.* ChemSusChem, 2012. **5**(8): p. 1343.

109. Murakami, T.N., S. Ito, Q. Wang, M.K. Nazeeruddin, T. Bessho, I. Cesar, P. Liska, R. Humphry-Baker, P. Comte, P. Péchy, and M. Grätzel, *Highly Efficient Dye-Sensitized Solar Cells Based on Carbon Black Counter Electrodes.* Journal of The Electrochemical Society, 2006. **153**(12): p. A2255.

110. Kim, H., H. Choi, S. Hwang, Y. Kim, and M. Jeon, *Fabrication and characterization of carbon-based counter electrodes prepared by electrophoretic deposition for dye-sensitized solar cells.* Nanoscale Research Letters, 2012. **7**(1): p. 53.

111. Ceresana, *Market Study: Carbon Black* 2015.

112. Kay, A. and M. Grätzel, *Low cost photovoltaic modules based on dye sensitized nanocrystalline titanium dioxide and carbon powder.* Solar Energy Materials and Solar Cells, 1996. **44**(1): p. 99.

113. Dong, H., Z. Wu, Y. Gao, A. El-Shafei, B. Jiao, Y. Dai, and X. Hou, *A nanostructure-based counter electrode for dye-sensitized solar cells by assembly of silver nanoparticles.* Organic Electronics, 2014. **15**(7): p. 1641.

114. Ryu, J., T. Wakida, and T. Takagishi, *Effect of Corona Discharge on the Surface of Wool and Its Application to Printing.* Textile Research Journal, 1991. **61**(10): p. 595.

115. Savastano, D., *The conductive ink market: the printed electronics market is making gains as new applications emerge, and conductive ink manufacturers are seeing more opportunities.* Ink World, 2013.

116. Pasquarelli, R.M., D.S. Ginley, and R. O'Hayre, *Solution processing of transparent conductors: from flask to film.* Chemical Society Reviews, 2011. **40**(11): p. 5406.

117. Oh, Y., S.-N. Lee, H.-K. Kim, and J. Kim, *UV-Assisted Chemical Sintering of Inkjet-Printed TiO2 Photoelectrodes for Low-Temperature Flexible Dye-Sensitized Solar Cells.* Journal of the Electrochemical Society, 2012. **159**(10): p. H777.

118. Hoth, C.N., P. Schilinsky, S.A. Choulis, S. Balasubramanian, and C.J. Brabec, *Solution-Processed Organic Photovoltaics*, in *Applications of Organic and Printed Electronics, Integrated Circuits and Systems*, E. Cantatore, Editor. 2013.

119. Di Risio, S. and N. Yan, *Piezoelectric Ink-Jet Printing of Horseradish Peroxidase: Effect of Ink Viscosity Modifiers on Activity.* Macromolecular Rapid Communications, 2007. **28**(18-19): p. 1934.

120. Calvert, P., *Inkjet Printing for Materials and Devices.* Chemistry of Materials, 2001. **13**(10): p. 3299.

121. Magdassi, S., *The Chemistry Of Inkjet Inks*. 2010: World Scientific Publishing Company, Incorporated.

122. Angelo, P.D., *Inkjet-Printed Light-Emitting Devices: Applying Inkjet Microfabrication to Multilayer Electronics*, in *Department of Chemical Engineering & Applied Chemistry*. 2013, University of Toronto. p. 279.

123. Sridhar, A.B., Thomas; Baumann, Reinhard;, *Inkjet Printing as a Key Enabling Technology for Printed Electronics.* Material Matters, 2011. **Volume 6** (1): p. 12.

124. Yin, Z., Y. Huang, N. Bu, X. Wang, and Y. Xiong, *Inkjet printing for flexible electronics: Materials, processes and equipments.* Chinese Science Bulletin, 2010. **55**(30): p. 3383.

125. Tekin, E., P.J. Smith, and U.S. Schubert, *Inkjet printing as a deposition and patterning tool for polymers and inorganic particles.* Soft Matter, 2008. **4**(4): p. 703.

126. Shin, D.-Y. and P.J. Smith, *Theoretical investigation of the influence of nozzle diameter variation on the fabrication of thin film transistor liquid crystal display color filters.* Journal of Applied Physics, 2008. **103**(11): p. 114905.

127. Hoath, S.D., G.D. Martin, and I.M. Hutchings. *Effects of Fluid Viscosity on Drop-on-Demand Ink-Jet Break-Off*. in *International Conference on Digital Printing Technologies and Digital Fabrication*. 2010. Society for Imaging Science and Technology.

128. Fujifilm-Dimatix. *Jettable Fluid Formulation Guidelines*. 2013; Available from: http://www.fujifilmusa.com/shared/bin/Dimatix_Materials_Printer_Jettable_Fluid_Formulation_Guidelines_05-13.pdf.

129. Svanholm, E., *Printability and Ink-Coating Interactions in Inkjet Printing*, in *Chemical Engineering*. 2007, Karlstad University.

130. Hoth, C.N., S.A. Choulis, P. Schilinsky, and C.J. Brabec, *High Photovoltaic Performance of Inkjet Printed Polymer:Fullerene Blends.* Advanced Materials, 2007. **19**(22): p. 3973.

131. Sun, Y., Y. Zhang, Q. Liang, Y. Zhang, H. Chi, Y. Shi, and D. Fang, *Solvent inkjet printing process for the fabrication of polymer solar cells.* RSC Advances, 2013. **3**(30): p. 11925.

132. Kunjappu, J.T., *Ink chemistry.* Chemistry World, 2003. **3**.

133. Attension, *Tensiometry in Inkjet Printing Applications*. 2011. p. 1.

134. Jang, D., D. Kim, and J. Moon, *Influence of Fluid Physical Properties on Ink-Jet Printability.* Langmuir, 2009. **25**(5): p. 2629.

135. DeJidas, L.P. and T.M. Destree, *Sheetfed Offset Press Operating*. 2005: PIA/GATF Press.

136. Ito, S., P. Chen, P. Comte, M.K. Nazeeruddin, P. Liska, P. Péchy, and M. Grätzel, *Fabrication of screen-printing pastes from TiO2 powders for dye-sensitised solar cells.* Progress in Photovoltaics: Research and Applications, 2007. **15**(7): p. 603.

137. Huang, M.-R. and X.-G. Li, *Thermal degradation of cellulose and cellulose esters.* Journal of Applied Polymer Science, 1998. **68**(2): p. 293.

138. Mandzy, N., E. Grulke, and T. Druffel, *Breakage of TiO2 agglomerates in electrostatically stabilized aqueous dispersions.* Powder Technology, 2005. **160**(2): p. 121.

139. Sato, K., J.-G. Li, H. Kamiya, and T. Ishigaki, *Ultrasonic Dispersion of TiO2 Nanoparticles in Aqueous Suspension.* Journal of the American Ceramic Society, 2008. **91**(8): p. 2481.

140. Colloidal Dynamics, *Determining the isoelectric point (i.e.p.)* 2014.

141. Malvern Instruments, *Zeta Potential. An Introduction in 30 Minutes* in *Zetasizer Nano series technical note*. 2014.

142. Uskoković, V., *Dynamic Light Scattering Based Microelectrophoresis: Main Prospects and Limitations.* Journal of dispersion science and technology, 2012. **33**(12): p. 1762.

143. Advanced Nano Products. *Nano-Silver Ink for Inkjet Printing*. 2013 24.04.14]; Available from: http://anapro.com/eng/product/silver_inkjet_ink.html.

144. Sun Chemical, *SunJet Develops Platform Inkjet Chemistry for Conductive Silver Inks at drupa.* Pigment & Resin Technology, 2008. **37**(5).

145. Nanogap. *Silver NanoParticles*. 2014; Available from: http://www.nanogap.es/#!silver-nanoparticles/c1it1.

146. Obene, P. and I. Clark, *High resolution copper ink printing for electronic interconnects.* Electronic Engineering Times Europe, 2013. **September**: p. 20.

147. Cui, W., W. Lu, Y. Zhang, G. Lin, T. Wei, and L. Jiang, *Gold nanoparticle ink suitable for electric-conductive pattern fabrication using in ink-jet printing technology.* Colloids and Surfaces A: Physicochemical and Engineering Aspects, 2010. **358**(1–3): p. 35.

148. Johnson Matthey, *Printed Electronic Inks.* 2013.

149. Intrinsiq materials. *Our products,*. 2013 24.04.14]; Available from: http://intrinsiqmaterials.com/our-products/.

150. Applied Nanotech Holdings Inc. *ANI Nanoparticle Nickel Inks*. 2013; Available from: http://www.appliednanotech.net/tech/conductive_ink_ni.php.

151. Bakhishev, T. and V. Subramanian, *Investigation of Gold Nanoparticle Inks for Low-Temperature Lead-Free Packaging Technology.* Journal of Electronic Materials, 2009. **38**(12): p. 2720.

152. Laughton, M.A. and D.F. Warne, *Electrical Engineer's Reference Book*. 2002: Elsevier Science.

153. Perelaer, B.J., A.W.M. de Laat, C.E. Hendriks, and U.S. Schubert, *Inkjet-printed silver tracks: low temperature curing and thermal stability investigation.* Journal of Materials Chemistry, 2008. **18**(27): p. 3209.

154. Hsien-Hsueh, L., C. Kan-Sen, and H. Kuo-Cheng, *Inkjet printing of nanosized silver colloids.* Nanotechnology, 2005. **16**(10): p. 2436.

155. Walker, S.B. and J.A. Lewis, *Reactive Silver Inks for Patterning High-Conductivity Features at Mild Temperatures.* Journal of the American Chemical Society, 2012. **134**(3): p. 1419.

156. Lu, H., J. Lin, N. Wu, S. Nie, Q. Luo, C.-Q. Ma, and Z. Cui, *Inkjet printed silver nanowire network as top electrode for semi-transparent organic photovoltaic devices.* Applied Physics Letters, 2015. **106**(9): p. 093302.

157. Finn, D.J., M. Lotya, and J.N. Coleman, *Inkjet Printing of Silver Nanowire Networks.* ACS Applied Materials & Interfaces, 2015. **7**(17): p. 9254.

158. Kang, J., J. Ryu, H. Kim, and H. Hahn, *Sintering of inkjet-printed silver nanoparticles at room temperature using intense pulsed light.* Journal of Electronic Materials, 2011. **40**(11): p. 2268.

159. Lim, S., D. Han, H. Kim, S. Lee, and S. Yoo, *Cu-based multilayer transparent electrodes: A low-cost alternative to ITO electrodes in organic solar cells.* Solar Energy Materials and Solar Cells, 2012. **101**: p. 170.

160. Hutter, O.S. and R.A. Hatton, *A Hybrid Copper:Tungsten Suboxide Window Electrode for Organic Photovoltaics.* Advanced Materials, 2015. **27**(2): p. 326.

161. Grouchko, M., A. Kamyshny, and S. Magdassi, *Formation of air-stable copper-silver core-shell nanoparticles for inkjet printing.* Journal of Materials Chemistry, 2009. **19**(19): p. 3057.

162. Zenou, M., O. Ermak, A. Saar, and Z. Kotler, *Laser sintering of copper nanoparticles.* Journal of Physics D: Applied Physics, 2014. **47**(2): p. 025501.

163. Yung, K., X. Gu, C. Lee, and H. Choy, *Ink-jet printing and camera flash sintering of silver tracks on different substrates.* Journal of Materials Processing Technology, 2010. **210**(15): p. 2268.

164. Cherrington, M., T.C. Claypole, D. Deganello, I. Mabbett, T. Watson, and D. Worsley, *Ultrafast near-infrared sintering of a slot-die coated nano-silver conducting ink.* Journal of Materials Chemistry, 2011. **21**(21): p. 7562.

165. Perelaer, J., B.J. de Gans, and U.S. Schubert, *Ink-jet printing and microwave sintering of conductive silver tracks.* Advanced Materials, 2006. **18**(16): p. 2101.

166. Allaoui, A., S. Bai, H.M. Cheng, and J.B. Bai, *Mechanical and electrical properties of a MWNT/epoxy composite.* Composites Science and Technology, 2002. **62**(15): p. 1993.

167. Sandler, J., M.S.P. Shaffer, T. Prasse, W. Bauhofer, K. Schulte, and A.H. Windle, *Development of a dispersion process for carbon nanotubes in an epoxy matrix and the resulting electrical properties.* Polymer, 1999. **40**(21): p. 5967.

168. Asthana, A., T. Maitra, R. Büchel, MK.Tiwari, and D. Poulikakos, *Multifunctional superhydrophobic polymer/carbon nanocomposites: graphene, carbon nanotubes, or carbon black?* ACS Appl Mater Interfaces, 2014. **6**(11).

169. Zhou, Y.F.-H., C; Shim, J; Meyer, J; Giordano, A,J; Li, H; Winget, P; Papadopoulos, T; Cheun, H; Kim, J; Fenoll, M; Dindar, A; Haske, W; Najafabadi, E; Khan, TM; Sojoudi, H; Barlow, S; Graham, S; Brédas, JL; Marder, SR; Kahn, A; Kippelen, B, *A universal method to produce low-work function electrodes for organic electronics.* Science, 2012. **Vol. 336 (6079)**: p. 327.

170. Zhang, D.W., X.D. Li, H.B. Li, S. Chen, Z. Sun, X.J. Yin, and S.M. Huang, *Graphene-based counter electrode for dye-sensitized solar cells.* Carbon, 2011. **49**(15): p. 5382.

171. Geoghegan, M. and G. Hadziioannou, *Polymer Electronics*. 2013: OUP Oxford.

172. Chandrasekhar, P., *Conducting Polymers, Fundamentals and Applications: A Practical Approach*. 1999: Springer US.

173. Syed, A.A. and M.K. Dinesan, *Review: Polyaniline—A novel polymeric material.* Talanta, 1991. **38**(8): p. 815.

174. Aldissi, M., *Intrinsically Conducting Polymers: An Emerging Technology*. 1993: Springer.

175. Townsend, P.D., D.D.C. Bradley, M.E. Horton, C.M. Pereira, R.H. Friend, N.C. Billingham, P.D. Calvert, P.J.S. Foot, D.C. Bott, C.K. Chai, N.S. Walker, and K.P.J. Williams, *Electronic Properties of Polyacetylene Prepared by the Durham Route*, in *Electronic Properties of Polymers and Related Compounds*, H. Kuzmany, M. Mehring, and S. Roth, Editors. 1985, Springer Berlin Heidelberg. p. 50.

176. Huber, J. and S. Mecking, *Processing of Polyacetylene from Aqueous Nanoparticle Dispersions.* Angewandte Chemie, 2006. **118**(38): p. 6462.

177. Jang, K.S., H. Lee, and B. Moon, *Synthesis and characterization of water soluble polypyrrole doped with functional dopants.* Synthetic Metals, 2004. **143**(3): p. 289.

178. Takano, T., A. Mikazuki, and T. Kobayashi, *Conductive polypyrrole composite films prepared using wet cast technique with a pyrrole–cellulose acetate solution.* Polymer Engineering & Science, 2014. **54**(1): p. 78.

179. Elschner, A., S. Kirchmeyer, W. Lovenich, U. Merker, and K. Reuter, *PEDOT: Principles and Applications of an Intrinsically Conductive Polymer*. 2010: CRC Press.

180. Yoshioka, Y. and G.E. Jabbour, *Desktop inkjet printer as a tool to print conducting polymers.* Synthetic Metals, 2006. **156**(11–13): p. 779.

181. Aernouts, T., P. Vanlaeke, W. Geens, J. Poortmans, P. Heremans, S. Borghs, R. Mertens, R. Andriessen, and L. Leenders, *Printable anodes for flexible organic solar cell modules.* Thin Solid Films, 2004. **451**: p. 22.

182. Vosgueritchian, M., D.J. Lipomi, and Z. Bao, *Highly conductive and transparent PEDOT: PSS films with a fluorosurfactant for stretchable and flexible transparent electrodes.* Advanced Functional Materials, 2012. **22**(2): p. 421.

183. Crispin, X., F. Jakobsson, A. Crispin, P. Grim, P. Andersson, A. Volodin, C. Van Haesendonck, M. Van der Auweraer, W.R. Salaneck, and M. Berggren, *The origin of*

the high conductivity of poly (3, 4-ethylenedioxythiophene)-poly (styrenesulfonate)(PEDOT-PSS) plastic electrodes. Chemistry of Materials, 2006. **18**(18): p. 4354.

184. Ouyang, J., Q. Xu, C.-W. Chu, Y. Yang, G. Li, and J. Shinar, *On the mechanism of conductivity enhancement in poly (3, 4-ethylenedioxythiophene): poly (styrene sulfonate) film through solvent treatment.* Polymer, 2004. **45**(25): p. 8443.

185. Hohnholz, D., H. Okuzaki, and A.G. MacDiarmid, *Plastic electronic devices through line patterning of conducting polymers.* Advanced Functional Materials, 2005. **15**(1): p. 51.

186. Cruz-Cruz, I., M. Reyes-Reyes, M.A. Aguilar-Frutis, A.G. Rodriguez, and R. López-Sandoval, *Study of the effect of DMSO concentration on the thickness of the PSS insulating barrier in PEDOT:PSS thin films.* Synthetic Metals, 2010. **160**(13–14): p. 1501.

187. Eom, S.H., S. Senthilarasu, P. Uthirakumar, S.C. Yoon, J. Lim, C. Lee, H.S. Lim, J. Lee, and S.-H. Lee, *Polymer solar cells based on inkjet-printed PEDOT: PSS layer.* Organic Electronics, 2009. **10**(3): p. 536.

188. Weng, B., R. Shepherd, K. Crowley, A. Killard, and G.G. Wallace, *Printing conducting polymers.* Analyst, 2010. **135**(11): p. 2779.

189. Suttiponparnit, K., J. Jiang, M. Sahu, S. Suvachittanont, T. Charinpanitkul, and P. Biswas, *Role of Surface Area, Primary Particle Size, and Crystal Phase on Titanium Dioxide Nanoparticle Dispersion Properties.* Nanoscale Research Letters, 2011. **6**(27).

190. Kuscer, D., G. Stavber, G. Trefalt, and M. Kosec, *Formulation of an Aqueous Titania Suspension and its Patterning with Ink-Jet Printing Technology.* Journal of the American Ceramic Society, 2012. **95**(2): p. 487.

191. Kanniah, V., P. Wu, N. Mandzy, and E.A. Grulke, *Fractal analysis as a complimentary technique for characterizing nanoparticle size distributions.* Powder Technology, 2012. **226**(0): p. 189.

192. Kim, S.-J. and D.E. McKean, *Aqueous TiO2 suspension preparation and novel application of ink-jet printing technique for ceramics patterning.* Journal of Materials Science Letters, 1998. **17**(2): p. 141.

193. Imao, T., N. Noma, and S. Ito, *Preparation of TiO2 nanocrystalline films controlled by acetylacetone/polyethylene glycol and their photoelectric properties.* Journal of Sol-Gel Science and Technology, 2006. **38**(2): p. 197.

194. Peng, B., Y. Huang, L.-y. Chai, G.-l. Li, M.-m. Cheng, and X.-f. Zhang, *Influence of polymer dispersants on dispersion stability of nano-TiO2 aqueous suspension and its application in inner wall latex paint.* Journal of Central South University of Technology, 2007. **14**(4): p. 490.

195. Schott. *Ultra-Thin Glass*. 2015 06.03.2015]; Available from: http://www.us.schott.com/advanced_optics/english/products/wafers-and-thin-glass/glass-wafer-and-substrates/ultra-thin-glass/index.html.

196. Pilkington. *Pilkington Microfloat™*. 2015; Available from: https://www.pilkington.com/en-gb/uk/products/product-categories/special-applications/pilkington-microfloat.

197. MacDonald, W.A., *Advanced Flexible Polymeric Substrates*, in *Organic electronics, Materials, Manufacturing and Applications*, H. Klauk, Editor. 2006, Wiley. p. 164.

198. Dupont, *High performance flexible films for photovoltaic substrates*. 2012.

199. Wang, C., L. Wang, Y. Shi, H. Zhang, and T. Ma, *Printable electrolytes for highly efficient quasi-solid-state dye-sensitized solar cells.* Electrochimica Acta, 2013. **91**: p. 302.

200. Samad, W.Z., M.M. Salleh, A. Shafiee, and M.A. Yarmo. *Transparent conducting thin films of fluoro doped tin oxide (FTO) deposited using inkjet printing technique*. in *Semiconductor Electronics (ICSE), 2010 IEEE International Conference on*. 2010.

201. Pilkington. *NSG TEC™ (Solar applications)*. 2016 17/03/2016]; Available from: http://www.pilkington.com/products/bp/bybenefit/solarenergy/tec/literature.htm.

202. Aldrich, S. *Indium tin oxide coated PET*. 2016 17/03/2016]; Available from: http://www.sigmaaldrich.com/catalog/product/aldrich/639303?lang=en&region=GB.

203. Peccell. *Dye Sensitized Solar Cells*. 2016 17/03/2016]; Available from: http://www.peccell.com/index_e.html.

204. Ito, S., *How to make high-efficiency dye-sensitized solar cells*, in *Dye sensitized solar cells*, K. Kalyanasundaram, Editor. 2010, EFPL Press. p. 251.

205. Kim, Y.H., C. Sachse, M.L. Machala, C. May, L. Müller-Meskamp, and K. Leo, *Highly Conductive PEDOT:PSS Electrode with Optimized Solvent and Thermal Post-Treatment for ITO-Free Organic Solar Cells.* Advanced Functional Materials, 2011. **21**(6): p. 1076.

206. Solaronix. *Platisol T/SP*. 2016; Available from: http://shop.solaronix.com/platinum-catalysts/platisol-t-sp.html.

207. Pitney Bowes, *High-speed inkjet printing*. 2015. p. 1.

208. Okumura, M. and T. Takahashi, *Novel Micro Piezo Technology for Ink Jet Printhead* in *NIP23 and Digital Fabrication 2007*. 2007, Society for Imaging Science and Technology. p. 314.

209. Liu, F., J. Wu, K. Chen, and D. Xue, *Morphology study by using scanning electron microscopy.* Microscopy: Science, Technology, Applications and Education, 2010: p. 1781.

210. Goldstein, J., D.E. Newbury, D.C. Joy, C.E. Lyman, P. Echlin, E. Lifshin, L. Sawyer, and J.R. Michael, *Scanning Electron Microscopy and X-ray Microanalysis*. 3 ed. 2012: Springer US.

211. Goodhew, P.J., J. Humphreys, and R. Beanland, *Electron Microscopy and Analysis, Third Edition*. 2000: Taylor & Francis.

212. Reimer, L., *Scanning Electron Microscopy: Physics of Image Formation and Microanalysis*. 1998: Springer.

213. Malvern Instruments Limited, *Dynamic light scattering common terms defined*. 2011.

214. Koch, C., I. Ovid'ko, S. Seal, and S. Veprek, *Structural Nanocrystalline Materials: Fundamentals and Applications*. 2007: Cambridge University Press.

215. Viswanath, D.S., T. Ghosh, D.H.L. Prasad, N.V.K. Dutt, and K.Y. Rani, *Viscosity of Liquids: Theory, Estimation, Experiment, and Data*. 2007: Springer Netherlands.

216. Wang, X., W.W. Carr, D.G. Bucknall, and J.F. Morris, *High-shear-rate capillary viscometer for inkjet inks.* Review of Scientific Instruments, 2010. **81**(6): p. 065106.

217. Zou, M., S. Cai, Z. Zhao, L. Chen, Y. Zhao, X. Fan, and S. Chen, *A novel polydimethylsiloxane microfluidic viscometer fabricated using microwire-molding.* Review of Scientific Instruments, 2015. **86**(10): p. 104302.

218. RheoSense. *Viscometer-Rheometer-on-a-Chip* 2015 09.10.2015]; Available from: http://www.rheosense.com/technology.

219. Biolin Scientific, *Theta Optical Tensiometer User Manual*. 2016.

220. Owens, D.K. and R.C. Wendt, *Estimation of the surface free energy of polymers.* Journal of Applied Polymer Science, 1969. **13**(8): p. 1741.

221. Huang, X.D., S.M. Bhangale, P.M. Moran, N.L. Yakovlev, and J. Pan, *Surface modification studies of Kapton® HN polyimide films.* Polymer International, 2003. **52**(7): p. 1064.

222. W. A. Zisman, *Relation of the Equilibrium Contact Angle to Liquid and Solid Constitution*, in *Contact Angle, Wettability, and Adhesion*. 1964, AMERICAN CHEMICAL SOCIETY. p. 1.

223. Yang, L., J. Chen, Y. Guo, and Z. Zhang, *Surface modification of a biomedical polyethylene terephthalate (PET) by air plasma.* Applied Surface Science, 2009. **255**(8): p. 4446.

224. Qian, B. and Z. Shen, *Fabrication of Superhydrophobic Surfaces by Dislocation-Selective Chemical Etching on Aluminum, Copper, and Zinc Substrates.* Journal of the American Chemical Society, 2005. **21**(20): p. 9007.

225. BYK-Gardner GmbH. *Introduction to transparency*. 2015; 61]. Available from: http://www.byk.com/fileadmin/byk/support/instruments/theory/appearance/en/Intro_Transparency.pdf.

226. Bandara, H.M.N., R.M.G. Rajapakse, K. Murakami, G.R.R.A. Kumara, and G. Anuradha Sepalage, *Dye-sensitized solar cell based on optically transparent TiO2 nanocrystalline electrode prepared by atomized spray pyrolysis technique.* Electrochimica Acta, 2011. **56**(25): p. 9159.

227. Tagliaferro, R., D. Colonna, T.M. Brown, A. Reale, and A. Di Carlo, *Interplay between transparency and efficiency in dye sensitized solar cells.* Optics Express, 2013. **21**(3): p. 3235.

228. Jandel Engineering Limited, *Cylindrical four point probe head.* 2016.

229. Heaney, M., *Electrical Conductivity and Resistivity*, in *The Measurement, Instrumentation and Sensors Handbook on CD-ROM*. 1999, CRC Press.

230. Frederik C Krebs, *Polymeric Solar Cells: Materials, Design, Manufacture*. 2010: DEStech Publications, Inc.

231. O'Donnell, M.Z., R *How To Minimize Measurement Errors In Solar Cell Testing* Solar Industry Magazine, 2011.

232. David Ian Black, *Fabrication of hybrid inorganic and organic photovoltaic cells*, in *Emerging Technologies Research Centre*. 2011, De Montfort University: Leicester. p. 250.

233. Rahman, F., *Basics of organic photovoltaic cell*, in *Global Engineering, Science and Technology* 2012: Dhaka, Bangladesh.

234. Wacom, *Super solar simulator*. 2015. p. 1.

235. Tsakalakos, T., I.A. Ovid′ko, I.A. Ovid'ko, and A.K. Vasudevan, *Nanostructures: Synthesis, Functional Properties and Applications*. Vol. 128. 2003: Springer Netherlands.

236. Zhang, Z., S. Brown, J.B.M. Goodall, X. Weng, K. Thompson, K. Gong, S. Kellici, R.J.H. Clark, J.R.G. Evans, and J.A. Darr, *Direct continuous hydrothermal synthesis of high surface area nanosized titania.* Journal of Alloys and Compounds, 2009. **476**(1–2): p. 451.

237. Thamaphat K, L.P., Ngotawornchai B, *Phase Characterization of TiO2 Powder by XRD and TEM.* Nat. Sci, 2008. **42**(5): p. 357.

238. Rajan, K.S. and M. Silambarasan, *Sub-Micron Dispersions of TiO2 in Ethylene Glycol-Water Mixture: Rheology & Thermal Conductivity.* International Journal of ChemTech Research, 2012. **4**(3): p. 1137.

239. Sward, G., *Oil Absorption of Pigments*, in *Paint Testing Manual*. 1972, ASTM International,.

240. Gooch, J.W., *Oil Absorption (Value)*, in *Encyclopedic Dictionary of Polymers*, J.W. Gooch, Editor. 2011, Springer New York. p. 500.

241. Allen, N.S., M. Edge, A. Ortega, C.M. Liauw, J. Stratton, and R.B. McIntyre, *Behaviour of nanoparticle (ultrafine) titanium dioxide pigments and stabilisers on the photooxidative stability of water based acrylic and isocyanate based acrylic coatings.* Polymer Degradation and Stability, 2002. **78**(3): p. 467.

242. Kasperchik, V., *Oxide pigment dispersion for inkjet ink*. 2013, Google Patents.

243. Aloysius, F.H., B. Sheila, S.M. Jeremiah, D.H. Jerry, S.C. Mv, H. Parameswar, A.A. Delania, R. Kevin, and D.J. Andrew, *Advanced Solar Energy Conversion Technologies Enabled by Novel (Nano)Materials and Processing for Space Power with Potential for Terrestrial Applications*, in *12th International Energy Conversion Engineering Conference*. 2014, American Institute of Aeronautics and Astronautics.

244. Thomalla, M. and H. Tributsch, *Photosensitization of Nanostructured TiO2 with WS2 Quantum Sheets.* The Journal of Physical Chemistry B, 2006. **110**(24): p. 12167.

245. Rudyak, V.Y. and S.L. Krasnolutskii, *Dependence of the viscosity of nanofluids on nanoparticle size and material.* Physics Letters A, 2014. **378**(26–27): p. 1845.

246. Sigma Aldrich. *81170 Poly(ethylene glycol) 400*. 2016; Available from: http://www.sigmaaldrich.com/catalog/product/sial/81170?lang=en&region=GB.

247. Starr, C., C.A. Evers, and L. Starr, *Biology: Concepts and Applications*. 2006: Thomson, Brooks/Cole.

248. Kao, M.C., H.Z. Chen, S.L. Young, C.Y. Kung, and C.C. Lin, *The effects of the thickness of TiO2 films on the performance of dye-sensitized solar cells.* Thin Solid Films, 2009. **517**(17): p. 5096.

249. Dupont, *Kapton® polyimide film*. 2016.

250. Sridhar, A.B., Thomas; Baumann, Reinhard;, *Inkjet Printing as a Key Enabling Technology for Printed Electronics.* Material Matters, 2011. **Volume 6**

251. Peppas, N.A., A. Argade, and S. Bhargava, *Preparation and properties of poly(ethylene oxide) star polymers.* Journal of Applied Polymer Science, 2003. **87**(2): p. 322.

252. Dou, B., V. Dupont, P.T. Williams, H. Chen, and Y. Ding, *Thermogravimetric kinetics of crude glycerol.* Bioresource Technology, 2009. **100**(9): p. 2613.

253. Pielichowski, K., J. Njuguna, and R.T. Limited, *Thermal Degradation of Polymeric Materials*. 2005: Rapra Technology.

254. Jaroenworaluck, A., D. Regonini, C.R. Bowen, and R. Stevens, *A microscopy study of the effect of heat treatment on the structure and properties of anodised TiO2 nanotubes.* Applied Surface Science, 2010. **256**(9): p. 2672.

255. Dhas, V., S. Muduli, S. Agarkar, A. Rana, B. Hannoyer, R. Banerjee, and S. Ogale, *Enhanced DSSC performance with high surface area thin anatase TiO2 nanoleaves.* Solar Energy, 2011. **85**(6): p. 1213.

256. Mastroianni, S., A. Lanuti, S. Penna, A. Reale, T.M. Brown, A. Di Carlo, and F. Decker, *Physical and Electrochemical Analysis of an Indoor–Outdoor Ageing Test of Large-Area Dye Solar Cell Devices.* ChemPhysChem, 2012. **13**(12): p. 2925.

257. Kontos, A.G., T. Stergiopoulos, V. Likodimos, D. Milliken, H. Desilvesto, G. Tulloch, and P. Falaras, *Long-Term Thermal Stability of Liquid Dye Solar Cells.* The Journal of Physical Chemistry C, 2013. **117**(17): p. 8636.

258. Wang, G., L. Xu, J. Zhang, T. Yin, and D. Han, *Enhanced Photocatalytic Activity of TiO2 Powders (P25) via Calcination Treatment.* International Journal of Photoenergy, 2012. **2012**: p. 9.

259. Lu, S. and D.D.L. Chung, *Viscoelastic behavior of carbon black and its relationship with the aggregate size.* Carbon, 2013. **60**: p. 346.

260. Tay, T., M. Erdem, B. Ceylan, and S. Karagöz, *Adsorption of methylene blue from aqueous solution on activated carbon produced from soybean oil cake by KOH activation* 2012. Vol. 7. 2012.

261. Cai, X., Z. Lv, H. Wu, S. Hou, and D. Zou, *Direct application of commercial fountain pen ink to efficient dye-sensitized solar cells.* Journal of Materials Chemistry, 2012. **22**(19): p. 9639.

262. Kim, Y.H., C. Sachse, M.L. Machala, C. May, L. Müller-Meskamp, and K. Leo, *Highly Conductive PEDOT: PSS Electrode with Optimized Solvent and Thermal Post-Treatment for ITO-Free Organic Solar Cells.* Advanced Functional Materials, 2011. **21**(6): p. 1076.

263. Weldon, D.G., *Failure Analysis of Paints and Coatings*. 2009: Wiley.

264. Ummartyotin, S., J. Juntaro, C. Wu, M. Sain, and H. Manuspiya, *Deposition of PEDOT: PSS Nanoparticles as a Conductive Microlayer Anode in OLEDs Device by Desktop Inkjet Printer.* Journal of Nanomaterials, 2011. **2011**: p. 7.

265. Suzuki, M., K. Yamaguchi, H. Katayama, T. Muta, M. Okubo, A. Mochizuki, and H. Adachi, *Clean room having partially different degree of cleanliness*. 1987, Google Patents.

266. Cherrington, R., B.M. Wood, and V. Goodship, *Digital Printing of Titanium Dioxide for Dye Sensitized Solar Cells.* The Journal of Visualized Experiments (JoVE), 2016.

267. Holliman, P.J., M.L. Davies, A. Connell, B.V. Velasco, and T.M. Watson, *Ultra-fast dye sensitisation and co-sensitisation for dye sensitized solar cells.* Chemical Communications, 2010. **46**(38): p. 7256.

268. DeSimone, J.M., *Practical Approaches to Green Solvents.* Science, 2002. **297**(5582): p. 799.

269. Alonso, E., F.R. Field, and R.E. Kirchain, *Platinum Availability for Future Automotive Technologies*. Environmental Science & Technology, 2012. **46**(23): p. 12986.

270. Castellano, R.N., *Solar Panel Processing*. 2010: Éd. des Archives contemporaines.

271. Corporation for Comprehensive Analyses, *The Contribution of Plastic Products to Resource Efficiency*. 2005: Vienna.